# Melt Extraction from a Permeable Compacting Mantle

Peter James Webb

Submitted in accordance with the requirements for the degree of
Doctor of Philosophy
The University of Leeds, School of Earth and Environment

December 2012

# Acknowledgements

Of all the resources I have had available to me in my time at the University of Leeds, it has been the people around me that have helped the most. Everyone has been more than willing to help keep me going through the course of my post-graduate studies.

First and foremost, I wish to thank Greg for everything he has done to help me get to this point. No matter where he was in the world, Greg would do what he could to help; he was willing to help right into the last hours of the development of this work. I would also especially like to acknowledge his work on the mathematical analysis of the instabilities discussed at the end of Chapter 4. I would not be where I am now without him.

I would also like to thank everyone in the office for being so open minded and willing to discuss problems and allow me to bounce ideas around. Thank you to Amy Collinson, Barbara Hoffmann, Karen Pascal, Luke Jackson, Matt Garthwaite and Sandra Karl. I would also like to thank Tim Wright and Dan Morgan for their help in getting me here.

Outside the University, I would like to thank Colin Seddon for doing superb work checking through this thesis for errors and being generally wonderfully supportive all the way. I thank my dad, David, and step-mum, Jackie, for letting me stay in their spare room and eat all their food when my funding ran out. I would like to thank my sister Hannah and her husband Tim for the weekly Friday night games that kept me sane in the last push to finish. Thank you again to my mum, Lorraine, and step-dad, Mike, for being supportive all the way.

And to anyone I have missed, I apologise for forgetting and thank you too.

# Abstract

In this thesis, I present one- and three-dimensional numerical solutions to a two-phase fluid flow problem. The context of these investigations is the evolution of a viscous permeable matrix with a small fraction of melt that is representative of partial melt in the Earth's mantle. The matrix compacts under gravity as melt moves upward. In addition to the simple compaction solution, a range of solutions representing stably propagating waves are possible.

I first present a coherent mathematical development of the governing equations for the three-dimensional problem. I then describe a one-dimensional numerical algorithm (1D2PF) that solves the second-order inhomogeneous P.D.E. for the velocity of the viscous matrix, *V,* for arbitrary melt fraction distribution, $\varphi$ (the volume fraction occupied by melt). Combined with a time-stepping algorithm which advances the melt fraction in time, fully time-dependent 1D solutions are obtained. With an initial constant base melt fraction $\varphi_0$ with a superposed localised concentration of melt, I explore the evolution and formation of solitary compaction waves.

Using (1D2PF) I investigate the width, amplitude and phase velocity of stable solitary waves, and examine how these parameters depend on the initial conditions, permeability coefficient ($k_0$) and melt and matrix viscosities ($\eta_f$ and $\eta_m$). I demonstrate the existence of a threshold initial width above which secondary solitary waves form, with larger widths producing longer wave trains and smaller widths producing a small-amplitude oscillatory disturbance to the background melt fraction. Experiments with $k_0$, $\eta_f$ and $\eta_m$ reveal that the width of the stable solitary wave is simply proportional to the compaction length parameter $\delta = \sqrt{k_0 \eta_m / \eta_f}$ and its velocity varies as $\delta^{16/9}/\eta_m$. I also show that the width of the solitary waves varies as $\lambda_S = 4.6\delta$ and the amplitude follows the relation $A_S \simeq 89/\delta$. For initial melt fractions whose distribution is wider than the threshold width, secondary waves are produced with progressively smaller amplitude, and hence slower propagation velocity. I demonstrate that smaller values of $\delta$ result in the same volume of melt being partitioned over increasing numbers of relatively thinner solitary waves. The amplitude of the initial perturbation to the background melt fraction however is shown to have no effect on the number of solitary waves produced. A train of such waves arriving at the surface could provide an explanation of intermittent

volcanic activity above a region of partial melt.

In a preliminary study of two-phase flow in three-dimensions I have also made significant progress toward the development of a three-dimensional two-phase flow simulation program. To do so, I have adapted the three-dimensional viscous fluid convection program (TDCON) by Houseman (1990). The new program TD2PF depends on a potential-function formulation similar to that of Spiegelman (1993a), in which the divergence of the matrix velocity field, $D=\nabla\cdot\boldsymbol{V}$, and the vector potential, $\boldsymbol{A}$, are the primary variables. I have introduced new functionality to a significantly expanded three-dimensional Poisson solver (program TDPOTS) but lack of time prevented a successful conclusion to the development of a general 3D solver for the divergence field $D$.

# Table of Contents

# Table of Figures

# Table of Figures

# Table of Tables

# 1 Introduction

## *1.1 Overview*

The aim of this project is to investigate possible reasons for the distribution of volcanic centres along the Afar rift. For this project the major focus of the investigation is how melt migrates through the mantle from melting site to surface as the cause behind the observed magmatism at the surface. In section 1.2, I discuss how the mantle composition and convection lead to the production of melt and some basics of the ensuing migration. In section 1.3, I explore two-phase fluid dynamics which can be used to describe the melt-mantle system and its evolution, covering the governing equations and what can be inferred from them. Section 1.5 discusses solitary waves in the context of a melt-mantle environment. With the basic principles summarised, I then look at the impact of the aforementioned processes in explaining volcanic phenomena seen in Afar (covered in section 1.6).

## *1.2 Mantle*

### 1.2.1 Introduction

The Earth's mantle is the largest component of the planetary volume and, above depths of ~400km, it is understood to be comprised of mostly peridotite that is at high temperatures and pressures. The temperature generally follows an adiabatic curve that increases with depth from around 1170°C at a depth of around 50km (Anderson, 1980) at around 0.4°Ckm$^{-1}$ if purely adiabatic and assuming a surface thermal boundary layer (the lithosphere). The pressure rises with depth from about 3GPa to 12GPa from 100 to 400 km. Under these great pressures and temperatures mantle peridotite undergoes creep deformation that can be approximated using a viscous constitutive flow with a viscosity in the range of $10^{19}$ and $10^{24}$Pas. Creep deformation occurs because natural crystals such as olivine, which is the main constituent mineral of peridotite along with the pyroxenes, rarely have a perfect lattice structure and usually contain small defects in

the crystal lattice. These irregularities allow the matrix to deform through two well studied mechanisms. Dislocation creep describes the macroscopic deformation of a crystal by adjustment of microscopic flaws in the crystalline lattice, allowing the configuration of atomic bonds to shift with applied stress. Diffusion creep occurs when there is a gap in the crystal lattice, which relocates by successive occupation by local atoms, allowing strain via movement of these vacancies. Over long time scales these small deformations driven by the large stresses in the mantle allow the material to act like a highly viscous fluid, the most prominent expression of which is plate tectonics driven by the convection of the mantle.

Convection of the mantle is a vital process in allowing melting to occur when the majority of the mantle is under too low a temperature and too high a pressure to allow melting. The upward motion of mantle material allows for zones where perturbations in the pressure (spreading sites), temperature (hot spots) and composition (subduction zones) allow some of the mantle component minerals to melt. At low degrees of partial melt, the melt forms a network of fluid channels distributed along the boundaries of the remaining solid crystals which form a deformable solid matrix. This thesis focuses on the question of how the melt can migrate out of the matrix to form localised concentrations of magma.

### 1.2.2 Partial melting

When the mantle melts, it does not do so in a simple, uniform manner. Most of the upper mantle is peridotite, which consists primarily of olivine, clinopyroxene and orthopyroxene along with plagioclase, all of which obey different phase change curves. This contrast in the pressures and temperatures required for each mineral to undergo a phase change to a liquid state leads to the situation in which the separate minerals melt in a sequential manner as pressure decreases or temperature rises. The Pressure-Temperature state of the mantle is perturbed towards the eutectic for the peridotite composition, clinopyroxene is the first main mineral to melt, advancing the residual rock composition towards harzburgite and lherzolite (Kelemen et al., 1997).

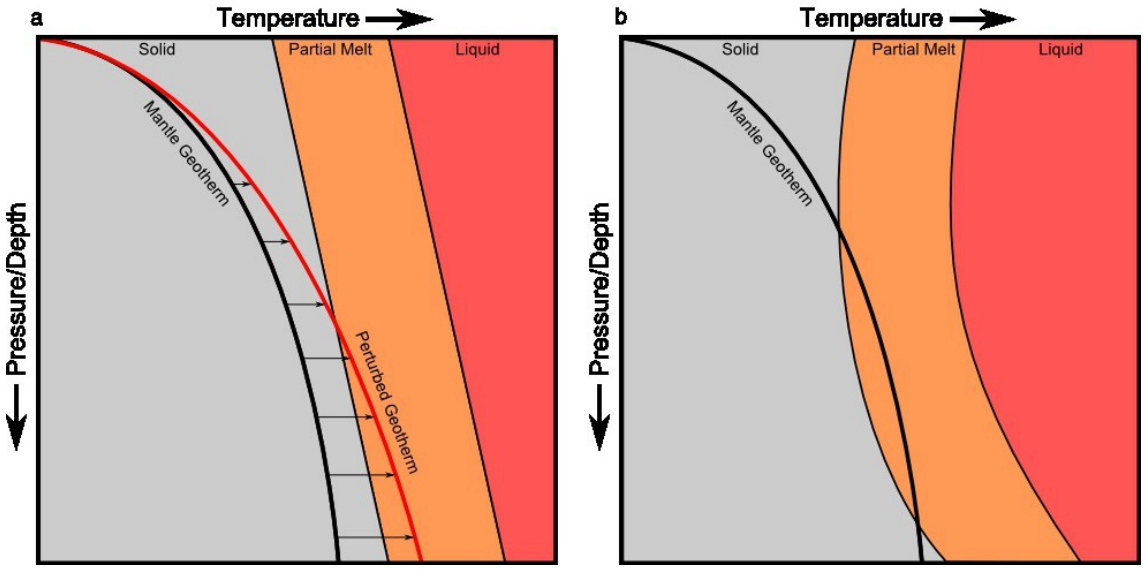


*Figure 1: The general principles of partial melting in the mantle. 1a depicts the effects of either increasing the temperature or reducing the pressure of the mantle, termed decompression melting. 1b represents a change in mantle composition such as the addition of water, which lowers the latent heat capacity of the mantle, called compositional melting. The black line represents the mantle geotherm and the coloured areas are phases of mantle rock.*

In the case of a mid-ocean ridge system, melting occurs by adiabatic decompression, where the decrease in pressure induced by mantle up flow induces the generation of partial melt at depth. Geochemical analysis of mid ocean ridge basalt shows that the material is out of equilibrium with peridotite, as deeply sourced mantle peridotite shows depletion in rare earth elements (Kelemen et al., 1997). The disequilibrium indicates that the melting must occur in small, intermittent fractions before being drawn away, never reaching large concentrations at the melting site. The rate of melting in the context of decompression melting is a smooth function of depth, reaching a maximal rate at the point where the isotherm is perturbed the most. For decompression melting that produces n-type MORB this starts at about ~80km and produces up to 9km of melting, or at ~120 km for ~23km for e-type as shown by McKenzie and O'Nions (1991).

Further geochemical analysis of MORB shows a discrepancy in the clinopyroxene content predicted by models of pure partial melting (Kelemen et al., 1995). The process proposed to explain this discrepancy is referred to as “near-fractional” melting, where melt is generated and is intermittently drawn out through a network of connected porosity in the rock. The melt fraction is indicated to be on average 3% from seismic data and it does not build up beyond ~7-13% from abyssal peridotite data matched to geochemical models by Kelemen et al., (1997).

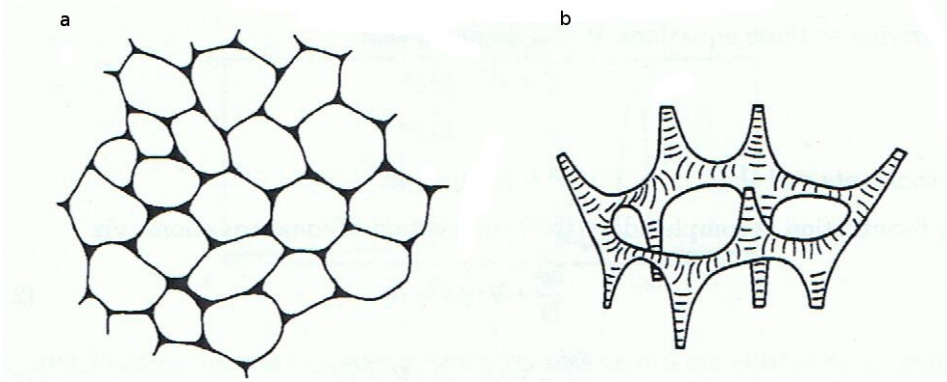


*Figure 2: A schematic view of an interconnected network of melt. 2a represents a two-dimensional slice through a three-dimensional grain network with wetted boundaries and pockets of melt. 2b is a perspective representation of a three-dimensional partial melt network. Created by Barcilon and Richter (1986).*

First, the melt grows at triple-junctions between grain corners, then along grain boundaries where the edges of grains touch, as discussed by Vaughn and Kohlstedt (1982); these wetted boundaries then grow with increased melt fraction into an interconnected network that allows separate movement of melt and matrix.

The formation of an interconnected network relies primarily on the dihedral angle of the grains, the angle between the crystals and the fluid phase filling the pore as discussed by Toramaru and Fujii (1986). If the angle is greater than 60 degrees the fluid can not enter the channels along the grain boundaries and inter-connectivity is not achieved. Dihedral angle is governed by the component minerals that make up the matrix, olivine and pyroxene predominantly for a mantle peridotite. The dihedral angle that develops from an olivine-olivine-olivine boundary lowers the wetting angle compared to boundaries with other minerals, and so the more depleted (olivine rich) the mantle rock, the higher its permeability.

### 1.2.3 Melt migration

Once the melt fraction per unit volume reaches ~0.02% (Zhu and Hirth, 2003) the melt starts to percolate upward under the forces of buoyancy. The relativity large difference between the density of mantle rock at ~3300kgm$^{-3}$ (average density of peridotite) and the melt at ~2800kgm$^{-3}$ (density of molten basalt) provides a density difference of 500kgm$^{-3}$ that drives the separation of fluid from the matrix.

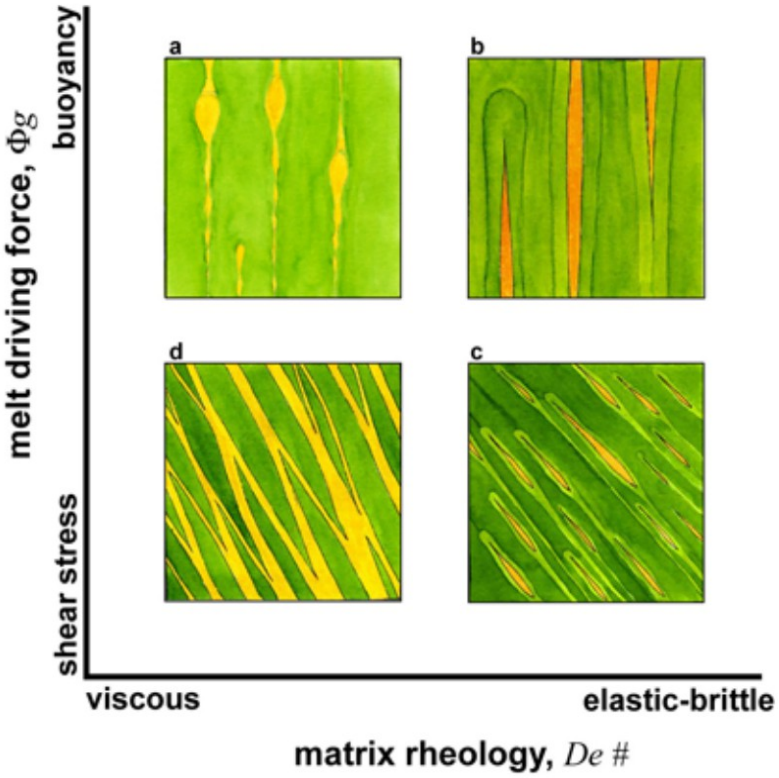


*Figure 3: Four different types of melt transport by Morgan and Holtzman (2005). The left hand diagrams depict mechanisms where the matrix is highly viscous, the fluid moving by viscous matrix deformation. The right hand graphs show mechanisms where the matrix is brittle, fracturing the dominant method for expansion and compaction. The y axis denotes the dominant driving force, where the bottom processes are driven by shear forces while the top mechanisms are driven by buoyancy forces. The mechanism shown in 3a is the one I explore in this thesis.*

Most of current research into melt migration from a numerical and analytical perspective stems from the work of McKenzie (1984) in which the main governing equations were refined for a two-phase mantle-melt system and used to analyse a system of initially constant melt fraction at an initial time. He demonstrated that there exists a length scale for a two-phase fluid system known as the compaction length over

which the fluid undergoing porous flow reaches maximum percolation velocity and above which no compaction of the matrix occurs given that the system is homogeneous in melt fraction and composition. Later using the equations from (McKenzie, 1984), Scott and Stevenson (1984) demonstrated the existence of solitary wave phenomena in a two-phase system, initialised by a melting band at the base of a one-dimensional numerical model that propagates upwards with associated expansion and compaction of the matrix above one compaction length and a possible method of concentrating melt transport. A number of studies in recent years have focused on just how an interconnected melt network in the mantle evolves upwards and focuses into magma chambers beneath the ridge system. Bercovici et al. (2001b) and Ricard et al. (2001) investigated the transition from two-phase fluid percolation to hydro-fracture and micro-cracking, exploring the role of surface tension as a possible fracturing mechanism. Others explored how the melt is concentrated in the mantle through a variety of systems: some propose shear segregation of melt, where melt is driven into concentrated bands by shear stress, as an important process (Holtzman et al., 2003; Katz et al., 2006; Rabinowicz and Toplis, 2009). While Kelemen et al. (1995, 1997) propose that the melt forms into vertical channels by a geochemical mechanism for dunite emplacement.

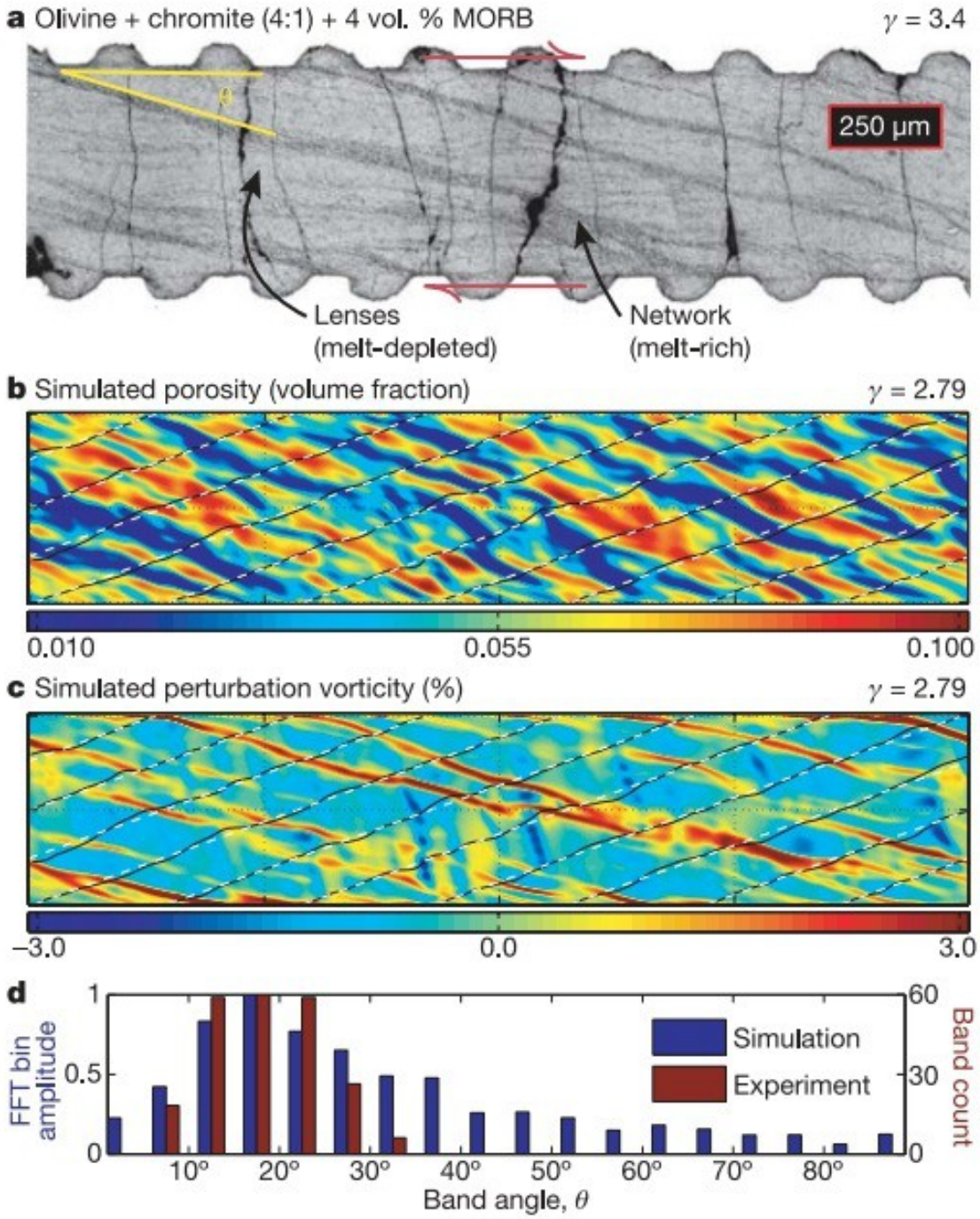


*Figure 4: Comparison of numerical and experimental results of shear driven segregation of a partially molten rock by Katz et al. (2006). The darker sloped regions in 4a are where melt has concentrated in the hot olivine-basalt-chromite aggregate when subjected to simple shear. The black dotted lines in 4b and 4c are tracer particle locations in the two-dimensional numerical model. 4c displays the total vorticity minus the constant vorticity due to simple shear. The data from 4a (experimental) and 4b (numerical) is compared in 4d to show that melt fraction concentrates into bands at low angles to the shear plane.*

Shear induced segregation during ductile deformation of the mantle is an experimentally (Holtzman et al., 2005; Katz et al., 2006) and numerically (Rabinowicz and Toplis, 2009) modelled process that occurs when a two-phase material is subjected to shear stress. The process is driven by application of shear stress in the horizontal plane to a partially molten rock, inducing the concentration of melt into bands. The process that drives this was suggested by Stevenson (1989) and confirmed through experimental work such by Holtzman et al., (2003) and Holtzman and Kohlstedt, (2007). The instability develops as the resistance to shear stresses in a two-phase fluid is highly sensitive to concentration of melt fraction. Given that the melt fraction is not perfectly homogeneous the sensitivity to stress creates a positive feedback driven by pressure gradients that concentrate the melt into isolated channels and enhancing the pressure fields in the process. These channels form angles of ~30 degrees from the perpendicular to the shear plane as demonstrated by Katz et al. (2006). Although a possible mechanism of melt segregation in the mantle, Rabinowicz and Toplis (2009) show that the process is too slow to be significant in partial melt zones due to the dissipation of stress through the fluid, but may become important towards the boundary of the viscous zone where stress becomes greater as shown by Holtzman and Kohlstedt (2007). However Rabinowicz and Toplis (2009) mention that, at the melting site, compaction will induce shear stress driven segregation in horizontal formations that will impede the percolation of melt upward, providing an instability in the vertical flow through draining of the surrounding material, due to mass conservation. These regions of melt-depletion provide a barrier to melt percolation, resulting in the formation of solitary compaction waves, discussed in section 1.5.

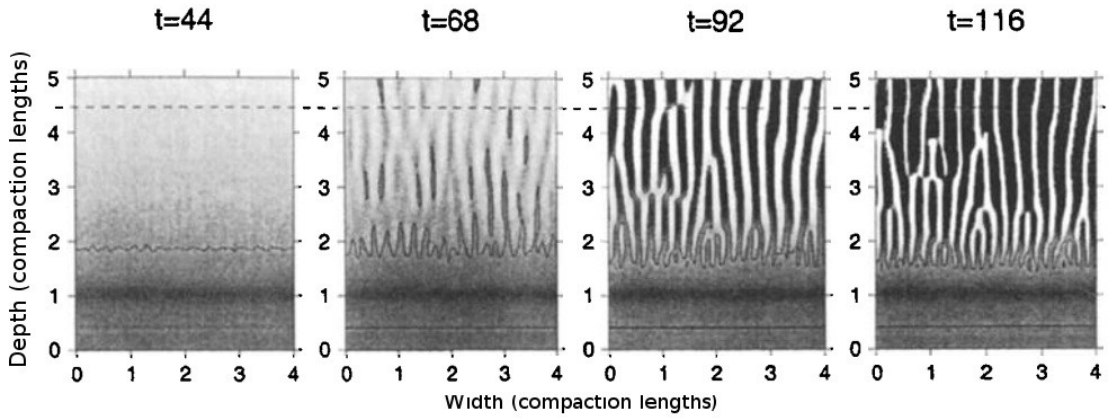


*Figure 5: Time-separated solutions for a two-dimensional two-phase numerical model by Spiegelman et al. (2001) where reactive dissolution is included. High permeability (white) channels develop with surrounding low permeability (black) areas.*

An alternative mechanism of melt separation favoured by geochemists is dunite channelisation created by reactive infiltration instability (RII). Dunite is a depleted form of mantle where olivine normal basaltic melt passes through a fertile mantle rock such as lherzolite and reactive dissolution removes pyroxene from the host rock and replaces it with olivine from the melt shifting its composition towards dunite.

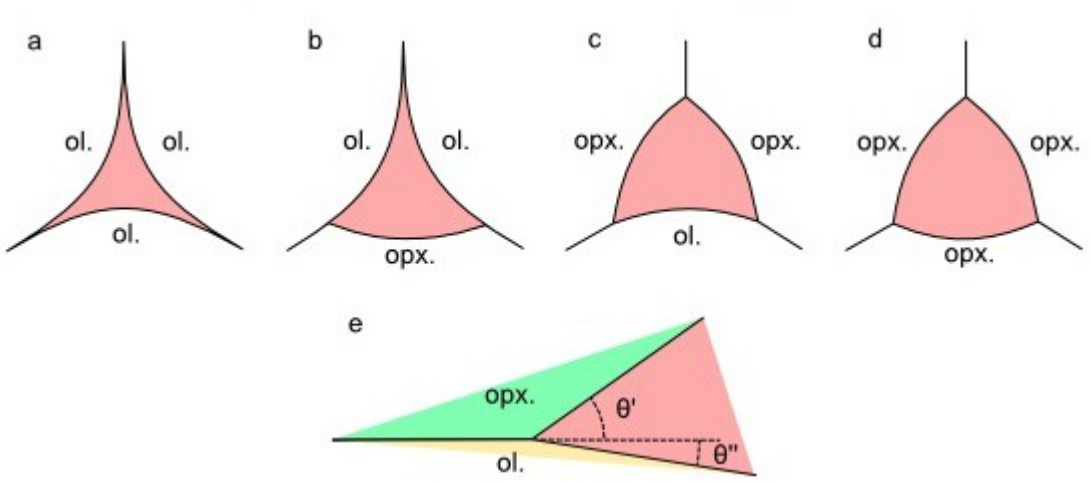


*Figure 6: Pore geometry diagrams for a partially molten rock comprised of olivine (ol.) and orthopyroxene (opx.). The associated average dihedral angles for the pores are a) 35°, b) 61°, c) 65° and d) 75°. Lower Dihedral angles equate to a higher permeability, as less fluid pressure is needed to wet the grain boundaries. Diagram e explains the dihedral angle in schematic form ($\theta_d=\theta'+\theta''$). Adapted from (Zhu & Hirth, 2003).*

The conversion to a higher concentration of olivine enhances the permeability, due to lowered dihedral angle as show in Figure 6. The dihedral angle is a consequence of the inter-facial energy of the minerals themselves. Lowered dihedral angle corresponds to increased permeability as higher dihedral angles reduce the connectivity of the fluid

network. The lowering of the dihedral angle by reactive dissolution draws in more melt, creating a geochemical feedback that generates channels of high permeability as shown in Figure 5, a mechanism that has both numerical and geological evidence behind it. The geological evidence comes from the formations of dunite found in ophiolite and peridotite massifs as shown by Kohlstedt and Holtzman (2009), 5-15% of the massifs comprising of dunite dykes or veins as indicated by Kelemen et al. (1997). Numerical experiments such as those by Schiemenz et al. (2011) back up the channelisation mechanism and focusing imposed by the change increase in porosity and grain size from the reactive dissolution.

## *1.3 Two-phase fluid dynamics*

### 1.3.1 Introduction

Given that the mantle can be modelled as a highly viscous fluid, this means the system can be represented as a two-phase fluid-fluid medium. Much research has been done into the dynamics of multi-phase systems, mostly due to applications in oil and gas exploitation. However such applications are generally represented as a solid-fluid-gas problem, which is beyond the scope of this research.

The most influential paper on two-phase fluid flow and the one that laid down the groundwork for research into the mantle-melt system was that of McKenzie (1984), who discussed subjects such as the compaction length, mass conservation and conservation of momentum, and developed a simplified formulation of the equations that describe how a two-phase system evolves and demonstrated the initial conditions and length scale of two-phase fluid systems.

Bercovici et al. (2001a,b) and Ricard et al. (2001) investigate surface tension and how it relates to transition from a viscous two-phase percolation of fluid to a brittle fluid flow. They show that the surface tension is really only important over the distance of meters but can cause melt to become locked into sill like structures in a one-dimensional model. They also mention that the surface tension can act as an intermediary to weaken the brittle material and allow fracturing.

Katz (2008) introduces the enthalpy method for the solving two-phase fluid equation,

although outside the scope of this thesis it includes equations and techniques for extending the continuum method of McKenzie (1984) with thermodynamic methods. This is done by replacing the PDE that describes the melt fraction with “a closure condition between local bulk enthalpy and bulk composition” as Katz (2008) describes it. This formulation is advantageous when working with chemical and phase change orientated research on partial melting and melt transport. Katz (2010) uses this method to explore asymmetric mantle convection due to partial melt presence and show that the presence of melt increases the likelihood of asymmetric features developing under mid-ocean ridge systems in two-dimensional numerical models.

Hewitt and Fowler (2008) look more into the boundary layers of the problem, creating a system of equations with a transition region from two-phase to a single phase numerical mantle simulation. They examine the thermal conditions of melting and freezing, modelling the system with a thermodynamic component and using pressure difference between matrix and melt as a primary variable (where most authors use velocity of the matrix). They propose that the effective pressure drops to zero at the upper boundary of the viscous mantle, generating oscillations in the pressure difference that could result in brittle fracture to allow for continued ascent of melt into the lithosphere.

Simpson et al. (2010a) derive a new set of equations using 'two scale homogenisation theory' based on a model of idealised spherical pores connected by small tubes to create a macroscopic model independent of McKenzie (1984). They show in the companion paper (Simpson et al., 2010b) that the viscosity is not substantially sensitive to the geometry of the melt network and show that this interpretation of a two-phase medium allows a better estimation of the bulk viscosity using a purely mechanical model of the medium they prescribe down to the grain scale.

### 1.3.2 Mass conservation

Conservation of mass relates any change in the fluid/matrix mass (left hand side) at any point to either motion of the material (advection) or to conversion between the phases (melting rate). As derived by McKenzie (1984):

Conservation equation for the matrix:

$$\frac{\partial \rho_m (1-\varphi)}{\partial t} = -\nabla \cdot [\rho_m \boldsymbol{V} (1-\varphi)] - \Gamma \tag{1.1}$$

Conservation equation for the melt:

$$\frac{\partial \rho_f \varphi}{\partial t} = -\nabla \cdot [\rho_f \boldsymbol{u} \varphi] + \Gamma \tag{1.2}$$

where $\rho_m$ and $\rho_f$ are the matrix and fluid densities, $\boldsymbol{u}$ and $\boldsymbol{V}$ are the fluid and matrix velocities, $\varphi$ is the melt fraction (fluid volume / total volume), $\Gamma$ is the volumetric melting rate and $t$ is time.

It is a common assumption in formulation of a two-phase fluid dynamical model applied to the interaction of mantle and melt that the densities of both the fluid and matrix are constant and not depth dependent, discussed in further detail in section 2.4.3. Using this assumption equations 1.1 and 1.2 can be combined:

$$\rho_m \frac{\partial (1-\varphi)}{\partial t} = -\rho_m \nabla \cdot [\boldsymbol{V} (1-\varphi)] - \Gamma \qquad \rho_f \frac{\partial \varphi}{\partial t} = -\rho_f \nabla \cdot [\boldsymbol{u} \varphi] + \Gamma \tag{1.3}$$

$$-\nabla \cdot [\boldsymbol{V} (1-\varphi)] - \nabla \cdot [\boldsymbol{u} \varphi] = \frac{\Gamma}{\rho_m} - \frac{\Gamma}{\rho_f} \tag{1.4}$$

Equation 1.4 is termed the combined conservation of mass equation, and it relates any mismatch in the divergence of the constituent fluids to the rate of melting. To further simplify the problem I make the assumption that no melting takes place ($\Gamma = 0$) limiting the scope to situations where melting has taken place to create the initial condition, but does not continue within the numerical simulation.

### 1.3.3 Conservation of momentum

Conservation of momentum describes the force balances involved in a two-phase system, where the first component in equation 1.5 represents the forces arising from differences between the fluid and matrix pressures, the second component governs those arising from shear stresses in the solid matrix and the final component is the main driving force for the system, buoyancy forces induced by differences between melt and matrix densities. This density difference effectively drives the migration of fluid and compaction of the matrix. As shown by Hewitt and Fowler (2008):

$$0 = -\nabla(\varphi P_f + (1-\varphi)P_m) + \nabla\cdot((1-\varphi)\boldsymbol{\tau_m}) + (\varphi\rho_f + (1-\varphi)\rho_m)g\hat{\boldsymbol{k}} \tag{1.5}$$

where $P_m$ and $P_f$ are the pressures with matrix and fluid respectively, $g$ is gravitational acceleration and $\boldsymbol{\tau_m} = \eta_m(\nabla[\boldsymbol{V}] + (\nabla[\boldsymbol{V}])^T - (2/3)\nabla\cdot[\boldsymbol{V}]\boldsymbol{I})$ where $\eta_m$ is the matrix viscosity.

To simplify equation 1.5, I assume that the fluid supports insignificant deviatoric stress. This sets $\boldsymbol{\tau_f}=0$ and is an assumption used by many authors such as Hewitt and Fowler (2008), Šrámek et al. (2007) and Bercovici et al. (2001a).

Equation 1.5 also assumes that surface tension is zero, removing a term that equates to:

$$\nabla(\sigma\alpha) = \nabla(\sigma\alpha_0\varphi^a(1-\varphi)^b) \tag{1.6}$$

where $\alpha$ is the inter-facial density, $\alpha_0$ is an inter-facial density constant and $a$ and $b$ are terms that define the fluid network geometry and are between zero and one. The importance of the fluid-matrix surface tension forces has been explored thoroughly by Bercovici et al. (2001a,b) and Ricard et al. (2001) using one- and two-dimensional numerical modelling techniques. Ricard et al. (2001) relate the importance of the surface tension forces to the buoyancy forces with the relation:

$$\frac{\sigma\alpha_0}{R\Delta\rho g} \simeq \frac{17}{R} \tag{1.7}$$

where R is the length scale of the system. The right hand side of equation 1.7 demonstrates that for length scales greater than 17m the dominant force is the buoyancy force. Given that the depth of the mantle in which partial melt exists is over the scale of kilometres, Ricard et al. (2001) indicate that surface tension could be one mechanism

for formation permeability discontinuities that trigger solitary wave formation in the mantle.

Šrámek et al. (2007) also discuss the implications of surface tension on the Clapeyron slope. Experimental studies such as that by Parsons et al. (2008) show that for small length scale problems, relating to small planetary bodies on the ~15km radius, surface tension is a factor in melt segregation but for larger bodies such as the earth, surface tension is a small force in comparison with buoyancy or shear. With these factors in mind I choose to assume zero surface tension to simplify the problem.

### 1.3.4 Darcy's law

Darcy's law is used to define the rate of transport of fluid through a permeable medium. This version deals with a medium in which the fluid velocity is defined relative to a matrix which deforms also but has a much greater viscosity than that of the fluid:

$$\varphi(\boldsymbol{u}-\boldsymbol{V}) = -\frac{k_\varphi}{\eta_f}\nabla(P_f - \rho_f g\vec{\boldsymbol{z}}) \tag{1.8}$$

where $\eta_f$ is the fluid viscosity and $k_\varphi$ is the specific permeability (see 1.3.5).

### 1.3.5 Specific permeability

Permeability is assumed to be a simple function of melt fraction φ according to Hewitt and Fowler (2008):

$$k_\varphi \sim \frac{a^2\phi^n}{b} = k_o\phi^n \tag{1.9}$$

where *n* is an empirically derived power law exponent that may depend on the type of interconnected fluid network, *a* is the typical grain diameter of the matrix, and *b* is a tortuosity factor which represents how indirect is the path between two pockets of melt on the grain scale.

The power *n* relates to how the fluid channels connect together, constrained by the dihedral angle of the grain intersections. Zhu and Hirth (2003) showed that a value of $n \approx 2$ arises for a model environment of tessellated grains, with a homogeneous network of connections along the grain boundaries. Unfortunately lab experiments using olivine based aggregates by Zhu et al. (2011) or quartz and calcite aggregate by Wark and

Watson (1998) do not completely agree with numerical and analytical experiments determining a value of $n \approx 3$. Zhu and Hirth (2003) attribute the differences in empirical values of $n$ to micro-scale heterogeneity, which are not really applicable to earth materials when examined over the macroscopic-scale.

Although the value of $n$ is still undergoing research, the general form of the equation 1.9 is widely used with the choice of $n$ varying between 2-3 for different authors. For this investigation I use the parameter $n=2$ in all future occurrences of $n$, following Hewitt and Fowler, (2008) and Šrámek et al. (2007) who also use this value of $n$.

### 1.3.6 Viscosity power law

The viscosity of the matrix has been empirically shown to be dependant on the melt fraction (Kohlstedt and Zimmerman, 1996) and can be expressed as the power law (Nakayama and Mason, 1992):

$$\eta_m = \frac{\eta_0}{\varphi^m} \tag{1.10}$$

Many authors, such as Barcilon and Richter (1986); Takashi and Satsuma (1988) and Scott and Stevenson (1986) use the assumption that $m=0$ to significantly simplify the problem which is within the range of predicted values for $m$, $0<m<1$ as shown by Scott and Stevenson (1986). For these reasons I also assume that $m=0$ for simplification and so that $\eta_m$ is a constant.

### 1.3.7 Compaction rate

McKenzie (1984) and Spiegelman (1993a) use the following formula to describe how pressure differences between matrix and fluid result in compaction of the matrix:

$$(P_m - P_f) = -\zeta_m \nabla \cdot ((1-\varphi)\boldsymbol{V}) \tag{1.11}$$

However, more recently Hewitt and Fowler (2008) described equation 1.11 as more a definition of bulk viscosity than a way to relate pressure to matrix divergence.

To do so, they constructed a model fluid network made up of tubules of radius *a* and state that the walls of these cylinders will expand via melting of the matrix and contract by viscous creep at the rate of $\pi a^2(P_m - P_f)/\eta_s$ which can be expressed as:

$$2\pi a\frac{da}{dt} = \frac{\Gamma}{\rho_m} - \frac{\pi a^2}{\eta_m}(P_m - P_f) \tag{1.12}$$

If the width of each tube is associated with permeability $\pi a^2 = \varphi$ and by applying the product rule 1.12 becomes:

$$2\pi a\frac{da}{d\varphi}\frac{d\varphi}{dt} = \frac{\Gamma}{\rho_m} - \frac{\pi a^2}{\eta_m}(P_m - P_f) \tag{1.13}$$

$$\frac{da}{d\varphi} = \frac{d}{d\varphi}\sqrt{\frac{\varphi}{\pi}} = \frac{1}{2}\frac{1}{\sqrt{\varphi\pi}} = \frac{1}{2}\frac{1}{\sqrt{\pi^2 a^2}} = \frac{1}{(2\pi a)} \tag{1.14}$$

$$\frac{d\varphi}{dt} - \frac{\Gamma}{\rho_m} = -\frac{\varphi}{\eta_m}(P_m - P_f) \tag{1.15}$$

Substituting equation 1.1 into equation 1.15, using the constant density assumption:

$$(P_m - P_f) = -\frac{\eta_m}{\varphi}\nabla\cdot((1-\varphi)\boldsymbol{V}) \tag{1.16}$$

Equation 1.16 provides a necessary relationship between the matrix-fluid pressure difference and the compaction rate of the matrix. Other authors such as Šrámek et al. (2007) also produce similar formulations from different starting assumptions, further reinforcing this relation.

### 1.3.8 Potential form

To make manipulation of the equations involving matrix velocity simpler, I use the potential function formulation to describe the velocity field of the solid, creeping matrix:

$$\boldsymbol{V} = \nabla\times[\boldsymbol{A}] + \nabla[B] \tag{1.17}$$

where $\boldsymbol{A}$ is the vector potential and $B$ is the scalar potential. A common simplification for this equation when considering incompressible fluid flow is:

$$\boldsymbol{V} = \nabla\times[\boldsymbol{A}] \tag{1.18}$$

As the vector potential $\boldsymbol{A}$ is associated with incompressible movements in the field while

the scalar potential deals with the compressible components. This separation allows for simplification of this equation by removing the *B* component whenever the fluid is incompressible. In the case of a two-phase system however, the matrix is effectively compressible in response to changes in the melt fraction, so the scalar potential remains an important part of the system. The separation of compressible and incompressible parts of the flow field is valuable since only the former component contributes to melt extraction.

## *1.4 Initially constant melt fraction problem*

### 1.4.1 Introduction

The simplest problem to solve in a two-phase fluid problem is an initially constant melt fraction over all depth. This is the initial problem explored by McKenzie (1984) and Richter and McKenzie (1984), examining the initial velocities of melt and matrix generated in a two-phase fluid field at initialisation. McKenzie (1984) demonstrates that compaction of the matrix initially only takes place over the “compaction length”, a specific depth range starting at the base of the column of melt where there are no forces to resist the compaction. This lessens vertically until a point is reached where the weight of the matrix is supported by the upward flow of melt.

Evolution of an initial constant melt fraction is explored by Richter and McKenzie (1984) and Spiegelman (1993b), an example shown in Figure 7. This demonstrates that the initial compaction takes place over the compaction length at the base of the medium, but as the region evolves the compaction spreads vertically as melt flows out of the top of the region.

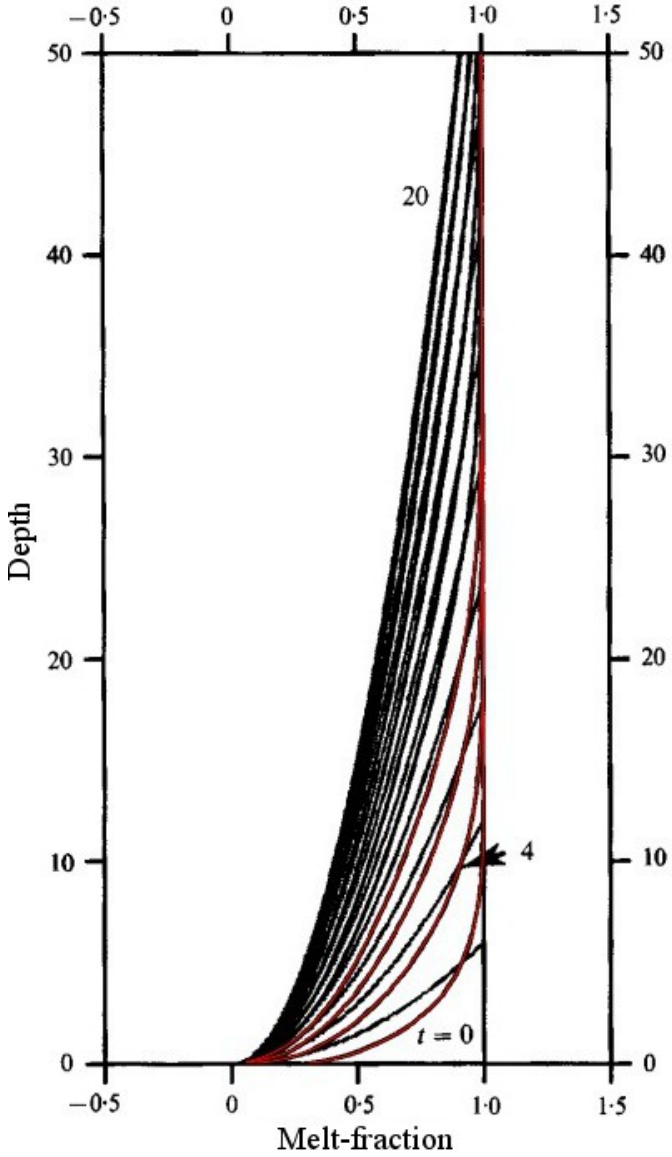


*Figure 7: Solutions to one-dimensional numerical and analytical models for an initially constant melt fraction by Speigelman (1993b). The black lines are analytical and numerical solutions at different time-steps, with the initial condition a constant ($\varphi/\varphi_0$=1.0), red lines highlight the first four numerical solutions for incremental time-steps while the black line at 1.0 is the initial condition.*

This simple percolation problem of an initially constant melt fraction does not require investigation outside of use as a test. It's use as a test allows comparison of analytical solutions to those of numerical solutions. If a barrier to flow of melt exists, such as reduced permeability, solitary waves will be generated as demonstrated by Spiegelman (1993b) and shown in Figure 8.

## *1.5 Solitary waves*

### 1.5.1 Introduction

Solitary waves were first discovered by John Scott Russell in the Union Canal in Scotland who termed these pulses solitons, expressed as local elevation in the water level that travelled along the canal for many kilometres with no observed changes in amplitude or wavelength. In Russell's case he was observing a solitary wave in water, but these waves emerge in many different areas of physics, showing up in fibre-optics, magnetic fields and many other systems governed by weakly non-linear dispersive partial differential equations.

For the two-phase melt-mantle problem, solitary waves arise when a barrier to flow of melt exists, such as a perturbation to the background melt fraction from the constant problem (section 1.4). Barcilon and Richter (1984) show that this barrier generates a pressure field that in turn forms the solitary wave, with positive pressure expanding the matrix and negative contracting it again, controlled by the buoyancy, friction, pressure gradient and conservation of mass.

Many authors have explored magma-melt solitary waves in one dimension e.g. (Marchant and Smyth, 2005; Barcilon and Richter, 1986 Richter and McKenzie, 1984; Spiegelman, 1993a-c; Scott and Stevenson, 1984; Nakayama and Mason, 1992, 1995, 1999), two dimensions (Richardson, 1998; Barcilon and Lovera, 1989; Connolly and Podladchikov, 2007) and even three dimensions (Wiggins and Spiegelman, 1995). However, there has been little headway in experimental proof that magmatic solitary waves or 'magmons' appear in the mantle, although they are predicted to arise with relative ease from conditions expected to occur in zones of partial melting and upward percolation of melt.

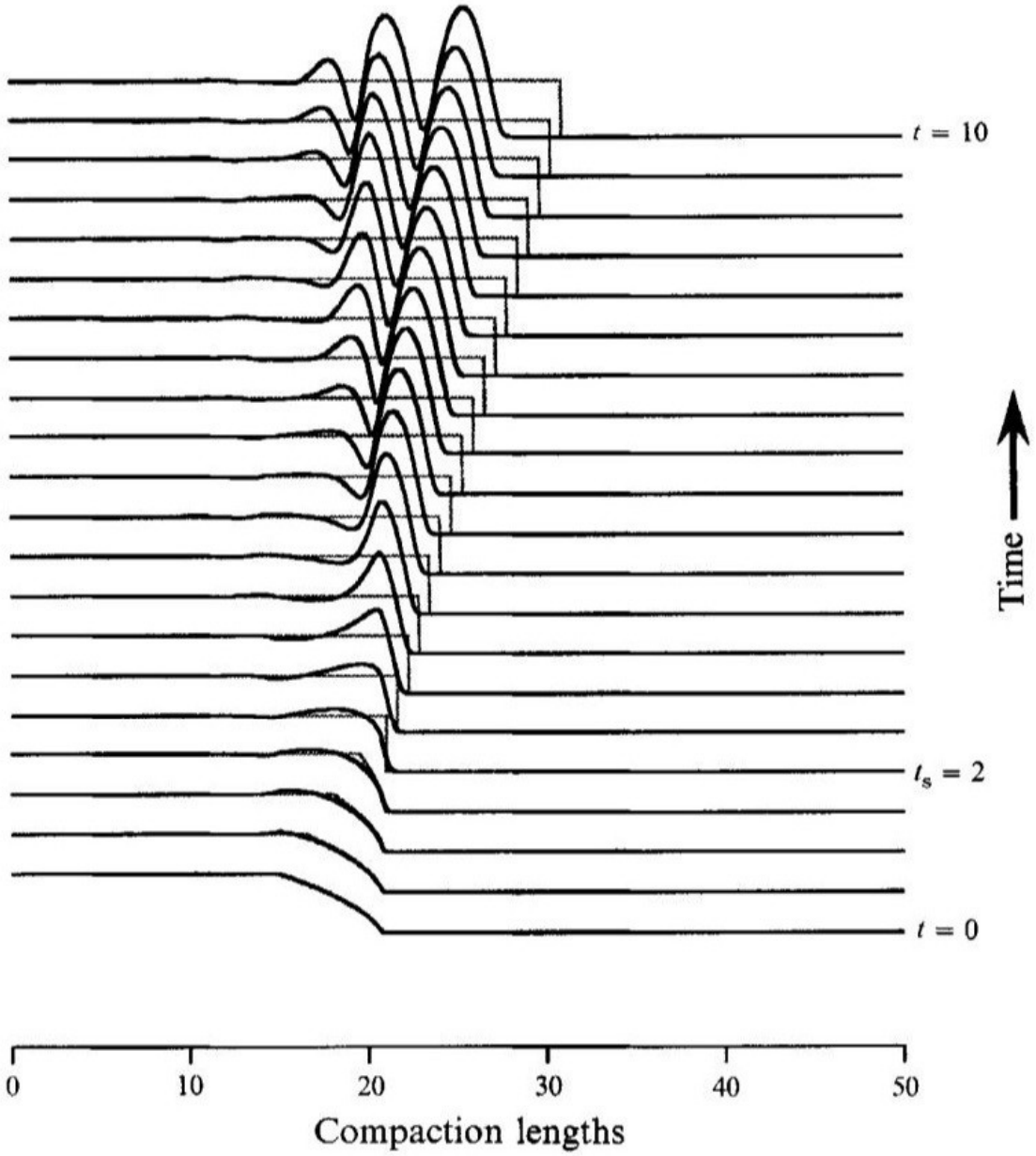


*Figure 8: Numerical solutions to an initial sigmoid function of melt fraction. Two solutions are shown at incremental time steps vertically, the zero-compaction length solution generates the sharp shock-wave while the standard numerical solution generates a train of solitary waves, both solutions overlapping. From Spiegelman (1993b).*

The term magmon comes from Scott and Stevenson (1984), as the waves were originally believed to be solitons. However, Barcilon and Richter (1986) showed that solutions, both analytical and numerical, did not fit the requirements of this label. Firstly, magma solitary waves do not obey an infinite number of conservation laws. Secondly, they do not emerge from wave-wave interaction with no change to themselves or the surrounding medium; they instead flow into one another, the material from the

lower, larger wave inflating the one above, giving the illusion of changing places. They also show that solitary wave velocity is proportional to the amplitude and that in a solitary wave collision the amplitudes of the waves swap positions rather than pass through each other. Wiggins and Spiegelman (1995) examine a highly simplified three-dimensional numerical solution to a two-phase problem and show that solitary waves of one- and two-dimensional form are unstable in a three-dimensional problem and devolve into spherical solitary waves. Other authors such as Barcilon and Richter (1986); Bercovici et al. (2001a,b); Ricard et al. (2001); Spiegelman (1993a); Simpson et al. (2010a,b); Ŝrámek et al. (2007) have produced amended formulations and explored the phenomena that occur in a two-phase system in more depth.

### 1.5.2 Governing equations

Solitary waves arise from the direct relationship between the melt fraction and the permeability as indicated by Barcilon and Richter (1986), which is shown in equation 1.9. In an initially constant melt fraction system, such as Figure 7 where solitary waves are not generated as a constant pressure gradient counteracts the buoyancy forces driving the percolation of melt. If, however, a perturbation is introduced in the form of an increased melt fraction, the pressure acting on the solid matrix is increased beyond the balance and induces increased downward flow of matrix. To balance this, there is an increase in the upward flow of melt, translating the melt fraction perturbation upwards and continuing the cycle. The forces driving solitary waves in compacting media are the buoyancy force incurred by the difference between the matrix and fluid densities while the restoring force is a result of the viscous compaction of the matrix required to conserve mass.

Spiegelman (1993a) shows that the wave phase velocity is related to the vertical gradient of the permeability function, expressed as $\omega \propto \partial k_{\varphi} / \partial \varphi$ arising from the velocity and divergence of fluid flux. He shows that solitary waves are defined by the "porosity shock" from which they are generated, such that larger obstructions to melt flow generate larger solitary waves. He also demonstrates that solitary waves can develop into sharp discontinuities known as shock waves, if the compaction length is assumed to be zero and provides two-dimensional numerical solutions, showing that

stable solitary waves are of cylindrical form in a two-dimensional problem.

Nakayama and Mason (1995) investigated the importance of the two main controlling constants of the permeability and viscosity dependences on the melt fraction of the system (*n* and *m* in equations 1.9 and 1.10 respectively). They showed that for solitary waves to form in a two-dimensional system, $n > 1$; that the width of the solitary wave is inversely proportional to the square root of the wave amplitude; and that the phase velocity of the solitary wave is a linear function of the wave amplitude.

## *1.6 Afar*

### 1.6.1 Introduction

Afar is a region of North East Ethiopia that is the site of an active triple-junction for the Aden Ridge, East African Rift and the Red Sea Rift. Mantle up-welling under the triple junction drives the divergence of the plates and thins the lithosphere, producing partial melt from decompression melting and large offset faults to accommodate stress at the surface. The majority of divergent ridge systems are submerged, making Afar a prime location to study active rifting and the mechanism of continental breakup above water.

Geochemical data by Wolfenden et al. (2004) indicate that the rift has formed over the last ~31 million years (Myr), while extension of the rifts started between about 11-17Myr. The majority of the surface geology however is significantly more recent due to its magmatic origin and extends over an area around ~300km wide (Wright et al., 2006) around the northern rift axis. Research by Nooner et al., 2009 supports the theory of a thinned crust and lithosphere overlying an up-welling mantle, resulting in decompression melting and partial melt at depths of ~53-88km (Roony et al., 2005) along the rift axis.

In September 14$^{th}$ 2005 a large-scale dyke event took place along the Dabbahu rift segment in Afar. This activity was associated with a magnitude ($M_b$) ~4.7 earthquake and over the following 10 days the rift opened with a sequence of fissure eruptions and an eight metre offset. Geodetic study of this dyke event by Hamling et al. (2009) has indicated that since initiation, there has been 13 basaltic dyke emplacements totalling to a width of greater than 8m. To study this activity the NERC funded Afar Rift

Consortium was formed, employing an interdisciplinary group from several university's to work towards fully analysing the Dabbahu rift segment, of which this project is part. The role of this project was to investigate a possible deep process control on the segmentation of volcanic activity along the Dabbahu rift.

### 1.6.2 Rift segmentation

Rift segmentation describes the distribution of volcanic activity along the axis of a rift, where activity is concentrated into discrete segments with gaps of minimal activity separating them.

Rift segmentation is a phenomenon observed in Afar as well as at mid-ocean ridges such as the Mid-Atlantic Ridge (Sempéré et al., 1993) and rift systems like Iceland (Thordarson and Larsen, 2007). The segmentation in Afar specifically is expressed as patches of volcanic activity, forming chains around 50-80km long shown by Hayward and Ebinger, (1996) to be spread out along the rift axis in discrete segments that are often offset along strike.

Many explanations for the existence of segmentation in both faulting and magmatic activity have been suggested. One possibility is that the segmentation is a natural length scale of the plate system itself as suggested by Mohr and Wood (1976) and Ebinger (1989). McConnell (1972) suggested that the structure of the plate itself could be the cause of offset rift segments, with variation in mechanical strength producing the separation of magmatic sites. Whitehead et al., (1984) propose that the up-welling mantle velocity fields are the mechanism for segmentation, with up-welling of the mantle under each volcanically active segment and a gap of either down-welling or stagnant mantle between.

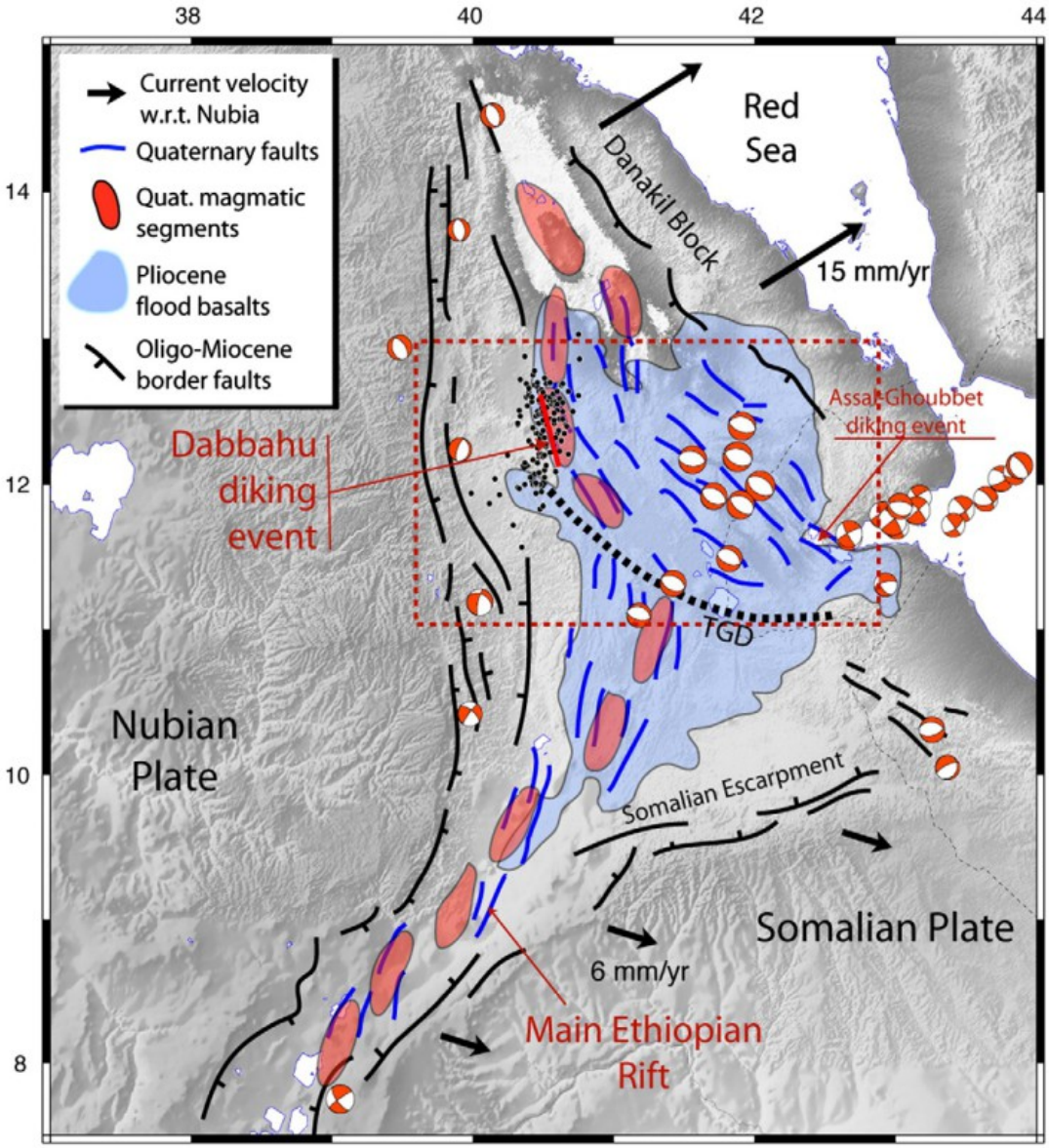


*Figure 9: Magmatic segments of the Afar triple junction between the southern Red Sea, Main Ethiopian Rift, and westernmost Gulf of Aden Rift systems by Beutel et al. (2010). The magmatic activity is depicted by the red patches along the rift, highlighting the segmentation of volcanism.*

Investigating the segmentation of the Afar rift in particular, Hayward and Ebinger (1996) hypothesised that the rifting length scales (of ~1km) are in part dependent on the mechanical properties of the rifting plate while the longer length scale features such as segmentation of volcanic activity are a function of periodicity in mantle up-welling.

## 1.7 Thesis outline

In this thesis, I endeavour to relate the segmentation of magmatic activity (Figure 9) along rifting sites, such as Afar, to solitary waves that enforce a length scale on the percolation of melt from the zone of partial melting in the viscous mantle. I will also examine the implications and links between solitary wave train time-scales and the eruptive cycles of volcanic complexes.

I plan to explore this concept in two major parts. First, I will explore the governing equations in search of a set of solvable equations that can be utilised in a numerical model to explore modes of compaction and melt migration in this two-phase system.

In chapter 3, I describe the construction of a one-dimensional two-phase fluid model for evaluation and investigation of the basic principles of a two-phase system and the behaviour and phenomena associated with solitary waves using dimensional constants that are relevant to the extraction of melt from the upper mantle.

Following this one-dimensional model, in chapter 4 I move on to discussing implementation of a three-dimensional model in order to investigate how the spatial distribution of melt, analogous to a rift axis, evolves with time.

This thesis concludes with a discussion of insights gleaned from the aforementioned numerical experiments regarding the mechanism that influences the spatial periodicity in mantle up-welling in the rifting environment. I will also discuss possible future applications for the numerical models developed here and what other avenues of research have been opened up by this investigation.

# 2 Mathematical Model

## *2.1 Introduction*

In this chapter, I look at how the governing equations set out in section 1.3 can be reworked into a set of solvable equations to be used in construction of a functional numerical model of two-phase fluid flow. Starting with the governing equations in section 2.2, I describe the simplifying assumptions whose validity will be further discussed in section 2.4. Essentially the evolving system is described by the two key variables of melt fraction φ and matrix velocity $\boldsymbol{V}$ and the spatial variation of the variables. The matrix deforms because of buoyancy forces due to the density difference between matrix and solid. Based on the Helmholtz decomposition, the velocity field can be expressed using two potential functions:

$$\boldsymbol{V} = \nabla \times [\boldsymbol{A}] + \nabla [B] \tag{2.1}$$

The vector potential $\boldsymbol{A}$ describes the part of the velocity field which is incompressible. The scalar potential $B$ describes the curl-free part of the flow field. In constructing a general formulation, I apply non-dimensionalisation in section 2.5 to produce a set of three governing equations on which a numerical algorithm can be based.

The mathematical model of a two-phase system evolves from an *a priori* distribution of the melt fraction and the physical properties of the matrix and fluid; density and viscosity. The evolution of the system is constrained by the principles of conservation of mass and momentum.

For a given spatial distribution of the melt fraction, an equation that defines the variation of matrix velocity is derived from the conservation of momentum constraint. Conservation of mass then provides an equation which governs the rate of change of melt fraction everywhere.

The model derived in this section is similar to that presented by Spiegelman (1993a), with the equations for $\boldsymbol{A}$ and the time-step identical before non-dimensionalisation. The $D$ ( $\nabla\cdot\boldsymbol{V}$ ) equation however has significant differences. The contrast between the $D$ equations arises from my choice of assumptions. First, I do not use a separate bulk viscosity term like Spiegelman (1993a), using the approach by Hewitt and Fowler (2008) of one viscosity constant. I also use the small-melt fraction equation to a far lesser extent. This results in the formulation of the $D$ equation shown in section 2.3.2.

## *2.2 Restatement of governing equations*

For ease of reference with respect to the forthcoming derivations, I first restate the conservation laws and other formulae previously defined in section 1.3. The equations shown here are simplified using the approximations described in section 2.4 to improve the solvability of the two-phase system. It should be remembered, however, that in so doing I render the resulting mathematical and numerical models possibly inapplicable to more general systems, including for example systems in which viscosity or density vary with depth.

**Conservation of Matrix Mass**

From (1.1) assuming no melting or freezing and constant matrix density.

$$\frac{\partial\varphi}{\partial t} - \nabla\cdot[(1-\varphi)\boldsymbol{V}] = 0 \tag{2.2}$$

**Combined mass conservation**

From (1.4) assuming constant matrix and fluid density.

$$\nabla\cdot[\boldsymbol{V}]+\nabla\cdot[\varphi(\boldsymbol{u}-\boldsymbol{V})] = 0 \tag{2.3}$$

**Conservation of Momentum**

From (1.5) assuming that inertial terms are negligible and the fluid supports no deviatoric stress.

$$-\nabla[(1-\varphi)P_m+\varphi P_f]+\nabla\cdot[(1-\varphi)\boldsymbol{\tau_m}]+((1-\varphi)\rho_m+\varphi\rho_f)g\hat{\boldsymbol{k}} = 0 \tag{2.4}$$

**Darcy's Law**

From (1.8) assuming a specific dependence of permeability on melt fraction as defined by (1.9).

$$\varphi(\boldsymbol{u}-\boldsymbol{V}) = -\frac{k_o \varphi^n}{\eta_f}\nabla[P_f - \rho_f g z] \tag{2.5}$$

**Permeability Function**

Restating (1.9).

$$k_\varphi \sim \frac{a^2 \varphi^n}{b} = k_0 \varphi^n \tag{2.6}$$

**Compaction Equation**

From (1.11) based on a conceptual model for the contraction or expansion of the connected fluid volume.

$$\Delta P = -\frac{\eta_m}{\varphi}\nabla\cdot[(1-\varphi)\boldsymbol{V}] \qquad \text{where: } \Delta P = P_m - P_f \tag{2.7}$$

**Deviatoric Stress Tensor**

Assuming bulk viscosity equals shear viscosity and is constant.

$$\boldsymbol{\tau_m} = \eta_m(\nabla[\boldsymbol{V}] + (\nabla[\boldsymbol{V}])^T - \frac{2}{3}\nabla\cdot[\boldsymbol{V}]\boldsymbol{I}) \tag{2.8}$$

**Divergence of the matrix velocity field**

Follows from application of the divergence operator to equation 2.1.

$$D = \nabla\cdot[\boldsymbol{V}] = \nabla^2[B] \tag{2.9}$$

**Vector Calculus Identities**

$$\nabla\cdot[\nabla\cdot[\boldsymbol{a}]\mathbf{I}] = \nabla[\nabla\cdot[\boldsymbol{a}]] \tag{2.10}$$

$$\nabla\cdot[\nabla[\boldsymbol{a}] + (\nabla[\boldsymbol{a}])^T] = \nabla^2[\boldsymbol{a}] + \nabla[\nabla\cdot[\boldsymbol{a}]] \tag{2.11}$$

$$\nabla^2[\boldsymbol{a}] = \nabla[\nabla\cdot[\boldsymbol{a}]] - \nabla\times[\nabla\times[\boldsymbol{a}]] \tag{2.12}$$

$$\nabla^2[a\ b] = a\nabla^2 b + b\nabla^2 a + 2\nabla a\cdot\nabla b \tag{2.13}$$

$$\nabla\times[\nabla[a]] = 0 \tag{2.14}$$

$$\nabla\cdot[\nabla\times[\boldsymbol{A}]] = 0 \tag{2.15}$$

$$\nabla\cdot[\boldsymbol{a}\,b]=\nabla[b]\cdot\boldsymbol{a}+b\nabla\cdot[\boldsymbol{a}] \tag{2.16}$$

For derivations of 2.10 and 2.11 see appendix (7.2).

## *2.3 Derivation of 3D equations*

### 2.3.1 Derivation of an equation for *A*

To obtain an equation for the matrix velocity, or equivalently its vector potential ***A*** and scalar potential *B*, I begin with the conservation of momentum 2.4 and substitute in deviatoric stress term $\boldsymbol{\tau}_m$ (2.8) in terms of viscosity and velocity gradients:

$$\begin{gathered}-\nabla[(1-\varphi)P_m+\varphi P_f]+\nabla\cdot[(1-\varphi)(\eta_m(\nabla[\boldsymbol{V}]+(\nabla[\boldsymbol{V}])^T-\frac{2}{3}\nabla\cdot[\boldsymbol{V}]\boldsymbol{I}))] \\ +((1-\varphi)\rho_m+\varphi\rho_f)g\hat{\boldsymbol{k}}=0\end{gathered} \tag{2.17}$$

I now use the small-φ approximation, as used by authors including Hewitt and Fowler (2008), Spiegelman (1993a), Richardson et al. (1996), Ribe (1985) and Barcilon and Richter (1986). I will discuss this assumption further in section 2.4.1). I simply assume that the melt fraction is very small and as such $1-\varphi\approx 1$ in computing the divergence of stress in equation 2.17 along with the assumption that matrix viscosity is constant in time and space to obtain the following simplified equation:

$$\begin{gathered}-\nabla[(1-\varphi)P_m+\varphi P_f]+\eta_m\nabla\cdot[\nabla[\boldsymbol{V}]+(\nabla[\boldsymbol{V}])^T-\frac{2}{3}\nabla\cdot[\boldsymbol{V}]\boldsymbol{I}] \\ +((1-\varphi)\rho_m+\varphi\rho_f)g\hat{\boldsymbol{k}}=0\end{gathered} \tag{2.18}$$

The small melt fraction assumption considerably simplifies the following equations.

Using the identity 2.10 to simplify 2.18:

$$\begin{gathered}-\nabla[(1-\varphi)P_m+\varphi P_f]+\eta_m\nabla\cdot[\nabla[\boldsymbol{V}]+(\nabla[\boldsymbol{V}])^T]-\eta_m\frac{2}{3}\nabla[\nabla\cdot[\boldsymbol{V}]] \\ +((1-\varphi)\rho_m+\varphi\rho_f)g\hat{\boldsymbol{k}}=0\end{gathered} \tag{2.19}$$

Then, substituting the identity 2.11 into equation 2.19:

$$\begin{gathered}-\nabla[(1-\varphi)P_m+\varphi P_f]+\eta_m(\nabla^2[\boldsymbol{V}]+\nabla[\nabla\cdot[\boldsymbol{V}]]-\frac{2}{3}\nabla[\nabla\cdot[\boldsymbol{V}]]) \\ +((1-\varphi)\rho_m+\varphi\rho_f)g\hat{\boldsymbol{k}}=0\end{gathered} \tag{2.20}$$

Substitution of identity 2.12 into equation 2.20 produces:

$$-\nabla[(1-\varphi)P_m+\varphi P_f]-\eta_m\nabla\times[\nabla\times[\boldsymbol{V}]]+\eta_m\frac{4}{3}\nabla[\nabla\cdot[\boldsymbol{V}]] +((1-\varphi)\rho_m+\varphi\rho_f)g\hat{\boldsymbol{k}}=0 \tag{2.21}$$

Taking the curl of equation 2.21 all gradient terms become zero following the identity 2.15:

$$\eta_m\nabla\times[\nabla\times[\nabla\times[\boldsymbol{V}]]]=\nabla\times[((1-\varphi)\rho_m+\varphi\rho_f)g\hat{\boldsymbol{k}}] \tag{2.22}$$

Which eliminates pressure, leaving an equation for matrix velocity $\boldsymbol{V}$ in terms of buoyancy forces produced by the difference between fluid and matrix density. Substituting equation 2.1 into equation 2.22, and using identity 2.12 an equation for the vector potential is obtained:

$$\nabla^4[\boldsymbol{A}]=\frac{g}{\eta_m}\nabla\times[((1-\varphi)\rho_m+\varphi\rho_f)\hat{\boldsymbol{k}}] \tag{2.23}$$

Since both densities are assumed constant, (2.23) can be rearranged into:

$$\nabla^4[\boldsymbol{A}]=-\frac{\Delta\rho\, g}{\eta_m}\nabla\times[\varphi\hat{\boldsymbol{k}}] \tag{2.24}$$

where $\Delta\rho=\rho_m-\rho_f$.

Equation 2.24 is a fourth-order partial differential equation known as the biharmonic equation. Given a known distribution of melt fraction φ, equation 2.24 with appropriate boundary conditions determines the vector potential, one of the two essential components of the matrix velocity field. This equation is identical to that derived by Spiegelman (1993a) and was the inspiration behind the adoption of TDCON. The derivation is fully explained here as several steps had to be re-derived to account for minor differences between the governing equations used here and those used by Spiegelman (1993a).

### 2.3.2 Derivation of an equation for *D*

To determine the other part of the velocity field a comparable equation for the scalar potential *B* is required. Returning to equation 2.17:

$$-\nabla[(1-\varphi)\Delta P]+\nabla\cdot[(1-\varphi)\eta_m(\nabla[\boldsymbol{V}]+(\nabla[\vec{\boldsymbol{V}}])^T-\frac{2}{3}\nabla\cdot[\boldsymbol{V}]\boldsymbol{I})] \\ +(1-\varphi)\Delta\rho g\hat{\boldsymbol{k}}-\nabla[P_f]+\rho_f g\hat{\boldsymbol{k}}=0 \tag{2.25}$$

where $\Delta P=P_m-P_f$ and $\Delta\rho=\rho_m-\rho_f$. This step was interpreted from work by Šrámek et al. (2007). The last two terms in equation 2.25 may be replaced using Darcy's law (equation 2.5) to produce:

$$-\nabla[(1-\varphi)\Delta P]+\nabla\cdot[(1-\varphi)\eta_m(\nabla[\boldsymbol{V}]+(\nabla[\boldsymbol{V}])^T-\frac{2}{3}\nabla\cdot[\boldsymbol{V}]\boldsymbol{I})] \\ +(1-\varphi)\Delta\rho g\hat{\boldsymbol{k}}+\frac{\eta_f}{k_o\varphi^n}\varphi(\boldsymbol{u}-\boldsymbol{V})=0 \tag{2.26}$$

Removing the remaining term in pressure by substituting the compaction equation (equation 2.7), much like Spiegelman (1993a), produces:

$$\nabla[(1-\varphi)\frac{\eta_m}{\varphi}\nabla\cdot[(1-\varphi)\boldsymbol{V}]] \\ +\eta_m\nabla\cdot[(1-\varphi)(\nabla[\boldsymbol{V}]+(\nabla[\boldsymbol{V}])^T-\frac{2}{3}\nabla\cdot[\boldsymbol{V}]\boldsymbol{I})] \\ +(1-\varphi)\Delta\rho g\hat{\boldsymbol{k}}+\frac{\eta_f}{k_o\varphi^n}\varphi(\boldsymbol{u}-\boldsymbol{V})=0 \tag{2.27}$$

As previously applied to obtain equation 2.18, again I use the small melt fraction approximation to simplify equation 2.27 by setting $1-\varphi\approx 1$ in both of the terms that are acted on by divergence operators:

$$\eta_m\nabla[\frac{1-\varphi}{\varphi}\nabla\cdot[\boldsymbol{V}]]+\eta_m\nabla\cdot[\nabla[\boldsymbol{V}]+(\nabla[\boldsymbol{V}])^T-\frac{2}{3}\nabla\cdot[\boldsymbol{V}]\boldsymbol{I}] \\ +(1-\varphi)\Delta\rho g\hat{\boldsymbol{k}}+\frac{\eta_f}{k_o\varphi^n}\varphi(\boldsymbol{u}-\boldsymbol{V})=0 \tag{2.28}$$

I do not remove the first (1- φ) term in equation 2.28 as it only results in a slight change in a single constant in the derivation to follow, and as such its removal does not provide significant advantage.

Expanding the first term in equation 2.28 produces:

$$\begin{aligned}&\eta_m \nabla\left[\frac{1}{\varphi}\nabla\cdot[\boldsymbol{V}]\right]-\eta_m\nabla[\nabla\cdot(\boldsymbol{V})]\\&+\eta_m\nabla\cdot[\nabla[\boldsymbol{V}]+(\nabla[\boldsymbol{V}])^T]-\frac{2}{3}\eta_m\nabla\cdot[\nabla\cdot[\boldsymbol{V}]\boldsymbol{I}]\\&+(1-\varphi)\Delta\rho\, g\,\hat{\boldsymbol{k}}+\frac{\eta_f}{k_o\varphi^n}\varphi(\boldsymbol{u}-\boldsymbol{V})=0\end{aligned} \tag{2.29}$$

and then by substituting identity 2.11, equation 2.29 can be rewritten as:

$$\begin{aligned}&\eta_m \nabla\left[\frac{1}{\varphi}\nabla\cdot(\boldsymbol{V})\right]+\eta_m\nabla^2[\boldsymbol{V}]-\frac{2}{3}\eta_m\nabla[\nabla\cdot[\boldsymbol{V}]]\\&+(1-\varphi)\Delta\rho\, g\,\hat{\boldsymbol{k}}+\frac{\eta_f}{k_o\varphi^n}\varphi(\boldsymbol{u}-\boldsymbol{V})=0\end{aligned} \tag{2.30}$$

Regrouping terms 1 and 3 from equation 2.30 and multiplying by a factor $\varphi^n/\eta_m$ in preparation for the divergence operator:

$$\begin{aligned}&\varphi^n\nabla^2[\boldsymbol{V}]+\varphi^n\nabla\left[\left(\frac{1}{\varphi}-\frac{2}{3}\right)\nabla\cdot[\boldsymbol{V}]\right]\\&+\varphi^n(1-\varphi)\Delta\rho\frac{g}{\eta_m}\hat{\boldsymbol{k}}+\frac{\eta_f}{k_o\eta_m}\varphi(\boldsymbol{u}-\boldsymbol{V})=0\end{aligned} \tag{2.31}$$

Taking the divergence of equation 2.31 then gives:

$$\begin{aligned}&\nabla\cdot[\varphi^n\nabla^2[\boldsymbol{V}]]+\nabla\cdot\left[\varphi^n\nabla\left[\left(\frac{1}{\varphi}-\frac{2}{3}\right)\nabla\cdot[\boldsymbol{V}]\right]\right]\\&+\nabla\cdot\left[\varphi^n(1-\varphi)\Delta\rho\frac{g}{\eta_m}\hat{\boldsymbol{k}}\right]+\frac{\eta_f}{k_o\eta_m}\nabla\cdot[\varphi(\boldsymbol{u}-\boldsymbol{V})]=0\end{aligned} \tag{2.32}$$

Now, the last term of this equation can be replaced using the combined conservation of mass equation 2.3 in order to remove the fluid velocity from the equation:

$$\begin{aligned}&\nabla\cdot[\varphi^n\nabla^2[\boldsymbol{V}]]+\nabla\cdot\left[\varphi^n\nabla\left[\left(\frac{1}{\varphi}-\frac{2}{3}\right)\nabla\cdot[\boldsymbol{V}]\right]\right]\\&+\frac{\Delta\rho\, g}{\eta_m}\frac{\partial}{\partial z}[\varphi^n(1-\varphi)]-\frac{\eta_f}{k_o\eta_m}\nabla\cdot[\boldsymbol{V}]=0\end{aligned} \tag{2.33}$$

Following rearranging and use of the chain rule, equation 2.33 becomes:

$$\begin{aligned}&\varphi^n\nabla^2\left[\left(\frac{1}{\varphi}+\frac{1}{3}\right)\nabla\cdot[\boldsymbol{V}]\right]\\&+\nabla[\varphi^n]\cdot\left[\nabla^2[\boldsymbol{V}]+\nabla\left[\left(\frac{1}{\varphi}-\frac{2}{3}\right)\nabla\cdot[\boldsymbol{V}]\right]\right]\\&+\frac{\Delta\rho g}{\eta_m}\frac{\partial}{\partial z}[\varphi^n(1-\varphi)]-\frac{\eta_f}{k_o\eta_m}\nabla\cdot[\boldsymbol{V}]=0\end{aligned}\tag{2.34}$$

Now that most of the $\boldsymbol{V}$ terms appear within a divergence operator it is helpful to substitute in the scalar variable $D = \nabla\cdot\boldsymbol{V}$, which is the Laplacian of the scalar potential $B$ from equation 2.9. Therefore equation 2.34 can be written as:

$$\begin{aligned}&\varphi^n\nabla^2\left[\left(\frac{1}{\varphi}+\frac{1}{3}\right)D\right]+\nabla[\varphi^n]\cdot\left[\nabla^2[\boldsymbol{V}]+\nabla\left[\left(\frac{1}{\varphi}-\frac{2}{3}\right)D\right]\right]\\&+\frac{\Delta\rho g}{\eta_m}\frac{\partial}{\partial z}[\varphi^n(1-\varphi)]-\frac{\eta_f}{k_o\eta_m}D=0\end{aligned}\tag{2.35}$$

To remove the remaining term in $\boldsymbol{V}$ we, first using identity 2.12:

$$\begin{aligned}&\varphi^n\nabla^2\left[\left(\frac{1}{\varphi}+\frac{1}{3}\right)D\right]\\&+\nabla[\varphi^n]\cdot\left[\nabla[\nabla\cdot[\boldsymbol{V}]]-\nabla\times[\nabla\times[\boldsymbol{V}]]+\nabla\left[\left(\frac{1}{\varphi}-\frac{2}{3}\right)D\right]\right]\\&+\frac{\Delta\rho g}{\eta_m}\frac{\partial}{\partial z}[\varphi^n(1-\varphi)]-\frac{\eta_f}{k_o\eta_m}D=0\end{aligned}\tag{2.36}$$

using equation 2.1, noting that the field component based on $B$ is removed by the curl operator and that based on $\boldsymbol{A}$ is removed by the divergence operator, so:

$$\begin{aligned}&\varphi^n\nabla^2\left[\left(\frac{1}{\varphi}+\frac{1}{3}\right)D\right]\\&+\nabla[\varphi^n]\cdot\left[\nabla[D]-\nabla\times[\nabla\times[\nabla\times[\boldsymbol{A}]]]+\nabla\left[\left(\frac{1}{\varphi}-\frac{2}{3}\right)D\right]\right]\\&+\frac{\Delta\rho g}{\eta_m}\frac{\partial}{\partial z}[\varphi^n(1-\varphi)]-\frac{\eta_f}{k_o\eta_m}D=0\end{aligned}\tag{2.37}$$

This equation is now, in principle, solvable for $D$ assuming the melt fraction, $\varphi$, and vector potential, $\boldsymbol{A}$, are known. However an efficient, feasible algorithm requires further rearrangement.

The next few steps are towards the goal of separating the terms out into their respective dependence on the various gradients of $D$. The identity 2.13 can be used to expand the first term in order to separate $D$ from the melt fraction, $\varphi$:

$$\begin{aligned}&\varphi^n\left(\frac{1}{\varphi}+\frac{1}{3}\right)\nabla^2 D+\varphi^n D\nabla^2\left(\frac{1}{\varphi}\right)+2\varphi^n\nabla\left(\frac{1}{\varphi}\right)\cdot\nabla D\\&+\nabla[\varphi^n]\cdot\left[-\nabla\times[\nabla\times[\nabla\times[\boldsymbol{A}]]]+\nabla\left[\left(\frac{1}{\varphi}+\frac{1}{3}\right)D\right]\right]\\&+\frac{\Delta\rho g}{\eta_m}\frac{\partial}{\partial z}[\varphi^n(1-\varphi)]-\frac{\eta_f}{k_o\eta_m}D=0\end{aligned}\tag{2.38}$$

Next, the product rule is used to expand the second line in equation 2.38:

$$\begin{aligned}&\varphi^n\left(\frac{1}{\varphi}+\frac{1}{3}\right)\nabla^2 D+\varphi^n D\nabla^2\left(\frac{1}{\varphi}\right)+2\varphi^n\nabla\left(\frac{1}{\varphi}\right)\cdot\nabla D\\&+\nabla[\varphi^n]\cdot\left[-\nabla\times[\nabla\times[\nabla\times[\boldsymbol{A}]]]+D\nabla\left[\frac{1}{\varphi}\right]+\left(\frac{1}{\varphi}+\frac{1}{3}\right)\nabla[D]\right]\\&+\frac{\Delta\rho g}{\eta_m}\frac{\partial}{\partial z}[\varphi^n(1-\varphi)]-\frac{\eta_f}{k_o\eta_m}D=0\end{aligned}\tag{2.39}$$

Finally, dividing the entirety of equation 2.39 by $\varphi^n$ obtains:

$$\begin{aligned}&\left(\frac{1}{\varphi}+\frac{1}{3}\right)\nabla^2 D+D\nabla^2\left(\frac{1}{\varphi}\right)+2\nabla\left(\frac{1}{\varphi}\right)\cdot\nabla D\\&+\nabla[\ln(\varphi^n)]\cdot\left[-\nabla\times[\nabla\times[\nabla\times[\boldsymbol{A}]]]+D\nabla\left[\frac{1}{\varphi}\right]+\left(\frac{1}{\varphi}+\frac{1}{3}\right)\nabla[D]\right]\\&+\frac{\Delta\rho g}{\eta_m\varphi^n}\frac{\partial}{\partial z}[\varphi^n(1-\varphi)]-\frac{\eta_f}{k_o\eta_m\varphi^n}D=0\end{aligned}\tag{2.40}$$

Collecting terms in $D$, $\nabla D$ and $\nabla^2 D$ produces:

$$\begin{aligned}&\left(\frac{1}{\varphi}+\frac{1}{3}\right)\nabla^2 D\\&+\left(\left(\frac{1}{\varphi}+\frac{1}{3}\right)\nabla[\ln(\varphi^n)]+2\nabla\left(\varphi^{-1}\right)\right)\cdot\nabla[D]\\&+\left(\nabla^2\left(\varphi^{-1}\right)-\frac{\eta_f}{k_o\eta_m\varphi^n}+\nabla[\ln(\varphi^n)]\cdot\nabla\left[\varphi^{-1}\right]\right)D\\&=\nabla[\ln(\varphi^n)]\cdot\nabla\times[\nabla\times[\nabla\times[\boldsymbol{A}]]]-\frac{\Delta\rho g}{\eta_m\varphi^n}\frac{\partial}{\partial z}[\varphi^n(1-\varphi)]\end{aligned}\tag{2.41}$$

Finally, by dividing through by the coefficient of $\nabla^2 D$:

$$\begin{aligned}&\nabla^2 D\\&+\left(\nabla[\ln(\varphi^n)]+\frac{6\varphi}{3+\varphi}\nabla\left(\varphi^{-1}\right)\right)\cdot\nabla[D]\\&+\frac{3\varphi}{3+\varphi}\left(\nabla^2\left(\varphi^{-1}\right)-\frac{\eta_f}{k_o\eta_m\varphi^n}+\nabla[\ln(\varphi^n)]\cdot\nabla\left[\varphi^{-1}\right]\right)D\\&=\frac{3\varphi}{3+\varphi}\left[\nabla[\ln(\varphi^n)]\cdot\nabla\times[\nabla\times[\nabla\times[\boldsymbol{A}]]]-\frac{\Delta\rho g}{\eta_m\varphi^n}\frac{\partial}{\partial z}[\varphi^n(1-\varphi)]\right]\end{aligned} \tag{2.42}$$

Equation 2.42 is similar to that derived by Spiegelman (1993a) but with several key differences. My derivation does not contain a bulk viscosity constant and shows several extra functions of the melt fraction. Spiegelman (1993a) does not go into as much detail on the derivation of the equations used and shown as I do, so the reasons for the differences are difficult to pin down, the most likely sources of difference being that Spiegelman does not separate $k_\varphi$ into $k_0\varphi^n$ and uses the small melt fraction approximation to a greater degree.

This reordering means that the above equation 2.42 can now be expressed in the form of a second-order three-dimensional inhomogeneous partial differential equation:

$$\nabla^2 D+\boldsymbol{r}\cdot\nabla D-q^2 D=p \tag{2.43}$$

where:

$$q^2=\frac{3\varphi}{(3+\varphi)}\left[\frac{\eta_f}{\eta_m k_0\varphi^n}-\nabla^2\varphi^{-1}-\nabla\left(\ln\varphi^n\right)\cdot\nabla\left(\frac{1}{\varphi}\right)\right] \tag{2.44}$$

$$p=-\frac{3\varphi}{(3+\varphi)}\left[\frac{\Delta\rho g}{\eta_m\varphi^n}\frac{\partial}{\partial z}\left[\varphi^n(1-\varphi)\right]-\nabla\left(\ln\varphi^n\right)\cdot\left[\nabla\times[\nabla\times[\nabla\times[\boldsymbol{A_m}]]]\right]\right] \tag{2.45}$$

$$\boldsymbol{r}=\left[\nabla\left(\ln\varphi^n\right)+\frac{6\varphi}{3+\varphi}\nabla\varphi^{-1}\right] \tag{2.46}$$

In chapters 3 and 4 I discuss different numerical algorithms, that can be applied to solve equation 2.43 for *D*. Given a value for *D*, equation 2.9 can be inverted to obtain *B* and thus find the velocity of the matrix using equation 2.1 using $\boldsymbol{A}$ and *B*.

### 2.3.3 Application of conservation of mass to the derivation of time dependence.

In the previous section, I used conservation of momentum to derive equations that describe the spatial variation of the matrix velocity field based on a known melt fraction distribution of φ. I now apply conservation of mass to obtain an equation that describes how the melt fraction evolves with time based on a known velocity field ***V***.

Starting with the conservation of matrix mass (equation 2.2) and expanding the divergence operator to get:

$$\frac{\partial \varphi}{\partial t} = (1-\varphi)\nabla\cdot[\boldsymbol{V}] - \boldsymbol{V}\cdot\nabla[\varphi] \tag{2.47}$$

The terms in ***V*** can be replaced using the divergence *D* (equation 2.9) and the vector and scalar potentials ***A*** and *B* (equation 2.1):

$$\frac{\partial \varphi}{\partial t} = (1-\varphi)D - [\nabla\times\boldsymbol{A} + \nabla B]\cdot\nabla[\varphi] \tag{2.48}$$

With equations 2.9, 2.24, 2.43 and 2.48, I now have a complete system that is in principle solvable using numerical methods, given appropriate boundary and initial conditions. Equation 2.48 is used as a time step function by most authors, such as Spiegelman (1993a), Bercovici et al. (2001a) and Ŝrámek et al. (2007), although in this case I am ignoring the melting term.

In chapter 3 I describe the one-dimensional implementation of algorithms based on these equations and in chapter 4 I discuss the three-dimensional implementation.

## *2.4 Discussion of simplifying assumptions*

In the formulation of equations 2.24 and 2.43, I have made several assumptions that should be explained and analysed in more detail.

In general, these assumptions allow a feasible numerical algorithm to be implemented while retaining the essential physical processes which I wish to study.

### 2.4.1 Small melt fraction approximation

The small melt fraction approximation has been used by authors such as Hewitt and Fowler (2008) in derivation of equation 2.15 and in other equations by Spiegelman (1993a) and Barcilon and Richter (1986). In my formulation I applied this approximation once in derivation of equation 2.17 and twice in deriving equation 2.27, reproduced here:

$$\begin{aligned}&\nabla\left[(1-\varphi)\frac{\eta_m}{\varphi}\nabla\cdot[(1-\varphi)\boldsymbol{V}]\right]\\&+\eta_m\nabla\cdot\left[(1-\varphi)\left(\nabla[\vec{\boldsymbol{V}}]+(\nabla[\vec{\boldsymbol{V}}])^T-\frac{2}{3}\nabla\cdot[\boldsymbol{V}]\boldsymbol{I}\right)\right]\\&+(1-\varphi)\Delta\rho g\hat{\boldsymbol{k}}+\frac{\eta_f}{k_o\varphi^n}\varphi(\boldsymbol{u}-\boldsymbol{V})=0\end{aligned}\tag{2.27}$$

If φ << 1 it is expected that:

$$(1-\varphi)\boldsymbol{V}\approx\boldsymbol{V}\tag{2.49}$$

however:

$$\nabla\cdot((1-\varphi)\boldsymbol{V})=\nabla[\boldsymbol{V}]-\varphi\nabla[\boldsymbol{V}]-\boldsymbol{V}\cdot\nabla[\varphi]\tag{2.50}$$

Clearly, if φ << 1, the second term must be small relative to the first term. For the third term to also be small, requires another constraint on the melt fraction distribution:

$$|\nabla[\varphi]|\ll\frac{|\nabla\cdot\boldsymbol{V}|}{|\vec{\boldsymbol{V}}|}\approx|\nabla\ln|\boldsymbol{V}||\tag{2.51}$$

thus, the approximation:

$$\nabla\cdot[(1-\varphi)\boldsymbol{V}]\approx\nabla[\boldsymbol{V}]\tag{2.52}$$

Equation 2.52 is only valid if gradients of the melt fraction are sufficiently small. The melt fraction must be not only small, but smoothly varying. As such, sharp discontinuities in φ may invalidate this formulation. Accepting this constraint 1 – φ ≈ 1 is used in both of the terms that are subject to a divergence operator. The (1 – φ) term however should be retained in the buoyancy term at least:

$$\begin{aligned}&\nabla\left[(1-\varphi)\frac{\eta_m}{\varphi}\nabla\cdot[\boldsymbol{V}]\right]\\&+\eta_m\nabla\cdot\left[\left(\nabla[\boldsymbol{V}]+(\nabla[\vec{\boldsymbol{V}}])^T-\frac{2}{3}\nabla\cdot[\boldsymbol{V}]\boldsymbol{I}\right)\right]\\&+(1-\varphi)\Delta\rho g\hat{\boldsymbol{k}}+\frac{\eta_f}{k_o\varphi^n}\varphi(\boldsymbol{u}-\boldsymbol{V})=0\end{aligned}\tag{2.28}$$

The $1 - \varphi \approx 1$ approximation limits the distribution of melt fraction that can be accurately modelled and results in the solutions being correct only if the background melt fraction and the melt fraction gradient remains small. However, within this restriction many interesting problems can still be studied.
Barcilon and Richter (1986) explored the validity of this approximation, showing that for peaks in the melt fraction below ~30% there is around an error of only ~1% in the one-dimensional numerical solution relative to the corresponding analytical solution. Spiegelman (1993b) also investigated the problem and showed that the amplitude and phase velocity of solitary waves are resolved to within 0.1% and 0.2% of their analytical counterparts respectively. Therefore, I conclude that using this approximation is sufficiently accurate for the test cases that I describe.

### 2.4.2 Constant viscosity

To simplify the governing equations, I assumed in the derivation that viscosities of both matrix and fluid are constant with respect to both depth and time. This assumption is also frequently used in the literature in the derivation of the equation for $\boldsymbol{V}$ (or equivalently $\boldsymbol{A}$ and $B$). In the preceding derivations (sections 2.3.1 to 2.3.3), viscosity is assumed spatially constant in the derivation of 2.18 from 2.17, and again in the derivation of 2.27 from 2.26.

I thus ignore measurements which show that viscosities of both matrix and melt are dependent on depth, temperature and composition.

The effects of viscosity variation on melt extraction from a deformable permeable medium are explored by Richardson (1998), who showed that solitary waves can become very narrow and peaked if the viscosity is a strong function of melt fraction, and that dykes can form under high external stresses. Kohlstedt and Zimmerman, (1996) also show that viscosity is reduced by up to a factor of 20 as melt fraction varies from 0 to 10%. This viscosity may be highly variable in partially molten rock, but before including that complication in an analysis there is much value in studying the behaviour of a simplified constant viscosity system.

### 2.4.3 Constant density

Densities of melt and matrix are assumed constant for similar reasons. This approximation was used in the formulation of both the conservation of matrix mass (equation 2.2) and the combined mass conservation (equation 2.3) and also when the curl and divergence operations were applied when deriving the $\boldsymbol{A}$ and $D$ equations (2.24 and 2.43).

Although density may vary significantly with depth in the upper mantle as defined by the PREM model (Dziewonski and Anderson, 1981) the depth range of interest in this study is between about 30 to 90 km (between the brittle-ductile transition and the onset of partial melting) within which density changes from 3380kgm$^{-3}$ to 3373kgm$^{-3}$ for the matrix and 2746kgm$^{-3}$ to 2824kgm$^{-3}$ for the melt based on PREM and experimental data by Ohtani and Maeda, (2001).

Variation of density due to compressibility is not significant in this problem if both matrix and melt have the same compressibility. The principle driving force is provided by the density difference between melt and matrix, which is estimated at between 634kgm$^{-3}$ and 549kgm$^{-3}$. Thus variations in $\Delta\rho$ are thought to be in the range of 10 to 20% of the constant value used with this assumption. The impact of such variation is small relative to possible changes in viscosity and is neglected here in order to avoid unnecessary complexity that would not change the physical process in a significant way.

### 2.4.4 Deviatoric shear is zero for fluid phase

The assumption that the fluid phase does not support any deviatoric shear stress is based on the assumption of a large contrast in viscosity between fluid and matrix and the idea that stress in the fluid phase is isotropic.

I use this approximation in the momentum conservation equation (equation 2.4). The melt does not support significant deviatoric stress because of its low viscosity. For molten basalt at a temperature of 1300°C to 1120°C, the viscosity is about 10Pas from experiments by Shaw (1969), which is many orders of magnitude less than typical mantle viscosity of around $10^{18}$Pas (Šrámek et al., 2007).

The assumption that deviatoric stress is zero for the fluid phase is commonly used in the literature, e.g. (Šrámek et al., 2007; Hewitt and Fowler, 2008; and Spieglman, 1993a).

### 2.4.5 No phase change

The final simplifying assumption made is that no melting or freezing occurs in the medium; terms that represent melting or freezing are set to zero in the mass conservation equations 2.2 and 2.3. I assume that a fixed volume of partial melt exists at the beginning of an experiment in the form of the melt fraction distribution that is used as the initial condition. Since I am also assuming that no freezing takes place, this removes the possibility of melt focusing caused by the constriction of melt channels discussed by Hewitt and Fowler (2008).

The effects of phase change could be readily included in the aforementioned formulation but I focus here on the transport of melt concentrations that move quickly enough to avoid significant melting or freezing.

## *2.5 Non-dimensionalisation*

Non-dimensionalisation simplifies and enhances the utility of mathematical solutions. In doing so the mathematical problem is generalised as to highlight the length, time and stress scales inherent to the physical problem.
In equations 2.24 and 2.42, two groups of constants stand out:

$$\frac{\eta_f}{\eta_m k_0} \text{ with units } [m]^{-2} \text{ and } \frac{\Delta\rho g}{\eta_m} \text{ with units } [s]^{-1}[m]^{-1} \tag{2.53}$$

The first group suggests a scaling length for non-dimensionalising distance:

$$\delta = \sqrt{\frac{k_0 \eta_m}{\eta_f}} \tag{2.54}$$

This length scale arises is an important factor in two-phase fluid systems. Solution of a compacting layer with uniform melt fraction by McKenzie (1984) determines this as the length scale above which the upward percolation of melt supports the weight of the matrix. However the “compaction length” as stated by McKenzie (1984) is a function of melt fraction, using the term $k_\varphi$ instead of $k_0$. Therefore, I shall refer to equation 2.54 as the “melt fraction independent compaction length”, to avoid confusion.

My solution assumes a finite layer so a second constant is also needed:

$$z' = \frac{z}{h} \quad \text{where} \quad h = \delta h_o \tag{2.55}$$

where $h$ is the layer thickness and $h_0$ is a non-dimensional value that defines the layer thickness in terms of the melt fraction independent compaction length. $z'$ is the non-dimensional depth. The second group in 2.53 can now be used in conjunction with $h$ to define a velocity scale $V_0$:

$$V' = \frac{V}{V_0} \quad \text{where} \quad V_0 = \frac{\Delta \rho g}{\eta_m} h^2 \tag{2.56}$$

where $V'$ is the non-dimensional velocity.

These two constants, $h$ and $V_0$, can then be used together to non-dimensionalise time, divergence and vector potentials in a consistent way:

$$t' = \frac{V_0}{h} t \tag{2.57}$$

$$D' = \frac{h}{V_0} D \tag{2.58}$$

$$\boldsymbol{A}' = \frac{1}{h V_0} \boldsymbol{A} \tag{2.59}$$

### 2.5.1 Non-dimensionalisation of the *A* equation

Taking equation 2.24 and applying the non-dimensionalisation equations 2.55 and 2.59 produces:

$$\nabla^4 [\boldsymbol{A}'] h \frac{V_0}{h^4} = - \frac{\Delta \rho g}{\eta_m} \nabla \times [\varphi \hat{\boldsymbol{k}}] \frac{1}{h} \tag{2.60}$$

The constants cancel out completely to fully non-dimensionalise equation 2.60:

$$\nabla^4 [\boldsymbol{A}'] = - \nabla \times [\varphi \hat{\boldsymbol{k}}] \tag{2.61}$$

### 2.5.2 Non-dimensionalisation of the *D* equation

For the *D* equation (equation 2.42), the non-dimensional constants 2.55, 2.58 and 2.59 are used. The equation for $q^2$ (equation 2.44) becomes:

$$q'^2 = \frac{3\phi}{(3+\phi)}\left[\frac{h_0^2}{\varphi^n} - \nabla^2\varphi^{-1} - \nabla\left(\ln\varphi^n\right)\cdot\nabla\left(\varphi^{-1}\right)\right] \tag{2.62}$$

Equation 2.46 for $\boldsymbol{r}$ is:

$$\boldsymbol{r}' = \left[\nabla\left(\ln\phi^n\right) + \frac{6\phi}{3+\phi}\nabla\phi^{-1}\right] \tag{2.63}$$

*p* (equation 2.45) becomes:

$$p' = \frac{3\phi}{3+\phi}\left[\nabla\left(\ln\phi^n\right)\cdot\nabla\times[\nabla\times[\nabla\times[\boldsymbol{A}']]] - \frac{1}{\phi^n}\frac{\partial}{\partial z}\left[\phi^n(1-\phi)\right]\right] \tag{2.64}$$

The equation for *D* therefore remains the same, except for prime notation:

$$\nabla^2 D' + \boldsymbol{r}'\cdot\nabla D' - q'^2 D' = p' \tag{2.65}$$

### 2.5.3 Non-dimensionalisation of the time step equation

The final equation that needs to be non-dimensionalised is equation 2.48, using equations 2.55 and 2.58 to 2.60:

$$\frac{\partial\varphi}{\partial t'} = (1-\varphi)D' - [\nabla\times\boldsymbol{A}' + \nabla B']\cdot\nabla[\varphi] \tag{2.66}$$

These non-dimensional formula (equations 2.43, 2.61 to 2.64, and 2.66) provide the basis for all numerical modelling discussed in this thesis.

## 2.6 Discretisation

Discretisation is the representation of a continuous function by a discrete set of values that span the relevant domain. It is a vital step in the creation of any potentially numerically solvable set of equations to enable numerical solution.

To discretise a continuous function, a separation between points needs to be defined. For a one-dimensional system this requires just one separation such as $\Delta z$ while a three-dimensional system requires three, $\Delta x$, $\Delta y$ and $\Delta z$. This allows the splitting of any three-dimensional function into a series of discretised values that define an approximation of the analogue function.

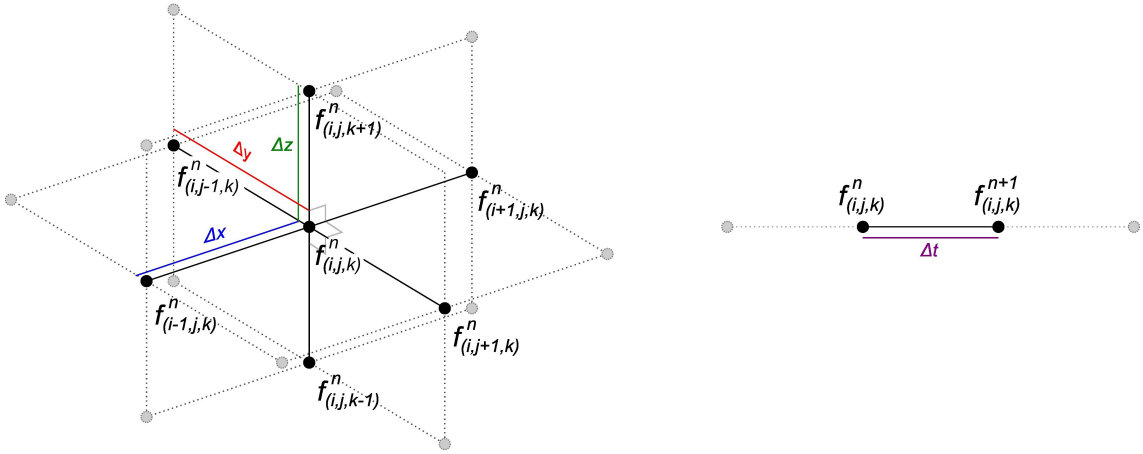


*Figure 10: Distribution of the finite difference mesh in three-dimensional space (i,j,k) and time (n).*

The smaller the choice of $\Delta x$, $\Delta y$ and $\Delta z$, the more accurate the function is in capturing short wavelength components, but the more costly in computer time it is to numerically model, as small spacing conversely requires more data points for any finite field. The reduction in accuracy with increasing discretisation length is represented in Figure 11.

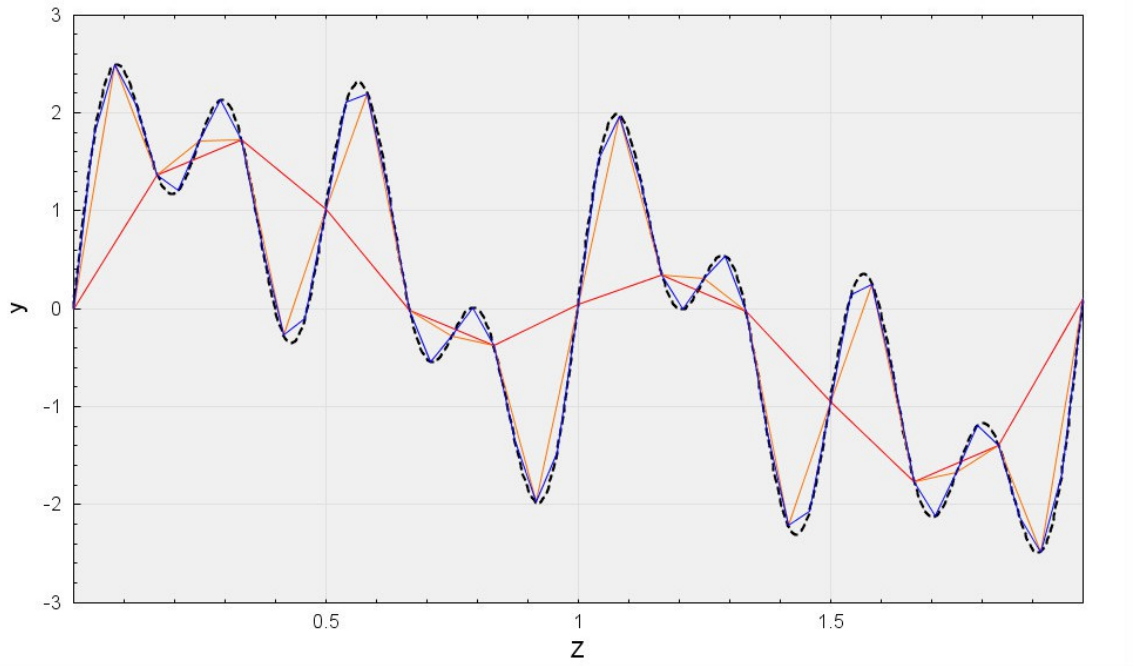


*Figure 11: An example of truncation errors due to discretisation of a simple function. The dashed black line has 1000 points and is a very good representation of the analogue function used, y=sin(z)+sin(2πz)+sin(4πz)+sin(8πz). The red line uses 12 points, the orange line uses 24, and the blue line 48. Increasing the number of points gives a discrete solution that more accurately represents the analogue data. The higher harmonics are of much shorter length scale and are simply lost in discretisation with a larger Δz, termed aliasing.*

Derivatives are approximated with finite difference techniques when using vector calculus in a discrete regime. The main finite difference formula for a first and second order partial differential are:

**Centred Difference**

$$\frac{\partial f}{\partial z} = \frac{f_{(i,j,k+1)} - f_{(i,j,k-1)}}{2\Delta z} \tag{2.67}$$

$$\frac{\partial^2 f}{\partial z^2} = \frac{f_{(i,j,k+1)} - 2\mathrm{f}_{(i,j,k)} + f_{(i,j,k-1)}}{\Delta z^2} \tag{2.68}$$

**Boundary Difference**

$$\frac{\partial f}{\partial z} = \frac{f_{(i,j,k+1)} - f_{(i,j,k)}}{\Delta z} \tag{2.69}$$

$$\frac{\partial f}{\partial z} = \frac{f_{(i,j,k)} - f_{(i,j,k-1)}}{\Delta z} \tag{2.70}$$

The boundary representations of the first order derivatives in 2.69 and 2.70 are first order (and therefore should be avoided if possible). There is however a second problem with the boundary difference methods as they do not calculate the gradient at the $f_{(i,j,k)}$ point, but the gradient at $k+1/2$, assigning this gradient to point $k$. This error ban be reduced by increasing the accuracy of the boundary difference equation through inclusion of extra points using a Taylor series expansion.

As expressed in appendix A (7.1), an $O(\Delta z^2)$ accurate boundary difference can be derived, resulting in:

**Boundary Difference**

$$\frac{\partial f}{\partial z} = -\frac{\left(3f_{(i,j,k)} - 4f_{(i,j,k+1)} + f_{(i,j,k+2)}\right)}{2\Delta z} + O\left(\Delta z^2\right) \tag{2.71}$$

$$\frac{\partial f}{\partial z} = \frac{\left(3f_{(i,j,k)} - 4f_{(i,j,k-1)} + f_{(i,j,k-2)}\right)}{2\Delta z} + O\left(\Delta z^2\right) \tag{2.72}$$

These finite difference equations allow the calculation of the boundary gradients used in the numerical models discussed in this thesis when boundary conditions are not sufficient.

# 3 One-Dimensional Numerical Model

## *3.1 Introduction*

The first step in my investigation into the physics of a two-phase fluid medium examines the behaviour of a one-dimensional model, based on the equations derived in chapter 2. The intention of this step is to gain a better understanding of how the equations work together, the physical processes they describe and of problems that may arise in the numerical methods when I later move on to the three-dimensional problem.

One-dimensional models are common in the literature as they provide a reasonable insight into how the physical system behaves while requiring far less processor time than two- or three-dimensional model. Three-dimensional numerical solutions by Wiggins and Spiegelman (1995) showed that a one-dimensional solitary wave in a three-dimensional model is unstable and will break up into a series of spherical three-dimensional solitary waves. Comparable waves in a one-dimensional model however exhibit many of the same characteristics as the three-dimensional waves, so they are a valid target for a preliminary investigation.

With this numerical model I first examine the compaction problem in an initially homogeneous two-phase medium, comparing my numerical solutions against an analytical solution obtained by McKenzie (1984). I then study solitary waves in the compacting medium and compare their properties to those predicted by other authors. I examine the generation and interaction of these solitary waves from a range of initial conditions in an attempt to provide an improved description and new insights into melt extraction.

## *3.2 Mathematical Framework*

### 3.2.1 Conversion of equations to one-dimension

Although I have derived a set of mathematical equations that can be solved numerically, they can be simplified for a one-dimensional setting. Allowing only variations in the z-direction, equation 2.30 is simplified to its one-dimensional form:

$$\left(\frac{3+\varphi}{3\varphi}\right)\frac{\partial^2 V}{\partial z^2}+\frac{\partial V}{\partial z}\frac{\partial}{\partial z}\left[\varphi^{-1}\right] + (1-\varphi)\Delta\rho\frac{g}{\eta_m}+\frac{\eta_f}{k_o\eta_m\varphi^n}\varphi(u-V)=0 \tag{3.1}$$

The one-dimensional form of the combined mass conservation equation (equation 2.3) is:

$$\frac{\partial}{\partial z}[V]+\frac{\partial}{\partial z}[\varphi(u-V)]=0 \tag{3.2}$$

Integrating equation 3.2 and setting the integration constant to zero since $V$=0 when $\varphi$=0:

$$-V=\varphi(u-V) \tag{3.3}$$

followed by substituting equation 3.3 into equation 3.1 to obtain:

$$\left(\frac{3+\varphi}{3\varphi}\right)\frac{\partial^2 V}{\partial z^2}+\frac{\partial}{\partial z}\left[\varphi^{-1}\right]\frac{\partial V}{\partial z}-\frac{\eta_f}{k_o\eta_m\varphi^n}V=-(1-\varphi)\Delta\rho\frac{g}{\eta_m} \tag{3.4}$$

I can integrate equation 3.4 numerically for a known distribution of the melt fraction $\varphi$, subject to appropriate boundary conditions on $V$. In section 3.2.4 below I describe a numerical implementation based on using a tridiagonal solver. As the solution evolves, the melt fraction distribution is constrained by equation 2.2, whose one-dimensional form is:

$$\frac{\partial\varphi}{\partial t}=(1-\varphi)\frac{\partial V}{\partial z}-V\frac{\partial\varphi}{\partial z} \tag{3.5}$$

The one-dimensional form of the problem requires that the Helmholtz decomposition (equation 2.1) of the velocity field has zero curl ($\boldsymbol{A}$=0).

The one-dimensional form of 2.1 is therefore:

$$V = \frac{\partial B}{\partial z} \tag{3.6}$$

It remains useful however to refer to the divergence of the matrix velocity field:

$$D = \frac{\partial^2 B}{\partial z^2} \tag{3.7}$$

I now consider relevant boundary conditions and describe a practical method of solving equations 3.4 and 3.5 for the functions $V(z,t)$ and $\varphi(z,t)$.

### 3.2.2 Boundary conditions

Boundary conditions are a necessary component of any integration problem; they determine the function values on the boundaries of the modelled region. In term 3.4 they represent on essential input, as in convection models, where heat influx through a basal boundary and out through the upper boundary drives an internal circulation, the choice of boundary conditions can inhibit or enable compaction. Equation 3.4 requires two boundary conditions on $V$ because the leading term is a second-order derivative with respect to $z$. I assume a Dirichlet boundary condition on the basal edge of the modelled region, which can be expressed as:

$$V_{z=0} = 0 \tag{3.8}$$

The Dirichlet boundary condition in this case represents an impermeable boundary through which no material passes. On the upper ($z=h$) boundary I use a Neumann boundary condition:

$$\frac{\partial V}{\partial z}\Big|_{z=h} = 0 \tag{3.9}$$

The Neumann boundary condition is sometimes referred to as a stress-free boundary condition, as it indicates there is no vertical velocity gradient on the boundary, implying that a static stress acts on the boundary. Fluid and matrix however can flow in and out of this boundary, allowing for compaction of the medium beneath. In physical terms a low density melt can exit the volume on this type of boundary to form a magma chamber.

These boundary and initial conditions are in common use throughout the literature on this subject (e.g. McKenzie, 1984).

### 3.2.3 Initial conditions

Different configurations of the melt fraction field drive the system to evolve along different paths, and several of these paths are of interest in my study. Spiegelman (1993b) discusses the initiation of solitary waves in a one-dimensional system, showing that one way to initiate solitary waves is by a restriction in vertical melt flow.

I first consider the problem of a uniform initial melt fraction of magnitude $\varphi_0$, which has to be relatively small for the solution to be accurate, due to the small melt fraction assumption discussed in section 2.4.1. Although 0.1% seems like a low value it is sufficient for full interconnectivity of the melt network. As demonstrated by Zhu and Hirth (2003) 0.02% is enough to ensure melt connectivity. A melt fraction distribution of this configuration does not develop solitary waves as there is no initial gradient in melt fraction. It does however allow me to do a comparison of my numerical solutions and an analytical solution by McKenzie (1984). This comparison confirms the accuracy of my computational methods and provides insight into the evolution of the system without solitary waves.

Among possible initial conditions used by other authors to produce propagating solitary waves, the sharp gradient function (Spiegelman, 1993a,b) evolves into a long regular chain of solitary waves, as does a band of melting at the base of the layer (Scott and Stevenson, 1984). Barcilon and Richter (1986) used a Gaussian distribution on top of a uniform background melt fraction ($\varphi_0$) to produce stably propagating solitary waves while Richter and McKenzie (1984) used a sech (hyperbolic secant) function to produce a solitary wave train. With this in mind, I have investigated wave trains generated from an initial melt fraction condition defined by the following equation:

$$\varphi_{(z,t=0)} = A\, e^{\frac{(b-z)^2}{(2\sigma)^2}} + \varphi_0 \qquad (3.10)$$

where $A$ is the amplitude of the Gaussian peak, $\sigma$ is the width parameter of the Gaussian, $b$ is the centre location of the peak and $\varphi_0$ is the background melt fraction.

I have chosen this initial distribution as I am investigating singular or small trains of solitary waves in the one-dimensional model, whereas discontinuous initial melt fraction distributions produce close packed trains of solitary waves.

In implementing this equation into my program, 1D2PF, I included the option of adding a second Gaussian perturbation to the background melt fraction, to study the interaction of solitary waves.

### 3.2.4 Tridiagonal algorithm

To solve equation 3.4, I use a tridiagonal matrix solver. In this section, I describe the mathematical and programming aspects of this problem, specifically for the one-dimensional formulation. The second-order ordinary differential equations may be written in the form:

$$a f''(z)+b f'(z)+c f(z)=\Omega(z) \tag{3.11}$$

where:

$$\begin{aligned} a&=\frac{3+\varphi}{3\varphi} \\ b&=\frac{\partial}{\partial z}\varphi^{-1} \\ c&=-\frac{\eta_f}{k_0\eta_m\varphi^n} \\ \Omega&=-(1-\varphi)\frac{\Delta\rho g}{\eta_m} \end{aligned} \tag{3.12}$$

To discretise equation 3.11, I define a series of points with a set separation of $\Delta z$ and use the centred finite difference approximation (equations 2.67) to give a series of linear equations for the discretised value of $f$. This produces:

$$a_k\frac{f_{k-1}-2f_k+f_{k+1}}{\Delta z^2}+b_k\frac{f_{k+1}-f_{k-1}}{2\Delta z}+c_k f_k=\Omega_k \tag{3.13}$$

where $k$ is the grid-point number of the finite difference mesh ($k$=0,$h$). Equation 3.13 can be rearranged to obtain:

$$\left(\frac{a_k}{\Delta z^2}-\frac{b_k}{2\Delta z}\right)f_{k-1}+\left(c_k-\frac{2a_k}{\Delta z^2}\right)f_k+\left(\frac{a_k}{\Delta z^2}+\frac{b_k}{2\Delta z}\right)f_{k+1}=\Omega_k \tag{3.14}$$

In this form, equation 3.14 can be expressed as a matrix equation for the set of $h$ unknowns $\{f_0, f_1,....f_h\}$:

$$\begin{bmatrix} \beta_0 & \gamma_0 & 0 & 0 & \cdots & 0 \\ \alpha_1 & \beta_1 & \gamma_1 & 0 & \cdots & 0 \\ 0 & \alpha_2 & \beta_2 & \gamma_2 & \cdots & 0 \\ \vdots & \ddots & \ddots & \ddots & \ddots & \vdots \\ 0 & \cdots & \alpha_{h-2} & \beta_{h-2} & \gamma_{h-2} & 0 \\ 0 & \cdots & 0 & \alpha_{h-1} & \beta_{h-1} & \gamma_{h-1} \\ 0 & \cdots & 0 & 0 & \alpha_h & \beta_h \end{bmatrix} \begin{bmatrix} f_0 \\ f_1 \\ f_2 \\ \vdots \\ f_{h-2} \\ f_{h-1} \\ f_h \end{bmatrix} = \begin{bmatrix} \Omega_0 \\ \Omega_1 \\ \Omega_2 \\ \vdots \\ \Omega_{h-2} \\ \Omega_{h-1} \\ \Omega_h \end{bmatrix} \tag{3.15}$$

where the α, β and γ terms, in general, are:

$$\alpha_k = \left(\frac{a_k}{\Delta z^2} - \frac{b_k}{2\Delta z}\right) \quad , \quad \beta_k = \left(c_k - \frac{2a_k}{\Delta z^2}\right) \quad , \quad \gamma_k = \left(\frac{a_k}{\Delta z^2} + \frac{b_k}{2\Delta z}\right) \tag{3.16}$$

The first and last equations in 3.15 are not valid however, as they involve values of the function outside of the computational domain. I therefore replace them using the boundary conditions described in the previous section. For the Dirichlet condition on the lower boundary ($k$=$h$):

$$f_h = 0 \tag{3.17}$$

I preserve the structure of the matrix equation 3.15 by defining:

$$\alpha_h = 0, \quad \beta_h = 1, \quad \Omega_h = 0, \tag{3.18}$$

For the Neumann conditions on the upper boundary ($k$=0) the application of the boundary condition requires, from the first order finite difference equation in 2.67:

$$f_1 = f_{-1} \tag{3.19}$$

Again, I preserve the structure of the matrix equation by replacing:

$$\gamma_0 \quad \text{with} \quad \gamma_0 + \alpha_0 = 2\gamma_0 \tag{3.20}$$

Thus, the discretised version of equation 3.4 with the appropriate boundary conditions is written:

$$\begin{bmatrix} \beta_0 & 2\gamma_0 & 0 & 0 & \cdots & 0 \\ \alpha_1 & \beta_1 & \gamma_1 & 0 & \cdots & 0 \\ 0 & \alpha_2 & \beta_2 & \gamma_2 & \cdots & 0 \\ \vdots & \ddots & \ddots & \ddots & \ddots & \vdots \\ 0 & \cdots & \alpha_{h-2} & \beta_{h-2} & \gamma_{h-2} & 0 \\ 0 & \cdots & 0 & \alpha_{h-1} & \beta_{h-1} & \gamma_{h-1} \\ 0 & \cdots & 0 & 0 & 0 & 1 \end{bmatrix} \begin{bmatrix} f_0 \\ f_1 \\ f_2 \\ \vdots \\ f_{h-2} \\ f_{h-1} \\ f_h \end{bmatrix} = \begin{bmatrix} \Omega_0 \\ \Omega_1 \\ \Omega_2 \\ \vdots \\ \Omega_{n-2} \\ \Omega_{n-1} \\ 0 \end{bmatrix} \tag{3.21}$$

Equation 3.21 is solved by forwards and then backwards substitution using the tridiagonal matrix algorithm (TDMA). By subtracting a scaled version of line 1 from line 2, $f_0$ is removed from line 2; the procedure is repeated using lines 2 and 3 to eliminate the coefficient of $f_1$ on line 3; and so on until the coefficient of $f_{n-1}$ has been eliminated on line $h$ and thus obtain the value of $f_h$. In the backward substitution stage the algorithm then works back up the lines of the matrix equation, sequentially solving for $f_{h-1}$, $f_{h-2}$ …. $f_0$. I used the FORTRAN95 subroutine TDMA of Press et al. (1986, p43) to solve the tridiagonal matrix equation 3.21.

### 3.2.5 Solitary wave analysis

In order to better analyse the solitary waves that develop in the numerical solution I implemented an automated detection and measurement algorithm. The way I searched for a peaks was to analyse the gradient of the melt fraction φ. If there is a peak, the gradient of melt fraction will appear as zero in an analytical solution. However, due to discretisation of the function the gradient at the peak of a symmetrical wave may not be exactly zero as the peak point may not be included in the discretisation. I therefore search for a change in gradients of φ from positive to negative using the centred difference gradient of φ at every point in the domain $k{:}0 \rightarrow h$, using $2\Delta z$, $4\Delta z$, $6\Delta z$ and $8\Delta z$ sample separation as depicted by Figure 12. The use of multiple gradients over increasing widths (2 to $8\Delta z$) prevents picking of slight variations in the background melt fraction as solitary waves.

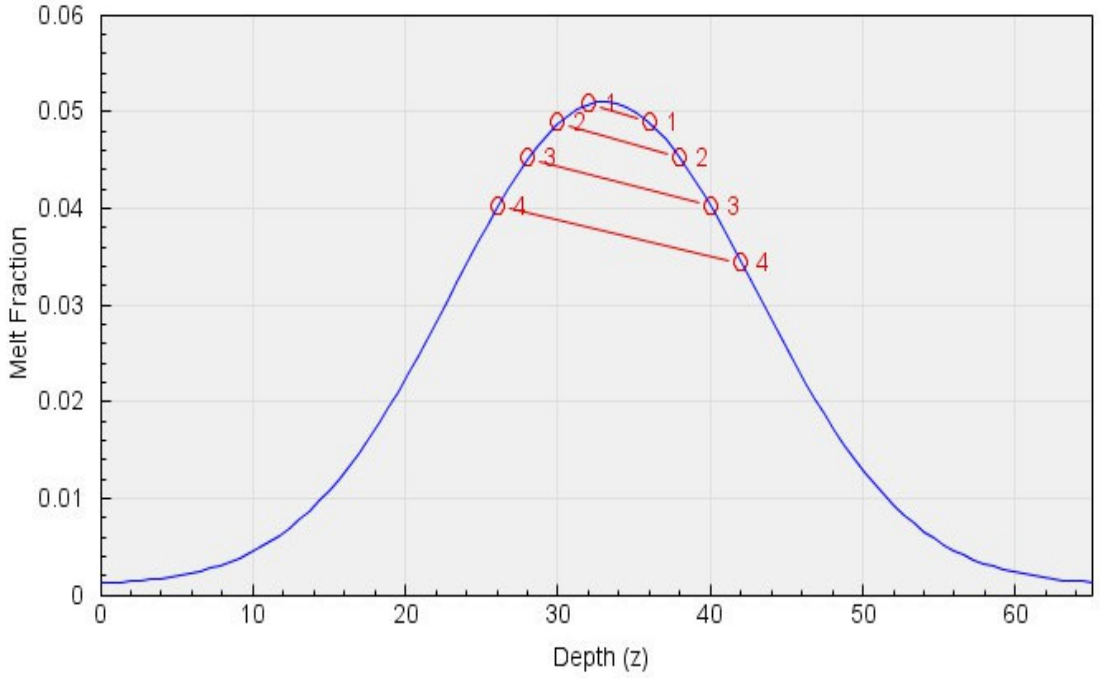


*Figure 12: Diagram of the peak finding algorithm picking method. The red circles are the points used for calculation of the gradient of the blue line. The gradient calculated relates to the point centred between the red points, the same centre point for each set. As the centre point passes over a large peak, the gradient of each red line with turn from positive to negative; at that point the central coordinate defines the point that immediately follows the top of the peak. The blue line is a Gaussian distribution generated by equation 3.10 using σ=7, A=0.05, b=33 $\varphi_0$=0.001.*

To characterize the properties of a solitary wave, I make use of a Gaussian function which fits φ in the vicinity of the peak melt fraction:

$$\varphi_{(z)} = A\, e^{-\frac{(b-z)^2}{2\sigma^2}} + \varphi_0 \tag{3.22}$$

The amplitude (*A*) and centre location (*b*) of equation 3.22 are obtained directly from the detection algorithm, subject to accuracy limited by the discretisation. The width constant (*σ)* is obtained by finding the distance between the two points either side of the peak that correspond to half of the maximum amplitude. This is termed the full width at half maximum, λ or FWHM, and for a Gaussian curve this provides an approximate value for σ:

$$\sigma = \frac{\lambda}{2\sqrt{2\ln 2}} \tag{3.23}$$

The value of σ thus obtained can be used as an input value for an optimisation procedure which iteratively finds the best match for σ by minimising the root mean

squared difference between the Gaussian estimation of the solitary wave and the numerical solution over the depth range given by $b - \lambda/2 < z < b + \lambda/2$.

To estimate the phase speed of the solitary wave, I calculate the position of the solitary wave at regular intervals during a calculation and thus obtain the gradient of the depth time curve. The most stable estimate of the phase speed is obtained when the solitary wave is within a few widths of the top of the solution domain.

### 3.2.6 Program flowchart

To construct this numerical model I decided to use the programming language FORTRAN95 over other options such as C/C++ and Matlab. I chose FORTRAN because the next stage of research was to move onto modification of an existing program called TDCON (Houseman, 1990) which is a three-dimensional parallel mantle convection model, written in FORTRAN77.

To summarise how the program works, I have produced the following flowchart that shows the sequence of computation:

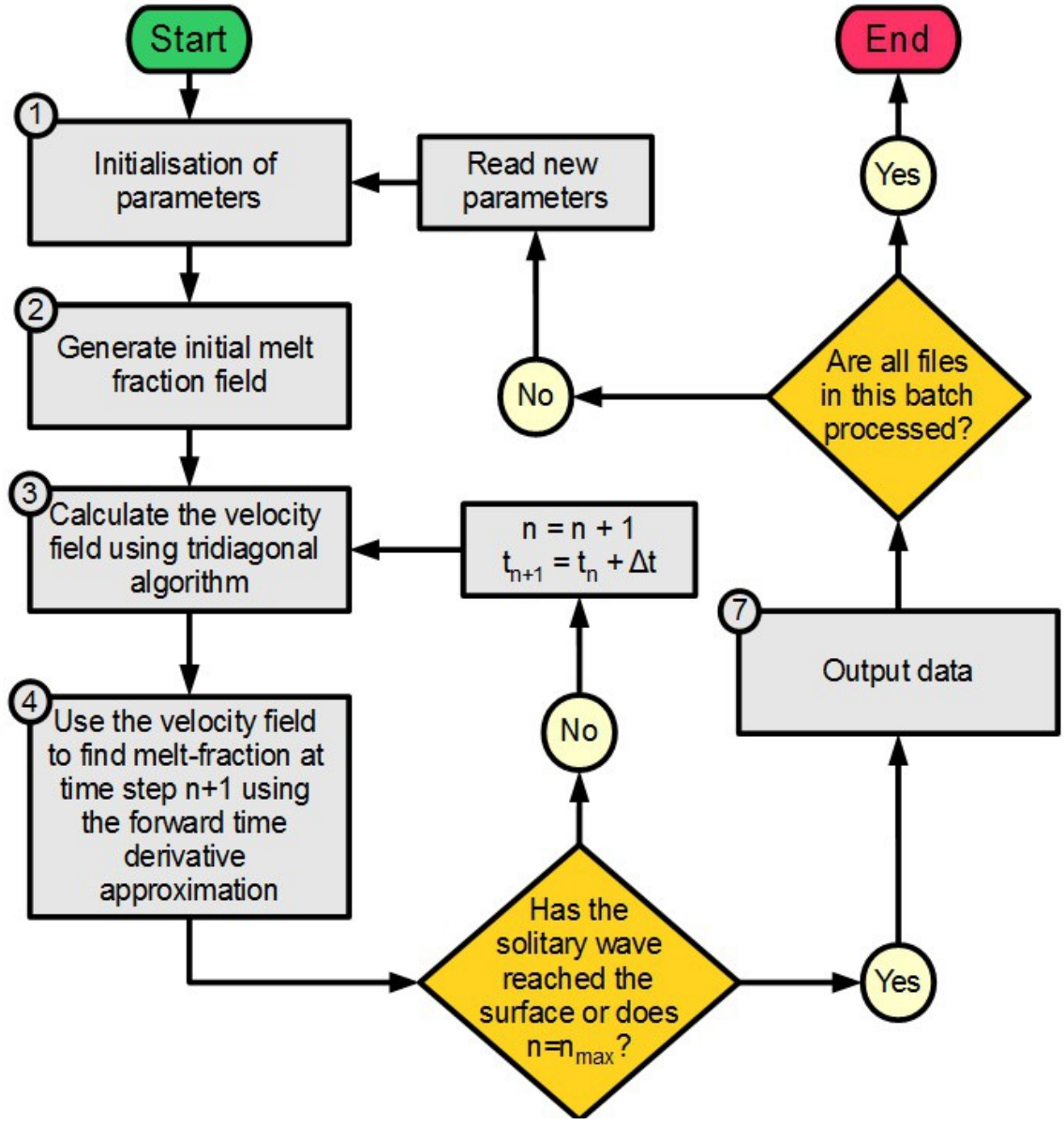


*Figure 13: Flowchart showing the sequence of processes that the one-dimensional two-phase fluid flow program runs through.*

### 3.2.7 Batch processing system

The program is invoked using a batch processing system. An input text file specifies the parameters to use and how many runs the program should do. Complete solutions are output at specific time steps and for requested variables at every time step. With these tools, a great deal can be learnt about the evolution of the system and the impact of each variable on the propagation of the solitary waves.

### 3.2.8 Compaction of an initially constant melt fraction

For the first series of tests I examine how an initially constant distribution of melt fraction evolves over time. For this and all subsequent tests, where not otherwise stated,the following set of constants are used:

| | | | | |
|---|---|---|---|---|
| $\eta_m$ | Matrix viscosity | $1.2 \times 10^{16}$ | Pas | (Kohlstedt and Zimmerman, 1996) |
| $\eta_f$ | Fluid viscosity | 10 | Pas | (Shaw, 1969) |
| $k_0$ | Permeability constant | $6.6 \times 10^{-8}$ | $m^2$ | (Spiegelman, 1993a) |
| $\rho_m$ | Matrix density | 3380 | $kgm^{-3}$ | (Dziewonski and Anderson,1981) |
| $\rho_f$ | Fluid density | 2785 | $kgm^{-3}$ | (Ohtani and Madea, 2001) |
| $g$ | Gravitational Acceleration | 9.81 | $ms^{-2}$ | - |
| $\varphi_0$ | Background melt fraction | 0.001 | - | - |
| $n$ | Permeability power | 2 | - | (Nakayama and Mason, 1995) |
| $A$ | Perturbation amplitude | 0.01 | - | - |
| $\sigma$ | Perturbation width parameter | 100 | mm | (equation 3.10) |

*Table 1: Table of standard constants and parameters used in the one-dimensional two-phase numerical experiments described in the following sections. In some tests I changed specific parameters, such as the width of the initial perturbation or the viscosity of the matrix.*

To test the correct operation of the program, I compare the numerical solution to analytical solutions given first by McKenzie (1984). Using the constants defined by McKenzie (1984) a time-dependent compaction solution can generated using the numerical methods outlined in chapter 2.

However, it should be noted that McKenzie (1984) used a different version of the permeability function (equation 2.6):

$$k_{\varphi} = k_0 \frac{\varphi^3}{(1-\varphi)^2} \tag{3.24}$$

where $k_0$ is also different to the constants I use. To compare my solutions directly to those by McKenzie (1984) I use the same initial condition (constant melt fraction, discussed in Section 1.4) and a value of $k_0$ that allows the matching of equation 2.6 and 3.24. Furthermore, McKenzie (1984) uses both the bulk viscosity $\zeta$ and shear viscosity $\eta_m$, deriving an intrinsic length scale for the system called the 'compaction length' as discussed in sections 1.4.1 and 2.5:

$$\delta_c = \left( \frac{(\zeta + 4/3\,\eta_m) k_{\varphi}}{\eta_f} \right)^{\frac{1}{2}} \tag{3.25}$$

where as I use a single matrix viscosity constant, $\eta_m = \zeta$. McKenzie (1984) designates the compaction length as the term $q$ in an equation of the form:

$$\frac{\partial^3 V}{\partial z^3} - q^2 \frac{\partial V}{\partial z} = 0 \tag{3.26}$$

I can reproduce the compaction length for this system of calculations by differentiating equation 3.4 with respect to $z$ and treating the melt fraction as a constant:

$$\frac{\partial^3 V}{\partial z^3} - \frac{3\varphi}{3+\varphi} \frac{\eta_f}{k_o \eta_m \varphi^n} \frac{\partial V}{\partial z} = 0 \tag{3.27}$$

which defines the compaction length for the formulation as:

$$q = \delta_c = \left( \frac{3+\varphi}{3\varphi} \frac{\eta_m k_0 \varphi^n}{\eta_f} \right)^{\frac{1}{2}} \tag{3.28}$$

This equation has many of the same elements as the length-scale for non-dimensionalisation (Equation 2.54), but Equation 3.28 is not preferable for use as a non-dimensionalisation constant as it is a function of melt fraction, which is not always constant.

With the values used by McKenzie (1984) (Table 2) and allowing for the difference in specific permeability function, 3.28 becomes:

$$\delta_c = 124\,\mathrm{m} \tag{3.29}$$

| | | | |
|---|---|---|---|
| $\eta_m$ | Dynamic shear viscosity | $10^{15}$ | Pas |
| $\eta_f$ | Fluid viscosity | 1 | Pas |
| $\zeta\zeta$ | Bulk viscosity | $10^{15}$ | $m^2$ |
| $\rho_m$ | Matrix density | 3300 | $kgm^{-3}$ |
| $\rho_f$ | Fluid density | 2800 | $kgm^{-3}$ |
| $g$ | Gravitational Acceleration | 9.81 | $ms^{-2}$ |
| $\varphi$ | Melt fraction | 0.1 | - |
| $n$ | Permeability power | 2 | - |
| $k_0$ | Permeability constant | $10^{-9}$ | $m^2$ |
| $\delta_c$ | Compaction length | 53 | m |
| $k_\varphi$ | Specific permeability | $1.2x10^{-12}$ | $m^2$ |
| $w_0$ | Relative velocity with no compaction | $5.3x10^{-8}$ | $ms^{-1}$ |

*Table 2: Specific parameters used by McKenzie (1984) to formulate the analytical solutions in Figures 15-17 and myself for Figures 14-16.*

To compare solutions from my one-dimensional numerical model directly to that of McKenzie (1984) requires application of his non-dimensionalisation system:

$$z' = \frac{z}{\delta_c} \quad V' = \frac{V}{w_0} \quad t' = t\frac{w_0}{\delta_c} \tag{3.30}$$

Using these parameters I generated two solutions with layer thickness of 0.5 and 4 compaction lengths, Figure 14 and (Figure 16) respectively. The units and signs of the solutions have been converted to match the non-dimensionalisation and *z*-direction used by McKenzie (1984) to allow comparison of the two solutions.

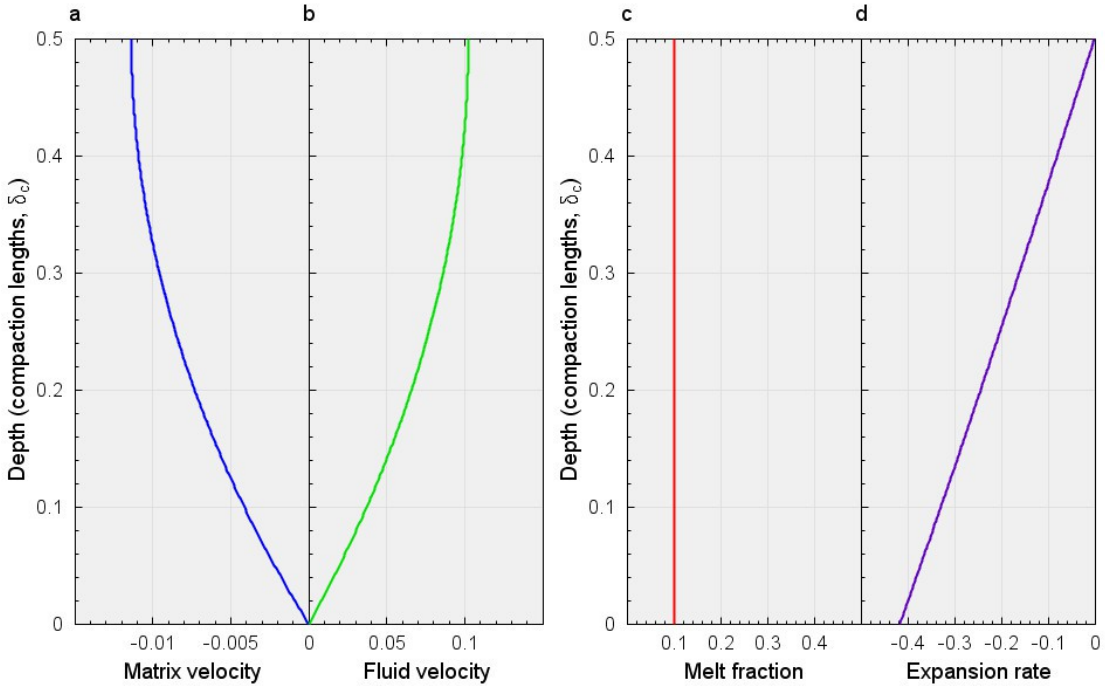


*Figure 14: A one-dimensional numerical solution for an initially constant melt fraction ($\varphi_0$=0.1), and a layer thickness of 0.5$\delta_c$ (equation 3.25). a) shows the velocity of the matrix (mantle) with depth, b) the velocity of the pore fluid (melt) with depth, c) the melt fraction with depth and d), the rate of expansion ($\varphi^{-1}d\varphi/dt$) with depth. All scales are non-dimensionalised to match those used by McKenzie(1984).*

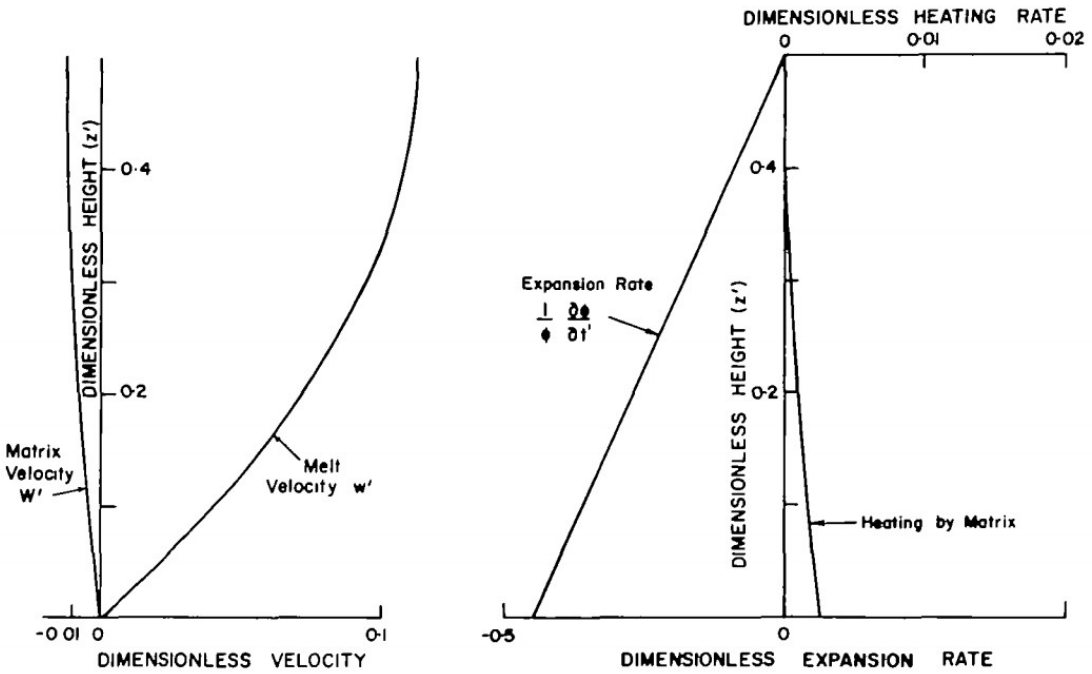


*Figure 15: The initial compaction solution for a constant melt fraction of $\varphi_0$ = 0.1 over a layer thickness of 0.5 compaction lengths ($\delta_c$) by McKenzie (1984). The scales are directly comparable with Figure 14.*

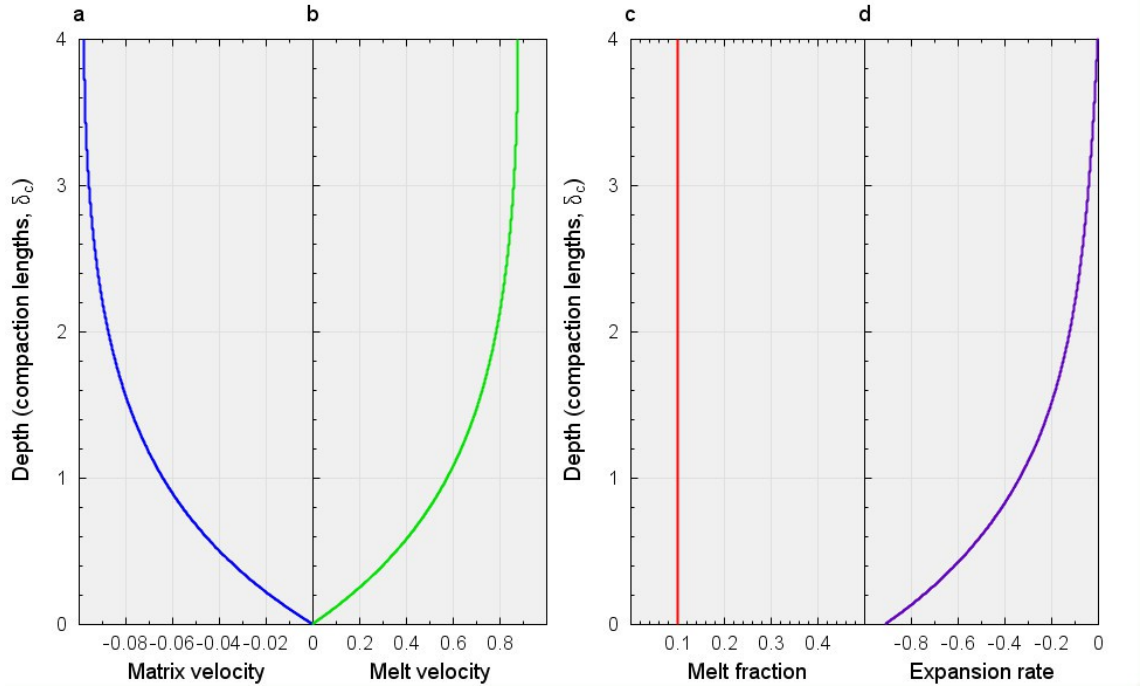


*Figure 16: A one-dimensional numerical solution for an initially constant melt fraction ($\varphi_0$=0.1), and a layer thickness of $4\delta_c$ (equation 3.25). All other parameters are in-line with Figure 14. a) shows the velocity of the matrix (mantle) with depth, b) the velocity of the pore fluid (melt) with depth, c) the melt fraction vs. depth and d) the rate of expansion ($\varphi^{-1}d\varphi/dt$) vs. depth. All scales are non-dimensionalised to match those used by McKenzie(1984).*

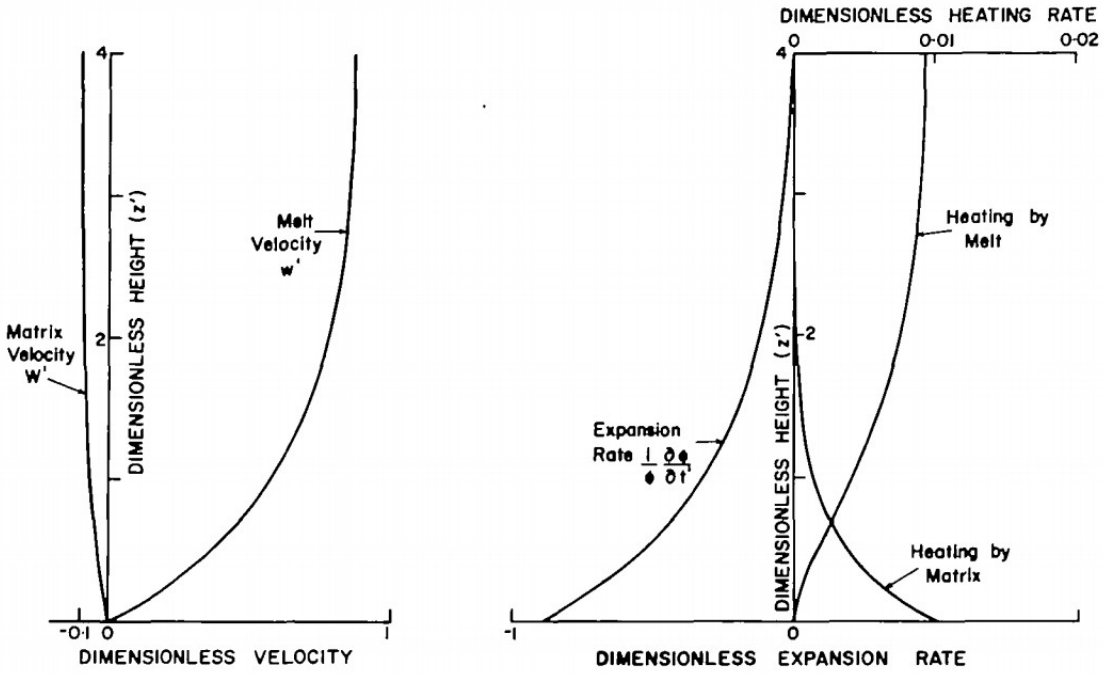


*Figure 17: The initial compaction solution for a constant melt fraction of $\varphi_0$ = 0.1 over a layer thickness of 4 compaction lengths ($\delta_c$) by McKenzie (1984). The scales are directly comparable with Figure 16.*

The solution in Figure 14 is consistent with that of Figure 15. The ratio of the matrix to fluid velocities is around ~11% in both solutions. The expansion rate plot in both figures is a simple straight line for any layer thickness less than the compaction length (McKenzie, 1984). For a layer thickness greater than the compaction length, McKenzie (1984) showed that the expansion rate decreases asymptotically to zero towards the top of the region as shown in Figure 17, which is comparable with my one-dimensional model in Figure 16. The velocity ratios are similarly comparable for Figure 16 and 17.

### 3.2.9 Comparison with analytical solutions

I now confirm the accuracy of the numerical model by comparison to solutions obtained analytically. Assuming that melt fraction is a constant, equation 3.4 reduces to:

$$\frac{d^2V}{dz^2} - q^2V = p \tag{3.31}$$

where:

$$q^2 = \left(\frac{3\varphi}{3+\varphi}\right)\frac{\eta_f}{k_o\eta_m\varphi^n}$$
$$p = -\left(\frac{3\varphi}{3+\varphi}\right)(1-\varphi)\frac{\Delta\rho g}{\eta_m} \tag{3.32}$$

using the boundary conditions discussed in section 3.2.2:

$$V = 0 \text{ at } z = 0 \tag{3.33}$$

and:

$$\frac{dV}{dz} = 0 \quad \text{at } z = h. \tag{3.34}$$

where $h$ is the layer thickness. To create an analytical solution a generic equation that satisfies 3.31 is needed. The solution is:

$$V = E\sinh(qz) + F\cosh(qz) - \frac{p}{q^2} \tag{3.35}$$

Where $E$ and $F$ are constants. It can be show that equation 3.35 is a valid solution to equation 3.31 by back substitution of 3.35 into 3.31.

To evaluate the constants *E* and *F*, the boundary condition (equation 3.33) can be used to obtain:

$$0 = E\sinh(0) + F\cosh(0) - \frac{p}{q^2} \tag{3.36}$$

thus:

$$F = \frac{p}{q^2} \tag{3.37}$$

For the condition 3.34, first differentiate 3.35:

$$\frac{\partial V}{\partial z} = E\,q\cosh(qz) + F\,q\sinh(qz) \tag{3.38}$$

Now apply boundary condition 3.34 to obtain:

$$E = -F\frac{\sinh(qh)}{\cosh(qh)} \tag{3.39}$$

and using equation 3.37 to find *E*:

$$E = \frac{-p}{q^2}\frac{\sinh(qh)}{\cosh(qh)} \tag{3.40}$$

Thus, by substituting equations 3.40 and 3.37 into equation 3.35:

$$V = -\frac{p}{q^2}\frac{\sinh(qh)}{\cosh(qh)}\sinh(qz) + \frac{p}{q^2}\cosh(qz) - \frac{p}{q^2} \tag{3.41}$$

Equation 3.40 then can be rewritten after some manipulation as:

$$V = -\frac{p}{q^2}\left[\frac{\cosh(q(h-z)) - \cosh(qh)}{\cosh(qh)}\right] \tag{3.42}$$

which is the time-zero analytical solution for the matrix velocity of the one-dimensional constant melt fraction problem. This analytical derivation follows the same rules as that used by McKenzie (1984), producing the same result except for *p* which comes from my differing definitions of constants, permeability function and some governing equations.

Furthermore, using equations 3.3 and 3.5, the analytical solutions for the fluid velocity and the expansion rate are:

$$u = \frac{(1-\varphi)}{\varphi}\frac{p}{q^2}\left[\frac{\cosh(q(h-z))-\cosh(qh)}{\cosh(qh)}\right] \tag{3.43}$$

$$\frac{1}{\varphi}\frac{\partial \varphi}{\partial t} = -\frac{(1-\varphi)}{\varphi}\frac{p}{q}\left[\frac{\sinh(q(h-z))}{\cosh(qh)}\right] \tag{3.44}$$

Equations 3.42 to 3.44 can now be compared with the numerical solutions shown in Figure 16 in order to assess the error of the numerical solution.

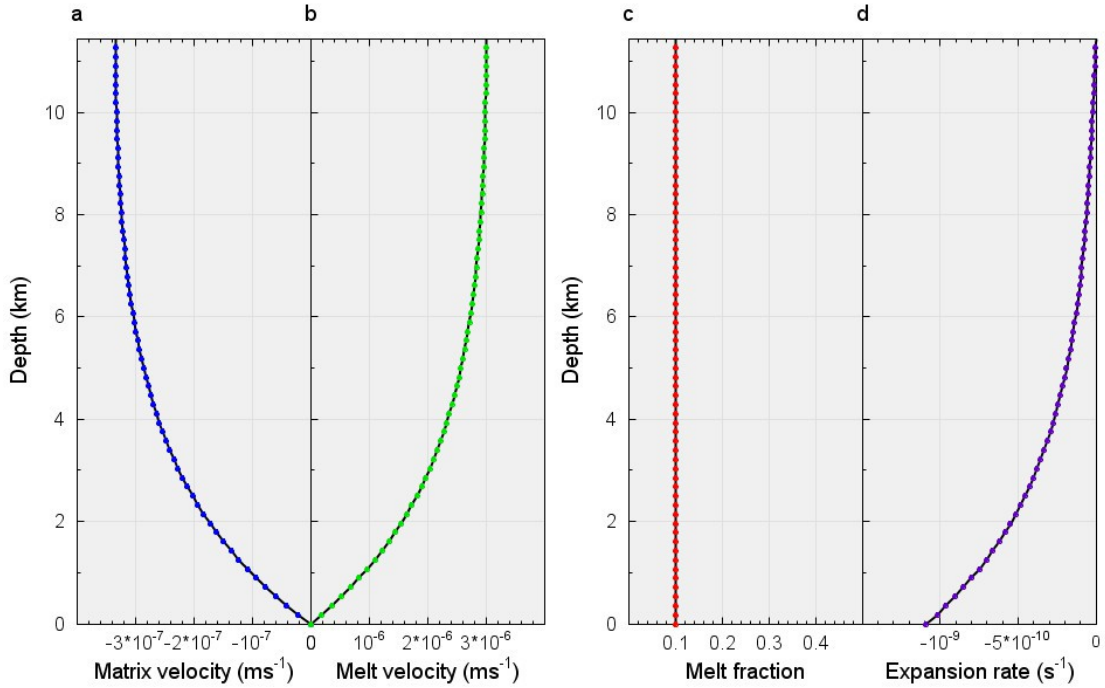


*Figure 18: Comparison of analytical and numerical solutions for initially constant melt fraction. The analytical (black lines) and numerical solution (coloured dots) have a maximum absolute difference as a percentage of the maximum absolute value of 0.0057% for the matrix viscosity. a) shows the velocity of the matrix (mantle), b) the velocity of the pore fluid (melt), c) the melt fraction and d) the rate of expansion (dφ/dt). The analytical solutions are generated by equations 3.42 to 3.44. These tests use the parameters from Table 1 with the exceptions of $\varphi_0$=0.1 and A=0.*

Figure 18 compares the numerical and analytical solutions for compaction of a constant melt fraction in a layer of thickness $4\delta_c$. The numerical and analytical solutions are visually identical. I also computed the maximum absolute difference as a percentage of the maximum absolute value ($m_{diff}$) between the numerical and analytical solutions. I obtained $m_{diff}$ values between the two solutions of 0.0057% (65 points), 0.0047% (129 points) and 0.018% (257 points) for the matrix velocity and 0.047% (65 points), 0.015%

(129 points) and 0.013% (257 points) for the divergence of the matrix velocity (*D)*. Although the errors are negligible, this error analysis does not behave as expected for a reducing discretisation error, implying that rounding error is the principle source of numerical error.

## *3.3 Evolution of solitary waves from an initial melt concentration*

In this section, I investigate the evolution of solitary waves that develop from an initial perturbation (equation 3.10) to the constant background melt fraction. I observe that the initial perturbation is typically not stable, even though it is of similar form to the final perturbation the parameters $A$, $b$ and $\sigma$ evolve over time to satisfy the governing equation. In comparing the initial perturbation to the resulting solitary waves I use the subscript $I$ to refer to the initial parameters at time zero and subscript $S$ for the solitary wave parameters at later times. In each case the constants $A$, $b$ and $\sigma$ describe the location and shape of the primary solitary wave.

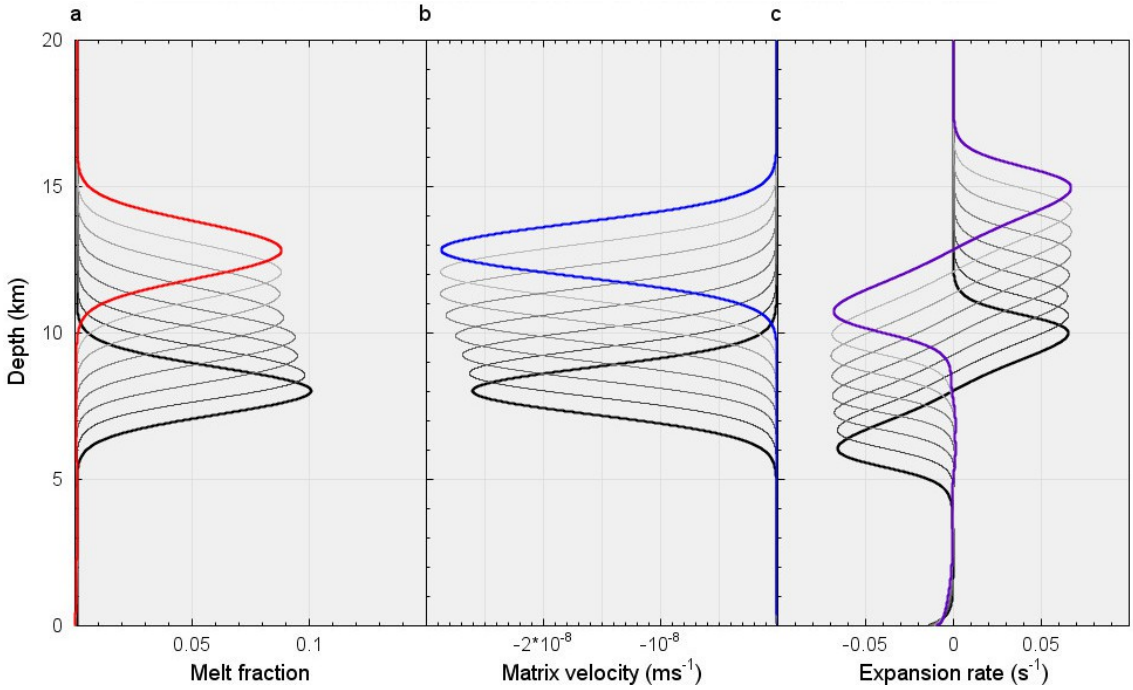


*Figure 19: The evolution of a solitary wave from an initial distribution of melt fraction (3.22), using parameters listed in Table 1 over a total time of 533 years. a) melt fraction, with the red line denoting the final stable solitary wave, b) matrix velocity and c) expansion rate. The thick black lines are the initial conditions at time step zero and the grey lines show the solutions at intervals of ~80 years.*

Figure 19 demonstrates how an initial melt fraction with a Gaussian perturbation evolves over time. In Figure 19a, the waveform parameters adjust as the initial perturbation evolves into a solitary wave. In this case the amplitude changes from $A_I$ = 0.1 to $A_S$ =0.08929, while the width of the solitary wave increases from $\sigma_I$ = 800m to $\sigma_S$ = 920m or, in terms of full width at half maximum, 1884m to 2168m. Thus the medium itself has a preferred set of parameters for solitary waves depending on the background

melt fraction and physical parameters such as permeability and viscosity. I investigate which parameters determine different aspects of the final solution in subsections 3.3.1 and 3.3.2, whereas in this subsection I describe in more detail the character of a typical solitary wave in this system. The expansion rate in Figure 19c illustrates the wave-like propagation of the solitary wave as the melt fraction increases ahead of the wave and then decreases behind it. The leading part of the wave is in dilatation while the trailing part is compacting. The matrix expands to concentrate melt at the top of the wave before contracting again at the base, leaving little if any disturbance to the background melt fraction in its wake. The description of this dilatation/compaction field reinforces the fact that a solitary wave is not a discrete pulse of melt rising through the mantle, but more a disturbance to the matrix pore space that transports melt as it moves.

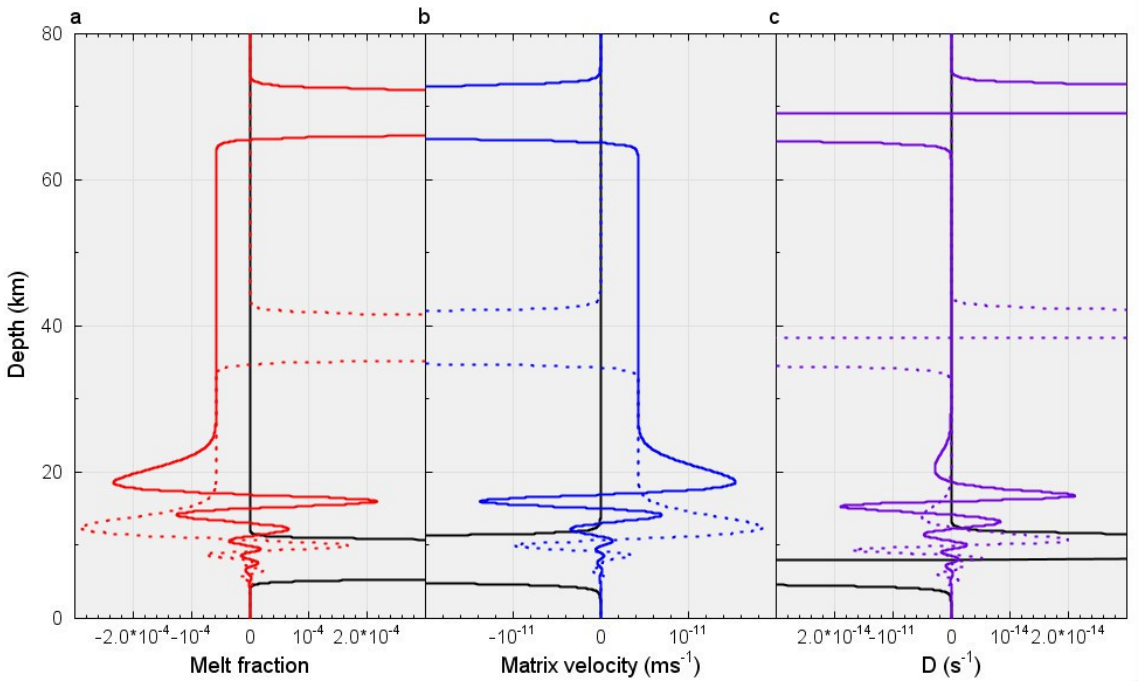


*Figure 20: Differences between an experiment with initially uniform melt fraction of $\varphi_0$ = 0.001 and one in which the Gaussian perturbation in Figure 19 is added to the uniform background. Solid lines show differences in value at time t = 6338yr for a) melt fraction, b) downward matrix velocity and c) expansion rate. Black lines and dashed lines show detail of the solution that includes the initially Gaussian melt-function distribution at times t = 0 and t = 3169yr. The horizontal scale has been reduced to show small scale amplitudes clearly, to a) 0.3%, b) 0.08% and c) 0.2% of the maximum initial values.*

In Figure 20, I show the differences in the field values, $V$, $\varphi$ and $D$ between a compaction solution for a layer with $h$ = 80km and $\varphi_0$ = 0.001, and the same solution with a solitary wave (like that of Figure 19: $A$ = 0.01, $b$ = 8km and $\sigma$ = 800m) added.

This graph demonstrates that as the solitary wave rises there is loss of the background melt fraction of around 0.065% of the solitary wave peak amplitude or 5.8% of the initial background melt fraction $\varphi_0$ with a small corresponding increase in solitary wave amplitude. This small decrease in the background melt fraction could explain the slight amplitude increase of the solitary wave over time on the order of 0.1% as described by Barcilon and Richter (1986). The disturbance at the base of Figure 20 is similar to the result of interaction between two solitary waves shown by Barcilon and Richter (1986). The disturbance to the melt fraction is not due to numerical instability, as the shape and magnitude of the disturbance is not affected by changes in the mesh size. The magnitude and number of these diminishing sinusoidal features is related to the initial perturbation, the disturbance diminishing completely as the first secondary wave begins to form.

After elapsed times of about 533 yr, the wave in Figure 19 exhibits a phase velocity of 10.4 m/yr while the fluid travels at a peak speed of 9.76 m/yr and there is little change in the amplitude and width parameters, which remain fairly stable as it continues to rise (Figure 21).

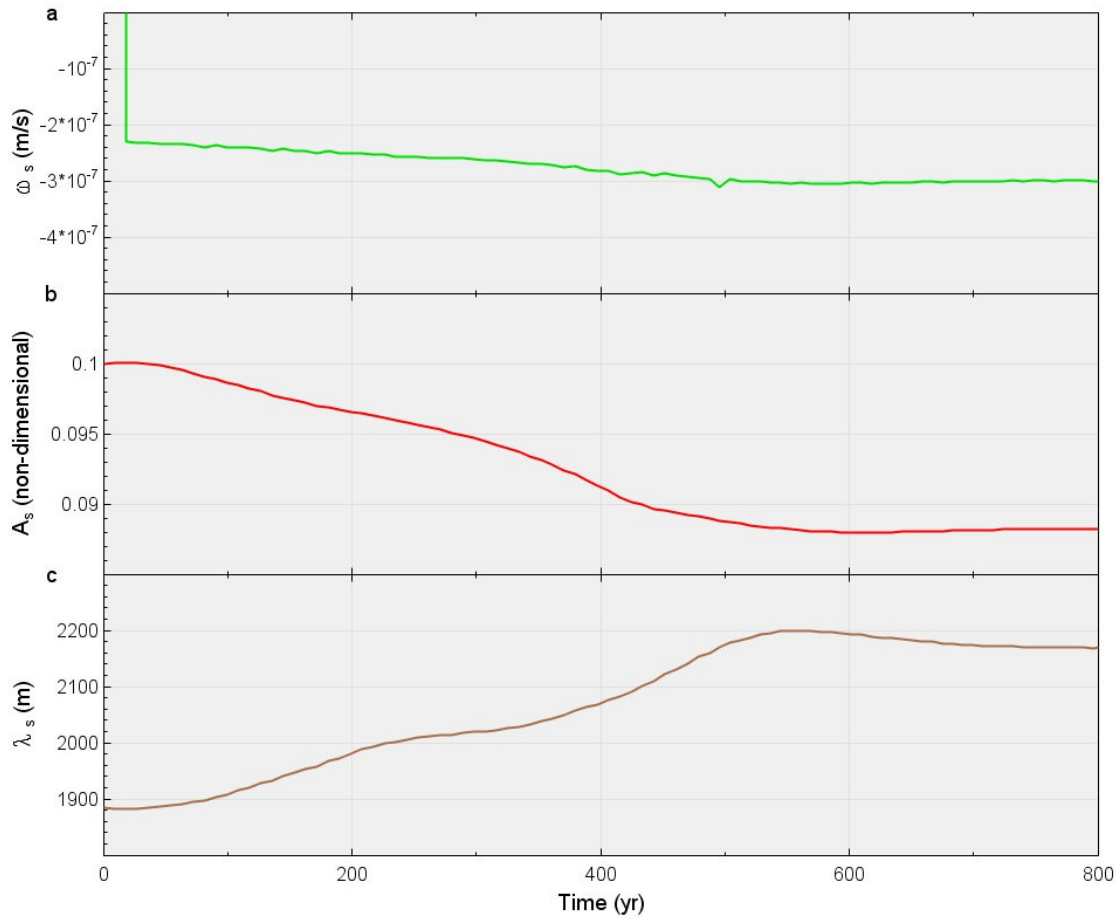


*Figure 21: The evolution of the primary solitary wave shown in Figure 19 following the initial perturbation. a) the solitary wave phase velocity, b) the amplitude, and c) the full width at half maximum of the solitary wave. This particular solitary wave stabilizes at around 500 years after initialisation.*

I examine the solitary wave at later times by calculating an RMS best fit of the computed melt fraction curve to equation 3.22, deriving values for its amplitude, full width at half maximum and position. As Figure 21 shows, the solitary wave requires time to evolve from the initial perturbation into a stable form, but it does so over a relatively short depth range (Figure 21), meaning that the wave is fully formed and stable well before interaction with the upper boundary takes place.

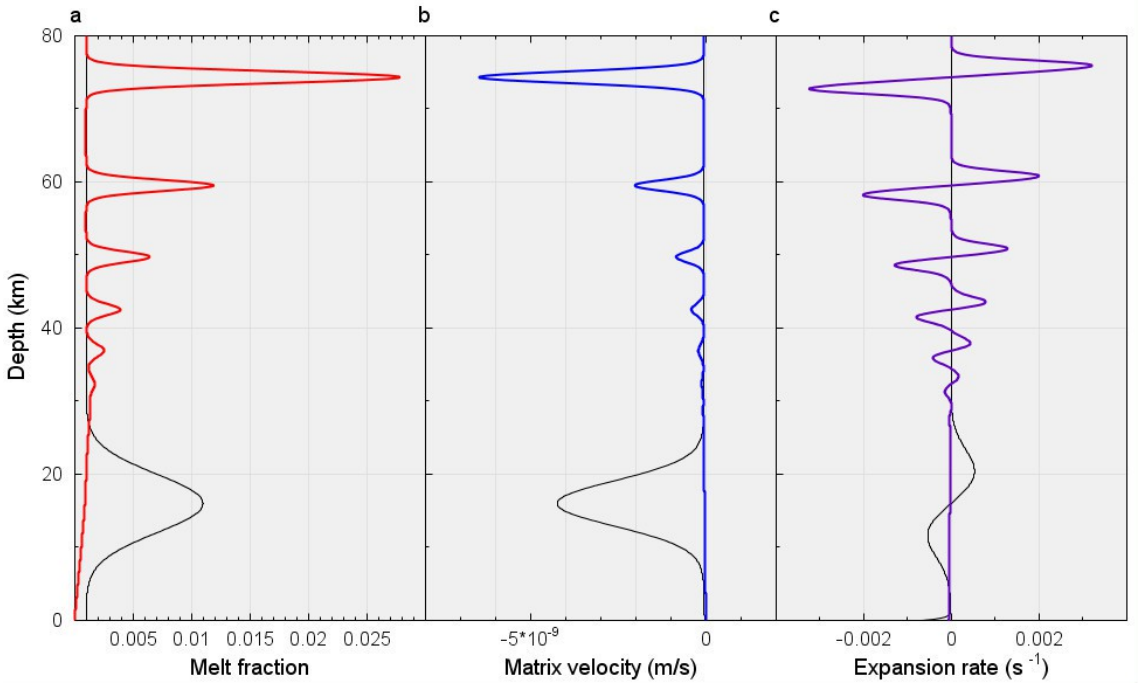


*Figure 22: The formation of a wave train from an initial distribution of melt fraction (3.22). The black line shows the initial melt fraction, matrix velocity and expansion rate profiles. This solution uses the parameters from Table 1 a the exception $\sigma_I$=4 km. The red line is the melt fraction after elapsed time 7129 yr, the blue line is the corresponding matrix velocity field and the purple line is the expansion rate. Several solitary waves evolve from the one perturbation to the melt fraction, each decreasing in amplitude and propagation velocity, in rank order.*

As mentioned earlier the initial Gaussian perturbation does not always result in a single solitary wave but can evolve into a group of waves, referred to as a wave train. Figure 22 shows an example of a wave train that developed from an initial unstable Gaussian perturbation. These waves are each smaller in amplitude and travelling with lesser phase velocity than the one preceding, I further discuss solitary wave trains in detail in section 3.4.

For the primary solitary wave in Figure 22 after steady propagation is attained, the wave moves at 8.078 m/yr while the fluid travels at a peak speed of 7.124 m/yr and the matrix moves in the opposite direction with a peak velocity of 0.2039 m/yr.

I have demonstrated that the one-dimensional model can reproduce propagating waves of melt fraction which transport magma through a permeable deforming matrix, exhibiting properties similar to those described by other authors, including stable wave form (Barcilon and Lovera, 1989; Scott and Stevenson, 1984; Nakayama and Mason, 1992).

### 3.3.1 Effects of altering the parameters of the initial perturbation

In this section, I vary the parameters that define the initial distribution of the melt fraction in order to show the impact on formation of stable propagating waves. The two constants that define the initial amplitude, $A_I$, and initial width constant, $\sigma_I$, together describe the one-dimensional volume of the initial perturbation:

$$Vol_I = 2\sqrt{\pi} A_I \sigma_I = \sqrt{\pi / (2\ln 2)}\, A_I \lambda_I \qquad (3.45)$$

where $\lambda_I$ is the full width at half maximum of the perturbation. I now describe the effect of independently varying the initial amplitude $A_I$ and initial width $\lambda_I$, and thus the volume $Vol_I$, of the resulting primary solitary wave. To do so I ran batches of experiments where only $A_I$ was changed or only $\lambda_I$ was changed while all other constants expressed in Table 1 remained the same.

When a train of solitary waves is produced from this type of initial condition (equation 3.22), the individual solitary waves are generally dispersed by a propagation velocity which increases with the amplitude of the solitary wave (Figure 23c). I refer to the lead solitary wave in such a train as the primary, and below I focus on its properties.

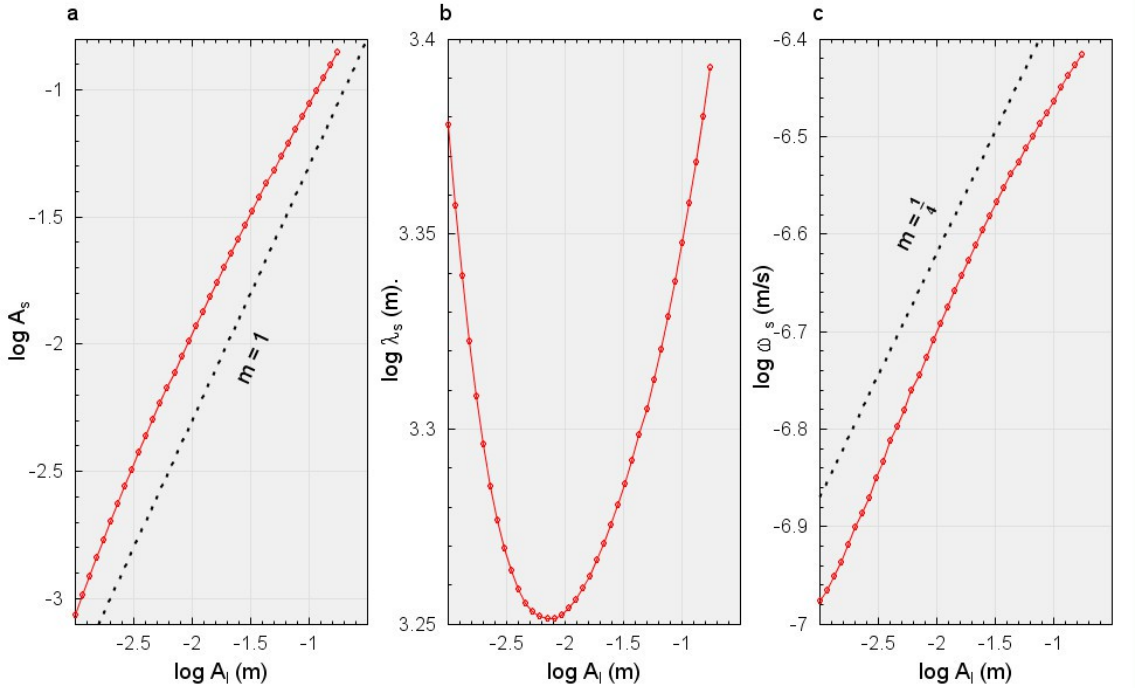


*Figure 23: Parameters of stable solitary waves in experiments where the amplitude of the initial perturbation ($A_I$) was altered (defined by equation (3.10)). Graph 23a is the solitary wave amplitude ($A_S$), 23b is the full width at half maximum ($\lambda_S$) and 23c is the phase velocity ($\omega_S$). All other parameters are defined in Table 1. The black lines are linear functions of gradient m. These are dimensional log10-log10 plots to clearly show variation over orders of magnitude.*

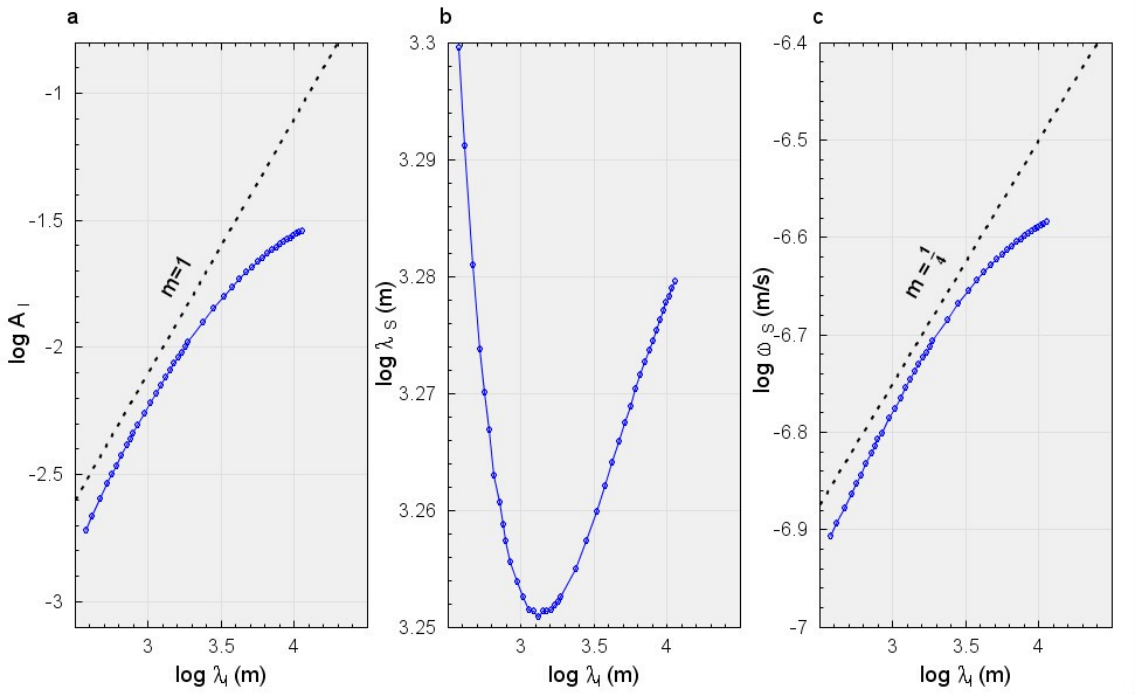


*Figure 24: Parameters of stable solitary waves in experiments where the width of the initial perturbation ($\lambda_I$) was altered (defined by equation (3.10)). Graph 24a is the solitary wave amplitude ($A_S$), 24b is the full width at half maximum ($\lambda_S$) and 24c is the phase velocity ($\omega_S$). All other parameters are defined in Table 1. The black lines are linear functions of gradient m. These are dimensional log10-log10 plots to clearly show variation over orders of magnitude.*

The wave trains illustrated in Figure 22 show a characteristic pattern of decreasing volume in successive wave packets. Figure 23c shows a relatively weak dependence of propagation velocity on solitary wave amplitude (an increase of a factor of about 4 as solitary wave volume is increased by two orders of magnitude) but this increase clearly explains the dispersion of the solitary wave trains discussed in section 3.4. The relationship between solitary wave amplitude and phase speed is discussed by Barcilon and Richter (1986) who compare phase velocity to solitary wave amplitude. The increase in propagation velocity associated with larger initial perturbation widths (Figure 24c) is probably due largely to the increase in solitary wave amplitude shown in Figure 24a. Intriguingly, a well-defined minimum solitary wave width of 1780m is found for a solitary wave volume of 15m for only the specific parameters used in Figure 24. This minimum ($\lambda_{crit}$) is further investigated in section 3.3.2 and is shown to depend on the melt fraction independent compaction length (δ, Equation 2.54). The width of the stable solitary waves varies only by about 30% in all of these experiments, but this property is also a function of δ. The small range of observed widths indicates that there

is a specific preferable configuration for the solitary wave dependant on the physical properties of the medium, such as viscosity and permeability.

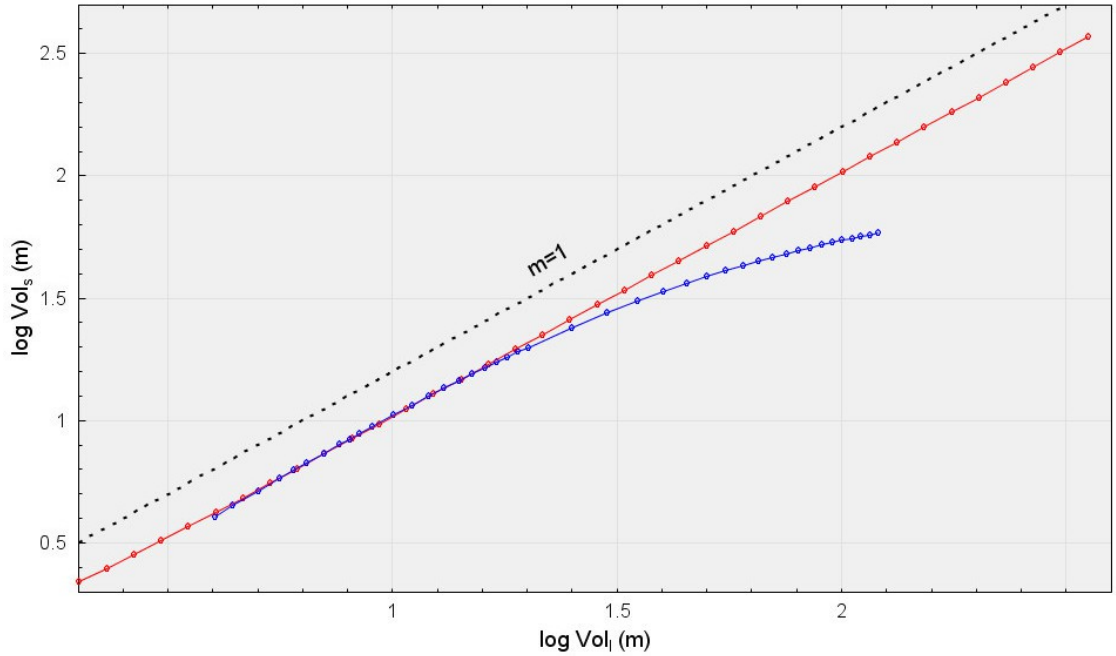


*Figure 25: Volume of the stable primary solitary waves ($Vol_S$) that evolve from initial perturbations of differing initial volumes ($Vol_I$) as defined by equation (3.22). The red line relates to experiments were the initial amplitude ($A_I$) of the perturbation was altered over the range of 0.001 to 0.18 with a constant width, $\lambda_I$ = 1.884 km. The blue line plots experiments where the width of the initial perturbation was altered between 0.3768 km and 9.419 km with $A_I$ = 0.01 constant. All other parameters are constants as defined in Table 1. The black line is a linear function of gradient m=1 ($V_s$=$V_I$ displaced vertically).*

For the right initial width ($\lambda_I$) the volume of the stable propagating wave is the same as the volume of the initial perturbation (Figure 25, red curve). As the width of the initial perturbation is systematically increased the ratio of $Vol_s$ to $Vol_I$ changes. For small widths, $Vol_S$ = $Vol_I$, but above some threshold of $\lambda_I$ the primary solitary wave volume ($Vol_S$) is less than the initial volume ($Vol_I$) (Figure 25, blue curve). This apparent loss of volume is caused by some of the initial melt being partitioned into the secondary waves.

When the width constant $\lambda_I$ is greater than the critical width (Figure 24), secondary solitary waves develop in the solution. The formation of these secondary waves explains the discrepancy between $Vol_I$ and $Vol_S$ seen in Figure 25. However, the critical value of 1780m from Figure 24 applies specifically to the case of $\delta$=8900m (derived from Table 1) which is discussed further in the next section.

### 3.3.2 Effects of altering the viscosities of matrix and melt and permeability constant.

Although other authors have considered a relatively complex dependence of matrix viscosity on melt fraction e.g., (Nakayama and Mason, 1999; Scott and Stevenson, 1984, 1986) I here examine solutions in which the matrix viscosity ($\eta_m$) is constant. While mantle viscosity in these regions may be on the order of $2.6\text{x}10^{17}$ to $5.2\text{x}10^{18}$Pas (e.g. Nooner et al., 2009; Kohlstedt and Zimmerman, 1996)**,** the onset of partial melting can reduce matrix viscosity by orders of magnitude as indicated by Kohlstedt et al., (1996). I therefore vary the value of $\eta_m$ in the range $10^{14}$ to $10^{17}$Pas in the series of calculations shown in Figure 26. Fluid viscosity, likewise, is variable within magmatic systems. This variation depends on temperature, pressure and composition of melt (Shaw, 1969) but for the purposes of this study, I assume viscosity is constant, and consider values in the range 1 to 1000Pas (Figure 27). Figure 28 explores the impact of variation in the permeability constant, between $1.0\text{x}10^{-9}$ to $1.0\text{x}10^{-7}\text{m}^2$.

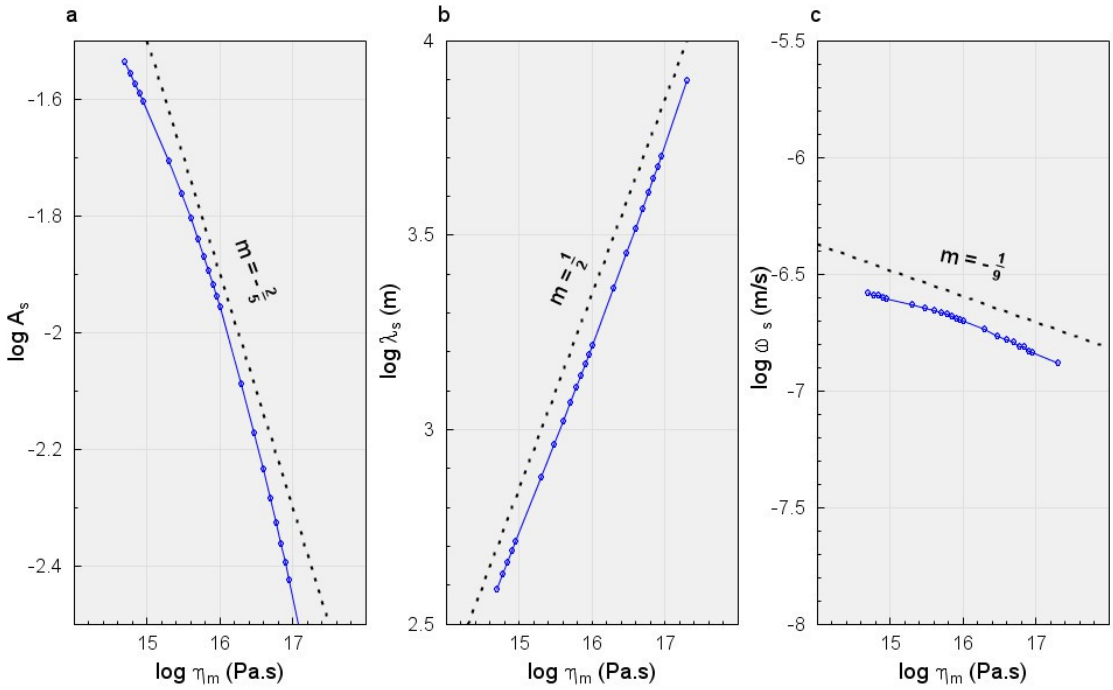


*Figure 26: Parameters of stable solitary waves in experiments where the matrix viscosity ($\eta_m$) was altered. Graph 26a is the solitary wave amplitude ($A_S$), 26b is the full width at half maximum ($\lambda_S$) and 26c is the phase velocity ($\omega_S$). All other parameters are defined in Table 1. The black lines are linear functions of gradient m, listed in Table 3. These are dimensional log10-log10 plots to clearly show variation over orders of magnitude.*

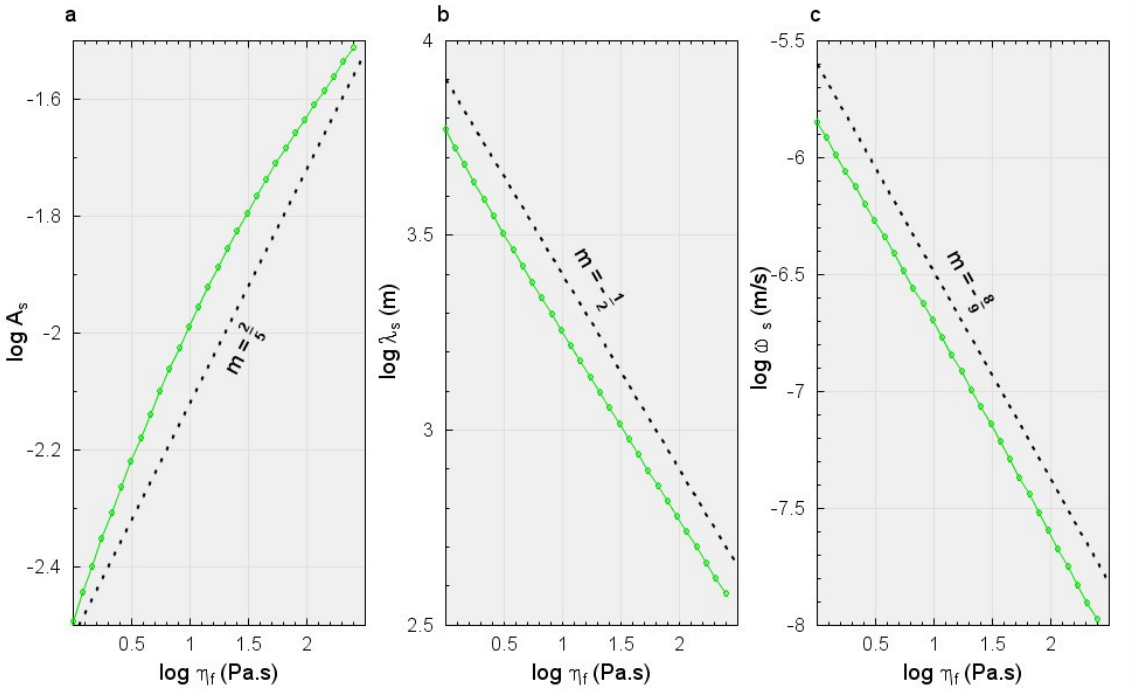


*Figure 27: Parameters of stable solitary waves in experiments where the fluid viscosity ($\eta_f$) was altered. Graph 27a is the solitary wave amplitude ($A_S$), 27b is the full width at half maximum ($\lambda_S$) and 27c is the phase velocity ($\omega_S$). All other parameters are defined in Table 1. The black lines are linear functions of gradient m, listed in Table 3. These are dimensional log10-log10 plots to clearly show variation over orders of magnitude.*

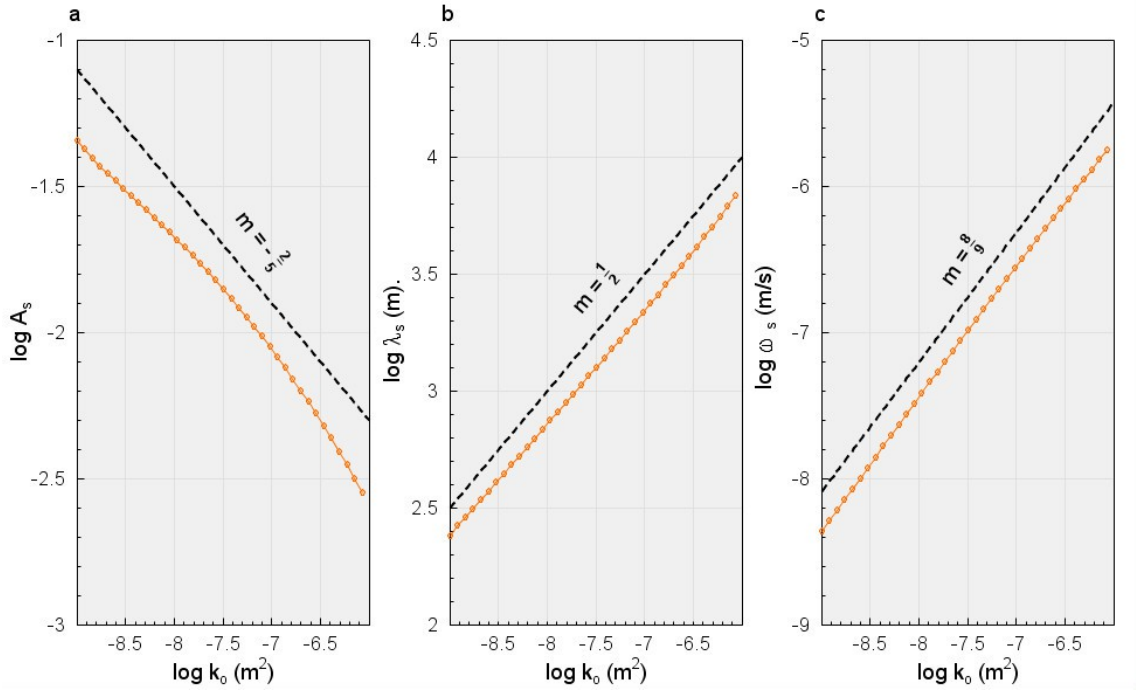


*Figure 28: Parameters of stable solitary waves in experiments where the permeability constant ($k_0$) was altered. Graph 28a is the solitary wave amplitude ($A_S$), 28b is the full width at half maximum ($\lambda_S$) and 28c is the phase velocity ($\omega_S$). All other parameters are defined in Table 1. The black lines are linear functions of gradient m, listed in Table 3. These are dimensional log10-log10 plots to clearly show variation over orders of magnitude.*

| Slope (m) for: | $\eta_m$ experiments | $\eta_f$ experiments | $k_0$ experiments |
|---|---|---|---|
| *Log* $A_s$ | -0.4 | 0.4 | -0.4 |
| *Log* $\lambda_s$ | 0.5 | -0.5 | 0.5 |
| *Log* $\omega_s$ | -0.11 | -0.88 | 0.88 |

*Table 3: Slopes of the black lines shown in Figures 26-28. The first row relates to 26a-28a, the second row to Figures 26b-28b and the last row to Figures 26c-28c.*

Best-fit properties of the stable solitary wave measured from the numerical experiments shown in Figure 26-28 and listed in Table 3 show a simple empirical relation for the width of the primary solitary wave. The relationships shown in these values indicate that $\delta$ (equation 3.28) is a key variable determining the evolution of the system. To explore the influence of the melt fraction independent compaction length, I combine the data shown in Figures 26, 27 and 28, calculating $\delta$ for each experiment to produce a common scale between all three experiments.

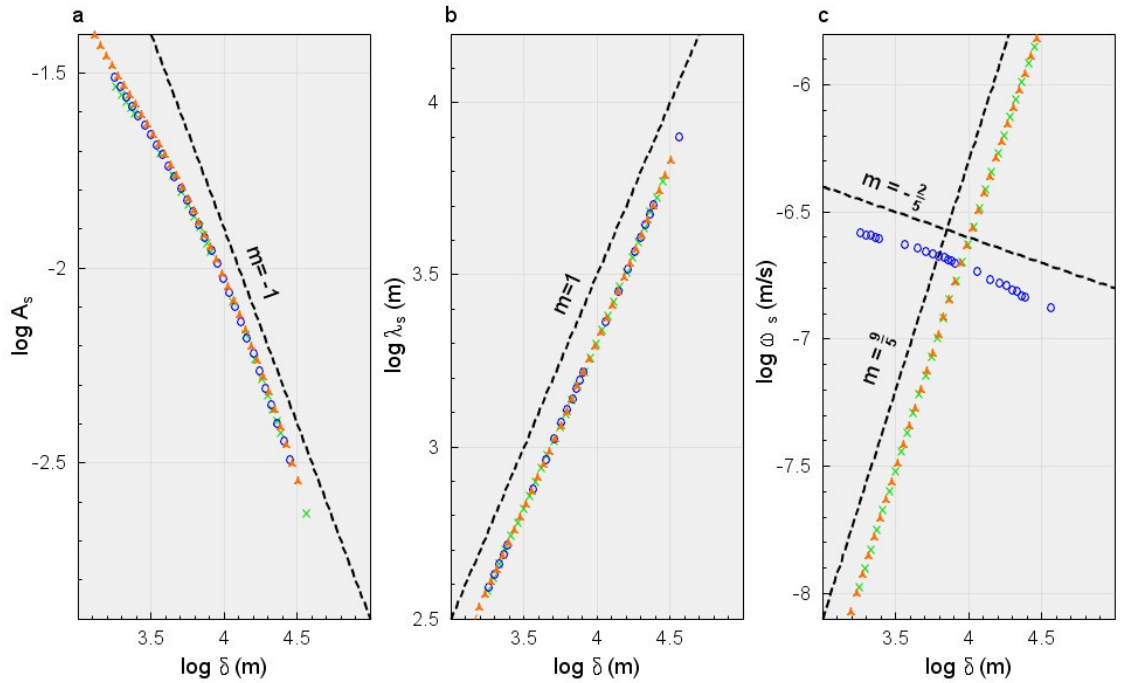


*Figure 29: Parameters of stable solitary waves in experiments where the matrix viscosity ($\eta_m$, blue circles), fluid viscosity ($\eta_f$, green crosses) or the permeability constant ($k_0$, orange triangles) was altered, keeping the other parameters fixed. Graph 29a is the solitary wave amplitude ($A_S$), 29b is the full width at half maximum ($\lambda_S$) and 29c is the phase velocity ($\omega_S$). All other parameters are defined in Table 1. In these graphs I used log10-log10 plots to clearly show variation over orders of magnitude. The x-axis is in units of compaction lengths (δ) as defined by equation (2.54). The black dashed lines have constant slope m.*

I use the melt fraction independent compaction length (δ, Equation 2.54) for this comparison, as the melt fraction is not a constant in these experiments.Figure 29 demonstrates the dependence of the stable primary solitary wave on the melt fraction independent compaction length (δ), allowing the definition of the following empirical statements. Figure 29b shows that the solitary wave width is simply proportional to δ:

$$\lambda_S \simeq 4.6\,\delta \tag{3.46}$$

while the amplitude (Figure 29a) is approximately inversely proportional to δ for the greater melt fraction independent compaction lengths:

$$A_S \simeq 89/\delta \tag{3.47}$$

which implies an almost inverse relationship between $A_s$ and $\lambda_s$, when either matrix or fluid viscosity is altered; in either case a key parameter is the ratio of fluid to matrix viscosity. The deviation from equation 3.47 in Figure 29a can be attributed to the

increasing role of secondary solitary waves.

The phase velocity of the solitary wave (from Figure 29) can be expressed as:

$$\omega_s \approx C_1 \delta^{16/9} (\eta_m)^{-1} \tag{3.48}$$

The solitary wave propagation velocity is almost inversely proportional to the fluid viscosity ($m$ = -0.88) and almost proportional to the permeability constant ($m$ = 0.88), but only weakly negatively correlated with the matrix viscosity (Figures 26-28c). Through its dependence on the melt fraction independent compaction length ($\delta$, Equation 2.54) the dependence of propagation velocity on fluid viscosity and permeability constant may be explicitly stated; the $C_1$ term is a constant empirically determined from Figure 29c. Barcilon and Richter (1986) state that the solitary wave velocity is a function of the solitary wave amplitude and background melt fraction, however Figures 26-29 show that the melt fraction independent compaction length and matrix viscosity are also determinants of the propagation rate. The solitary wave in general propagates faster than the fluid flows in the pores; the matrix moves in the opposite direction at the much slower speeds so as to conserve mass, as described in Section 3.2.8.

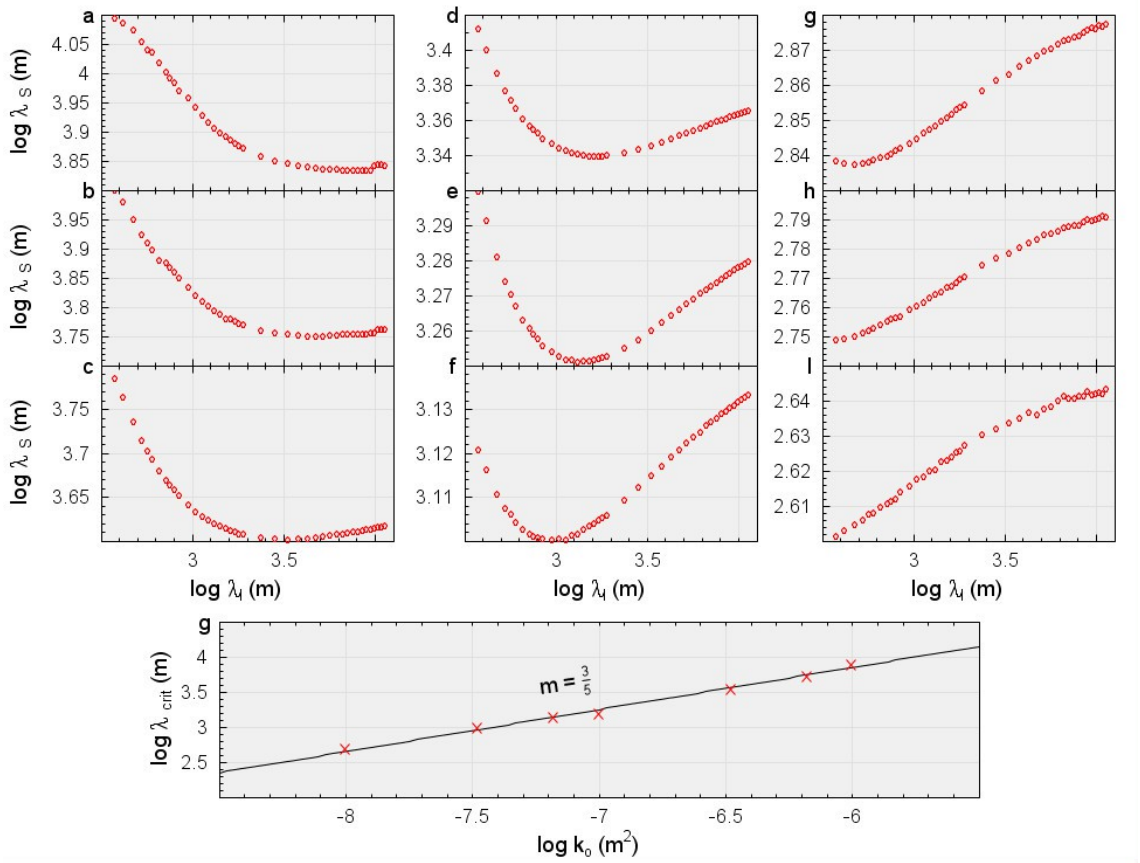


*Figure 30: Widths of the primary solitary wave generated from initial perturbations with initial widths ($\lambda_I$) between 376.8 to 11300m. Between each set of experiments the permeability constant $k_0$ was changed where $k_0$=9.9x10$^{-7}$ for (a), 6.6x10$^{-7}$ for (b), 3.3x10$^{-7}$ for (c), 9.9x10$^{-8}$ for (d), 6.6x10$^{-8}$ for (e), 3.3x10$^{-8}$ for (f), 9.9x10$^{-9}$ for (g), 6.6x10$^{-9}$ for (h) and 3.3x10$^{-9}$ for (i). g shows the critical solitary wave width ($\lambda_{crit}$, value of $\lambda_I$ that results in the minimum $\lambda_s$) for each $k_0$. The black line has constant slope m.*

In Figure 30, I examine widths value of stable solitary waves for different values of the permeability. In each set of experiments the width of the initial perturbation is altered in the same way as Figure 24b, where Figure 30e is identical to Figure 24b. In each set of experiments (Figure 30a-d, f-i) the permeability constant was altered as specified, showing that the minimum width of the primary solitary wave is proportional to the permeability. The initial width that produces the primary wave with the smallest width ($\lambda_{crit}$) is also proportional to the permeability as shown in Figure 30g.

## *3.4 Multiple solitary waves*

Figure 22 illustrates clearly that a large disturbance in the melt fraction can lead to a long train of solitary waves, consistent with solutions demonstrated by Spiegelman (1993b) and Scott and Stevenson (1984). Those authors used a sharp delta function to create the permeability discontinuity that initiated solitary wave formation, whereas I use an initial distribution that conforms to the stable solitary wave packets studied by Barcilon and Richter (1986). I have demonstrated that some such initial melt concentrations propagate with very similar parameters to the initial perturbation, whereas in other cases, they evolve into longer wave trains of spatially dispersed melt concentrations.

For each experiment, the number of waves in a solitary wave train, once the primary wave reached the surface, were manually counted. These results are shown in Figure 31 for a maximum of seven solitary waves in a train. Only seven waves are counted as the amplitudes of waves beyond this limit are too small to discern. Figure 31a demonstrates that the number of solitary waves generated is inversely proportional to the melt fraction independent compaction length (Equation 2.54) while Figure 31b demonstrates that variation in amplitude of the initial perturbation does not affect creation of secondary solitary waves, whereas variation in the initial width results in longer solitary wave trains with increasing initial pulse widths.

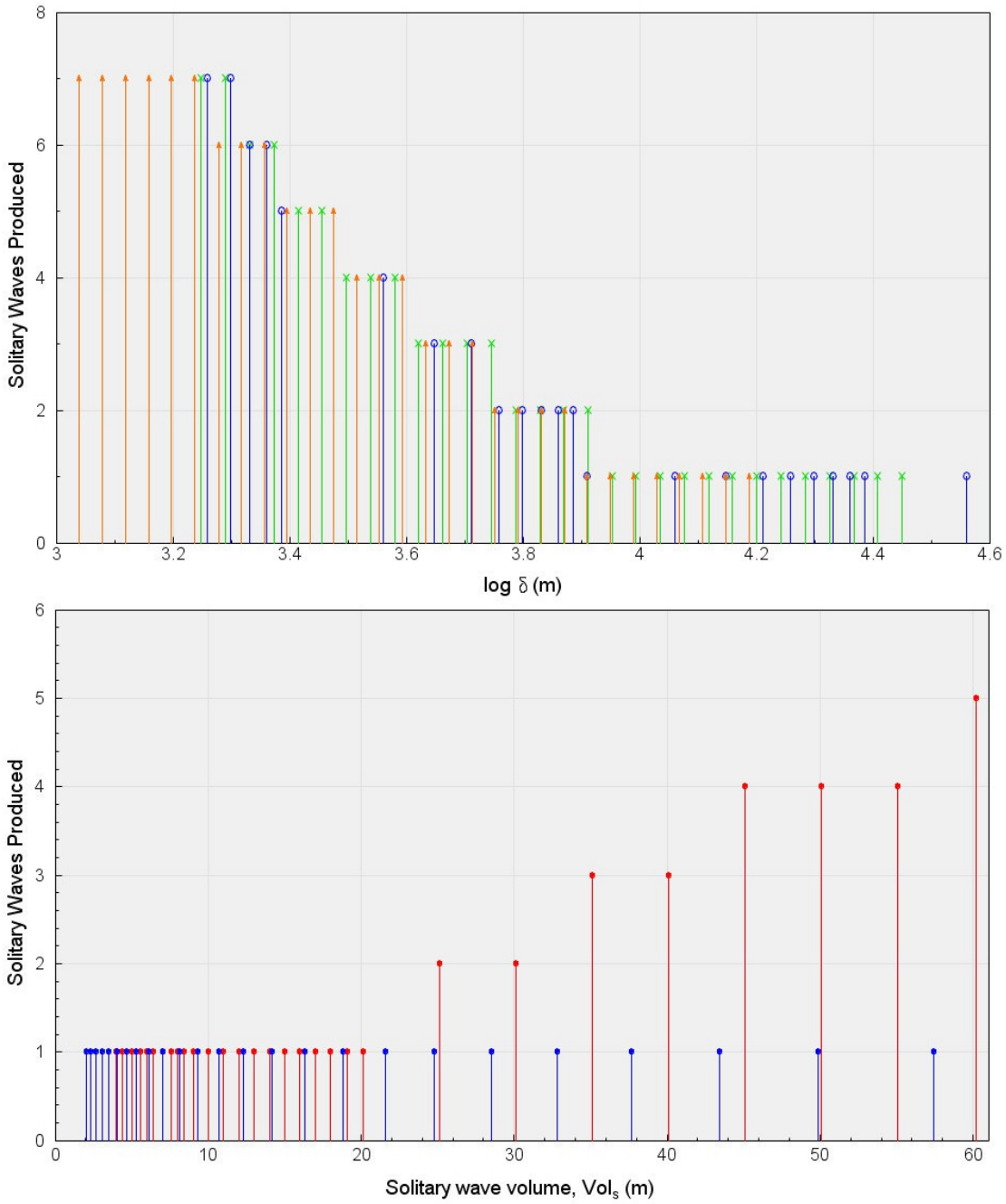


*Figure 31: (a) Solitary wave train length for variation in the fluid viscosities (green bars), matrix viscosity (blue bars) and permeability (orange bars). The x scale is in terms of log melt fraction independent compaction length (log(δ), Equation 2.54). (b) Solitary wave train length for changes in the amplitude (blue bars) and the width (red bars) of the initial perturbation. A maximum of 7 waves were counted in each experiment.*

To further analyse these secondary solitary waves I extended the least squares fitting algorithm to include secondary solitary waves and determine the Gaussian parameters of each component solitary wave after it had stabilised. In Figure 32 I show how the wave volumes vary for a series of experiments in which the width of the initial Gaussian perturbation is changed, and examine the constituents of the resulting wave trains.

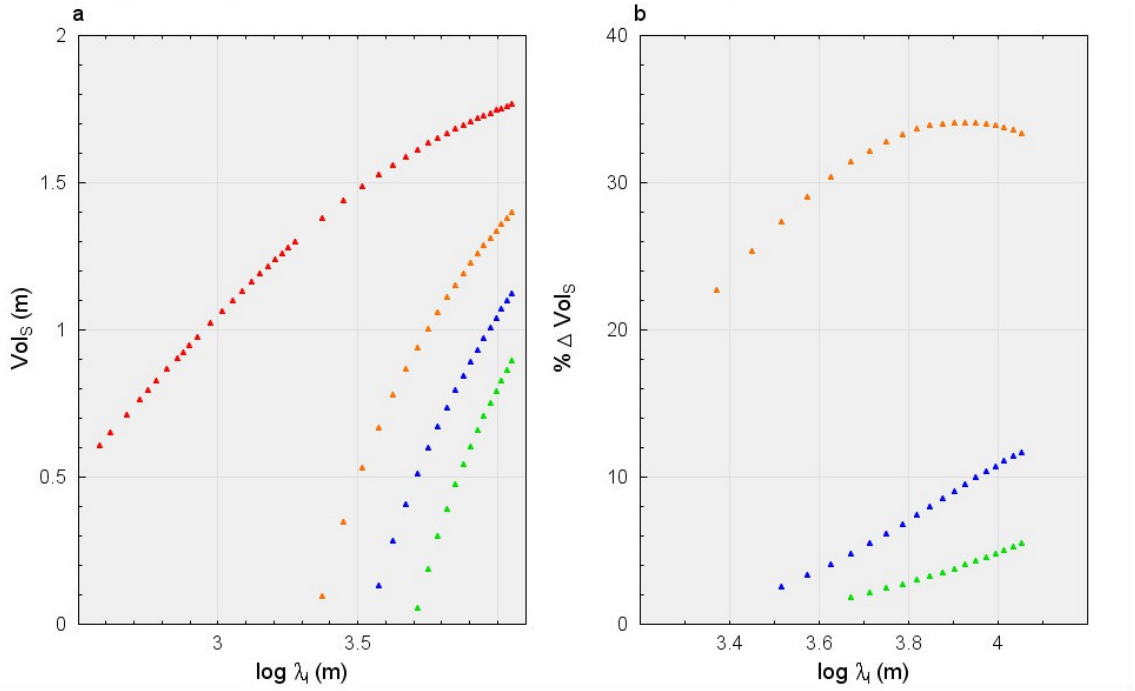


*Figure 32: (a) Stable waveform volumes (Vol$_s$) vs the initial perturbation width for solitary wave trains that evolve from an initial Gaussian distribution. The width of the initial perturbation (defined by equation 3.10) is varied between 160m and 4.8 km, all other parameters defined in Table 1. Colour indicates the successive waves: first (red), second (orange), third (blue) and fourth (green) solitary waves. (b) The volume of each solitary wave (Vol$_s$) as a percentage of the previous rank wave, where orange is used for second wave volume as percentage of the first, blue for third relative to second and green for fourth relative to third.*

As the width of the original melt region is increased, each wave packet increases in volume. For small initial widths there are no secondary waves until a critical width is reached as shown in Figure 32a at, 2.35km for the second solitary wave, 3.30km for the third and 3.77 km for the fourth. The proportion of the original melt that goes into the secondary waves increases with initial width, as more and larger secondary waves form behind the primary. Whether primary or later, the behaviour of each magmatic pulse is determined primarily by its amplitude, while the volume and number of successive pulses is determined by how much larger the initial distribution width is compared to the medium's "ideal" solitary wave width. For the parameters used in Figure 32, this

ideal solitary wave width is $\lambda_s$ = 1.78 km.

To investigate the effects of the width and δ on the number of solitary waves generated I repeated the experiment shown in Figure 32 with a different value for the permeability constant. For each experiment all other constants remained the same. As the permeability was decreased (corresponding with a decrease in δ) the number of solitary waves increases as predicted by Figure 31. The primary solitary wave volume decreases with additional secondary solitary waves, the original volume being partitioned over greater numbers of waves with increases in δ and initial width (only the first four waves are shown in Figure 31, more do exist in some cases).

As the solitary wave train is extended, the volume and shape of the leading solitary waves become increasingly similar. This convergence is demonstrated in its final state by Spiegelman (1993b) who produces a train of solitary waves from an initial melt fraction distribution in the form of a sigmoid function:

$$\varphi_{(z)} = \varphi_0 + \frac{A}{1 + e^{\sigma z - d_z}} \tag{3.49}$$

where σ is the width of the sigmoid step, $A+\varphi_0$ is maximum value of the function and $\varphi_0$ is the minimum value, $d_z$ is the location of the transition from high to low melt fraction. With this initial distribution, a series of solitary waves form each of the same volume and shape at regular intervals as the melt region is depleted by the series of waves.

To further examine the formation of secondary solitary waves I investigate how varying the permeability as well as the width of the initial perturbation impacts the number and size of the waves in the wave train. These calculations examined the width range of $\lambda_I$ = 376.8 to 11300m for permeabilities in the range of $k_0$=9.9x10$^{-7}$ to 3.3x10$^{-9}$m$^2$ for the first four waves in each wave train. The small scale melt fraction disturbance show in Figure 20, whose amplitude is proportional to the permeability constant, is ignored here. Figure 33 shows the variation of primary solitary wave width arising from perturbations of variable width for different background permeability. The width of the stable wave decreases systematically as the permeability decreases.

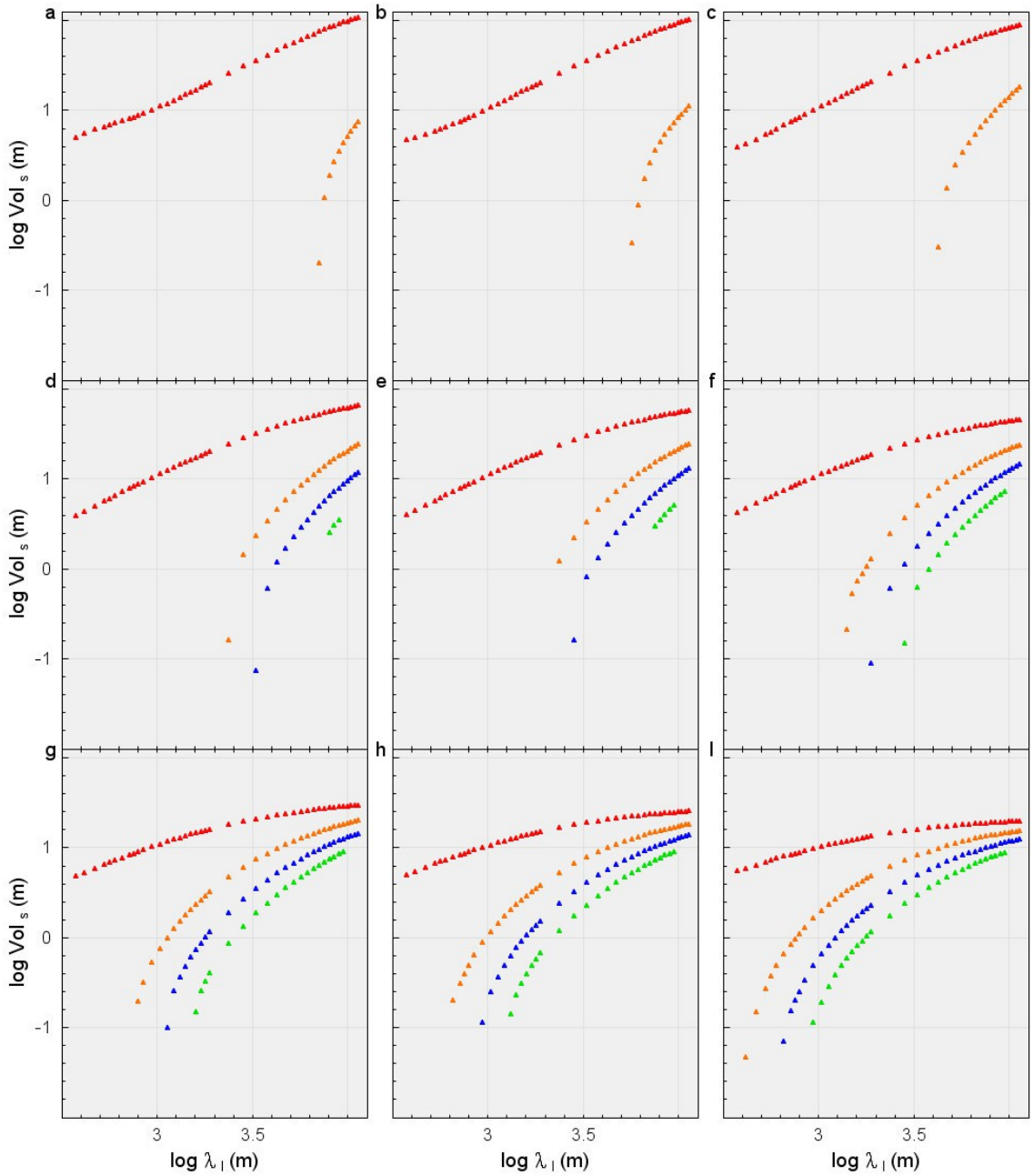


*Figure 33: Solitary wave volumes for wave trains developed from initial Gaussian perturbations (defined by equation 3.10). The width parameter of the initial perturbation ($\lambda_I$) was varied between 376.8 to 11300m each experiment. The permeability constant ($k_0$) was changed between each of experiments where $k_0=9.9x10^{-7}$ for (a), $6.6x10^{-7}$ for (b), $3.3x10^{-7}$ for (c), $9.9x10^{-8}$ for (d), $6.6x10^{-8}$ for (e), $3.3x10^{-8}$ for (f), $9.9x10^{-9}$ for (g), $6.6x10^{-9}$ for (h) and $3.3x10^{-9}$ for (I). All other parameters are as defined in Table 1. Red represents the primary solitary wave, orange the second, blue the third and green the fourth. Fifth and greater solitary waves are not shown.*

## 3.5 Solitary waves in the context of Earth processes

The existence of solitary wave trains (Figure 22) implies a possible deep control on the periodicity of surface volcanism. Formation of a solitary wave train from a zone of active partial melt generation has been demonstrated by Scott and Stevenson (1984). The trains of solitary waves I have studied consist of a series of waves at intervals governed by the relative phase velocity of each solitary wave, expressed as:

$$\Delta t = \frac{b}{\omega_{n+1}} - \frac{b}{\omega_n} \tag{3.50}$$

where $\Delta t$ is the time between arrivals of wave $n$ and $n$+1, $b$ is the depth of solitary wave formation and $\omega$ is the solitary wave phase velocity of pulse $n$ in the train.

In this mechanism the majority of melt would arrive at the base of a volcanic system in pulses rather than by percolation of melt at a constant rate.

Based on my calculations of solitary wave velocities, amplitudes and widths (Figures 23 and 24) and equation 3.50 I can calculate the range of time periods between episodes of increased volcanic activity. The width of the initial perturbation has already been demonstrated to be one of two controlling factors on the generation of solitary wave trains. In the Earth this width is analogous to the width of the melting zone, which for n-type MORB (Mid-ocean ridge basalt depleted in light rare earth elements) is geochemically estimated by McKenzie and O'Nions (1991) to be ~9km at a depth of ~80km. Using $b$=80km and $\lambda_I$=9km with the parameters from Table 1, a train of solitary waves is created (Figure 32). Applying equation 3.50 gives the interval of 3160 years between the 1st and 2nd, and 3200 years between the 2nd and 3rd arrivals. The difference between sequential arrivals remains small compared to the value of $\Delta t$ for both larger and smaller $\lambda_I$, as shown in Table 4. Solitary wave velocity however is sensitive to the parameters governing the region, as Figure 29 demonstrates, such that increasing the matrix viscosity from $1.2 \times 10^{16}$Pas to $1.2 \times 10^{17}$Pas for example changes the arrival time for the above example to 24600 years between the 1st and 2nd pulse, and 9450 years between the 2nd and 3rd pulse. For the ranges of matrix viscosity, fluid viscosity and permeability I have studied in section 3.3.2, $\Delta t$ is on the order $10^3$ to $10^5$ years.

| Initial width | $\Delta t$ between wave 1 and 2 | $\Delta t$ between wave 2 and 3 |
|---|---|---|
| 7km | 4130 yr | 4030 yr |
| 8km | 3560 yr | 3680 yr |
| 9km | 3160 yr | 3200 yr |
| 10km | 2670 yr | 2780 yr |
| 11km | 2470 yr | 2440 yr |

*Table 4 Time between surface arrival of successive waves (Δt) for the first three waves in a wave train. Arrival times were calculated from the phase velocity using equation 3.50 and b=80km for solitary waves that developed from an initial perturbation with the stated initial width (column 1) and all other constants as listed in table 1.*

To investigate the application of these time scales to the Earth I consulted the Smithsonian Volcanic Catalogue which provides historical eruption dates for many volcanoes from many different sources. I concentrated my investigation on Icelandic volcanoes instead of those of Afar, as Iceland has far more data on eruptive history from written records, geochronology and ice-cores. I produced plots of volcanic eruptions going back ~10000 years for the more well documented volcanoes in Iceland (Siebert and Simkin, 2002), but the number of eruptions show no discernible periodicity on the time-scales in question (~3000 years). The absence of a clear signal however may depend to some extent on the patchy nature of eruptive history data; recorded history, is far too short to accurately document the relevant proposed time scales of volcanic activity mediated by solitary wave arrivals.

The eruptive volume of an active volcanic complex provides another constraint. The volcano Krafla in Iceland alone produced $4.9 \times 10^8 m^3$ of erupted material during historical time (Siebert and Simkin, 2002). In three-dimensions solitary waves are likely to be spherical as demonstrated by Wiggins and Spiegelman, 1995. To simplify the comparison I assume that the one-dimensional volumes in Figure 25 are representative of a cross section through a spherical three-dimensional solitary wave in order to calculate a three-dimensional volume. Using equation 3.45 and the equation for a sphere, the volume of melt contained in a three-dimensional solitary wave can be calculated. The largest solitary wave I have studied in Chapter 3 has a melt volume of

$5.7x10^7m^3$ (Figure 23). To investigate larger volume solitary waves I ran five calculations with initial perturbation widths of 9km and peak melt fraction ($A_I$) of 7-11% to investigate the volumes generated. These experiments generated a train of solitary waves with primary solitary wave volumes between $3.8x10^8m^3$ and $2.1x10^9m^3$ for initial peak amplitudes between 7% and 11% respectively. These volumes fall within the bounds required to feed the recorded erupted volume of Krafla, supporting the argument that the solitary waves do not correspond to individual eruptions, but to periodic increases in volcanic activity on time scales of thousands of years.

## 3.6 Chapter summary

In this section, I summarise the experiments, solutions and discussion of one-dimensional numerical investigations into the two-phase fluid problem outlined in Chapter 2. To investigate the formation of solitary waves, a numerical program (1D2PF) was created to solve the one-dimensional two-phase fluid problem. 1D2PF uses a tridiagonal matrix solver along with a wave fitting algorithm to both simulate solitary wave evolution and examine the properties of the waves. These solutions were generated for a reference case defined by the constants specified in Table 1, then one constant at a time was varied across a pre-defined range and the parameters of solitary wave width, amplitude and velocity were calculated.

Firstly I varied the initial distribution of melt fraction, specifically the width and amplitude of the initial Gaussian perturbation ($A_I$ and $\sigma_I$ in equation 3.10). I showed that the amplitude ($A_S$) and phase velocity ($\omega_S$) of the solitary wave is a linear monotonic function of $A_I$, which supports the results of Barcilon and Richter (1986) who show that solitary wave velocity is a function of $A_S$. Building on this I moved on to examine the role of the initial perturbation width ($\lambda_I$, a function of $\sigma_I$, see equation 3.23) in the evolution of the solitary waves. The width of the initial perturbation is a controlling factor for the number of solitary waves that form from the initial perturbation, with larger initial widths producing a longer wave train consisting of more pulses. The initial amplitude does not influence the number waves in a train (Figure 31), only their amplitudes. Variation of $\lambda_I$ also shows a minimum width of stable solitary waves (Figure 23b) that also depends on the permeability (Figure 30). This minimum width soliton is produced for the same parameters that mark the transition from a single solitary wave to

a wave train.

I next investigated the dependence of the solitary wave width and amplitude on the permeability constant ($k_0$), fluid viscosity ($\eta_f$) and matrix viscosity ($\eta_m$), which together define the "melt fraction independent compaction length" of the medium ($\delta$, Equation 2.54). By varying these three parameters independently I have shown that $\delta$ is the primary variable that determines the solitary wave width and amplitude according to:

$$A_S \simeq 89/\delta \tag{3.47}$$

for the wave amplitude (using the slope of Figure 29a) and:

$$\lambda_S \simeq 4.6\,\delta \tag{3.46}$$

for the wave width (using the slope of Figure 29b).

The amplitude of the primary solitary wave is approximately inversely proportional to $\delta$, which implies an almost inverse relationship between $A_s$ and $\lambda_s$, when either permeability, matrix or fluid viscosity is altered.

The phase velocity however is a more complex property, demonstrating the relation:

$$\omega_s \approx C_1 \delta^{16/9} (\eta_m)^{-1} \tag{3.48}$$

which I determined from Figure 29c (Note that $\delta$ also depends on $\eta_m$). The $C_1$ term is a constant that depends on other parameters (including initial amplitude).

Finally I investigated the formation of solitary wave trains. Figure 31 shows clearly that the number of solitary waves is directly related to the initial perturbation width as well as the melt fraction independent compaction length. I have demonstrated that as $\delta$ is decreased or $\lambda_I$ is increased the number of solitary waves in the resulting wave train increases. Further experiments in which the permeability constant, and thus the melt-independent compaction length, is changed indicates that as the number of solitary waves in a train rises, the volumes of the solitary waves become closer to each other. This behaviour is consistent with experiments by Spiegelman (1993b) who used a sigmoid step function to produce a train of regular solitary waves of identical width and amplitude.

The interval between arrival of each solitary wave train at the surface can be expressed as:

$$\Delta t = \frac{b}{\omega_{n+1}} - \frac{b}{\omega_n} \tag{3.50}$$

where $\Delta t$ is time lag between successive arrival of wave $n$ and $n$+1, $b$ is the origin of the solitary waves and ω is the solitary wave phase velocity for the respective pulse.

Using computed solitary wave velocities, amplitudes and widths (Figures 23 and 24) with equation 3.50 and $b$=80km and $\lambda_l$=9km, the depth and width of the melting region for n-type MORB given by McKenzie and O'Nions (1991), $\Delta t$ can be calculated for Earth like parameters. With the parameters from Table 1, equation 3.50 gives the interval of 3160 years between the 1st and 2nd, and 3200 years between the 2nd and 3rd arrivals. The difference between sequential arrivals remains small compared to the value of $\Delta t$ for both larger and smaller $\lambda_l$, as shown in Table 4.

I consulted the Smithsonian Volcanic Catalogue to investigate if periodic increases in volcanic activity on these time scales have been observed. For the more well documented Icelandic volcanoes, plots of volcanic eruptions going back ~10000 years (Siebert and Simkin, 2002) showed no discernible increase in eruptivity on the time-scales in question (~3000 years). However the completeness of the record is questionable for eruptions that occurred more than ~1000 years ago due to lack of historical records.

I finally examined the melt volume contained in solitary waves by assuming that the one-dimensional volumes are cross sections of three-dimensional spherical waves like those shown by Wiggins and Spiegelman (1995). Experiments with initial perturbation widths of 9km and peak melt fraction ($A_l$) of 7-11% produced wave trains with a three-dimensional melt volumes between $3.8 \times 10^8$ m$^3$ and $2.1 \times 10^9$m$^3$ for the primary solitary waves. The volcano Krafla in Iceland alone produced $4.9 \times 10^8$m$^3$ of erupted material during historical time (Siebert and Simkin 2002), demonstrating that solitary waves can provide the volume of melt needed for an extended volcanic history.

# 4 Three-dimensional Numerical Model

## *4.1 TDCON and TD2PF*

### 4.1.1 Introduction

TDCON is a thermal convection program written by Greg Houseman in 1984 for specific application to the problem of thermal convection in the Earth's mantle. The program was initially written for a vector processor but was later modified to run as a parallel program on a multi-processor cluster. It has been subsequently used on many different systems. The code depends on a three-dimensional Poisson solver called TDPOIS (Houseman, 1987), which is described in detail in section 4.3.

From a defined initial distribution of temperature TDCON calculates the velocity field using the vector potential formulation, and advances the temperature field with discrete time steps. Numerical solutions obtained using TDCON have been used to study the topography of a dense layer at the base of the mantle (Youngs and Houseman, 2009; Youngs, 2007), mixing of the Earth's mantle (Schmalzl et al., 1996) and the thermal structure of mantle plumes (Houseman, 1990). Converting TDCON to model two-phase flows, representing the compaction of viscous permeable matrix, however, represents a major development of the program, and as such has presented unique challenges.
The adapted version of TDCON (three-dimensional convection) is designated TD2PF (three-dimensional two-phase flow) in order to facilitate comparison of the methods used in the two programs. Two major differences arise between TDCON (mantle convection) and TD2PF (movement of melt within a deformable permeable matrix). Firstly, the velocity field that describes the deformable matrix in TD2PF is compressible. Therefore, TD2PF requires that the scalar potential field $B$ (equation 2.1) is computed at every time-step, whereas $B=0$ everywhere for TDCON, and need not be computed.

Secondly, in TD2PF a time-stepping algorithm is used to study the evolution of the melt fraction φ in time and space; in TDCON the time-stepping algorithm is used to study the evolution of the temperature field *T*. A fundamental difference between the two problems is that diffusion of the temperature field is caused by thermal conduction (TDCON), but no corresponding process acts on the melt fraction field φ in TD2PF. In principle, φ evolves purely in response to advection by the flow field represented using Helmholtz potentials, $\boldsymbol{V} = \nabla\times\boldsymbol{A} + \nabla B$.

As TD2PF is derived by modification of the structures and processes used in TDCON it is worthwhile to briefly summarize the TDCON algorithm.

### 4.1.2 The of TDCON algorithm

TDCON (Houseman, 1990) uses a set of mathematical equations analogous to, but simpler than, those required for the melt migration problem (sections 2.5.1 to 2.5.3). Conservation of mass for a single-phase incompressible flow (part of equation 2.2), is:

$$\nabla\cdot\boldsymbol{V} = 0 \tag{4.1}$$

The zero divergence condition requires that $B=0$ and $V=\nabla\times\boldsymbol{A}$ (equation 2.1).

The single-phase conservation of momentum for a constant viscosity fluid (the Boussinesq approximation) is:

$$\eta\nabla^2\boldsymbol{V} - \nabla P + \rho(1-\alpha T)g\boldsymbol{k} = 0 \tag{4.2}$$

where $T$ is the temperature, $\alpha$ is the thermal expansivity of the fluid, and ρ is its density. Equation 4.2 is comparable to equation 2.4, with the first term representing viscous stress, the second term internal pressure gradients, and the last term the buoyancy forces arising from thermal expansion. The driving forces in equation 4.2 contrast with those of equation 2.4 in which the difference in density between fluid and matrix phases, combined with the spatial variability of the melt fraction, drives the flow.

Finally, TDCON uses the principle of conservation of energy, to determine the evolution of the temperature field:

$$\frac{DT}{Dt} = \kappa\nabla^2 T + \frac{H_v}{\rho c_p} \tag{4.3}$$

where $H_v$ is rate per unit volume of internal heating, $c_p$ is specific heat capacity and κ is the thermal diffusivity.

Taking the curl of equation 4.2 and using an appropriate non-dimensionalisation ($d$, the layer thickness for the length scale, and $d^2/\kappa$ for the time scale), obtaining:

$$\nabla^4 \boldsymbol{A} = Ra \nabla \times [T \hat{\boldsymbol{k}}] \tag{4.4}$$

where:

$$Ra = \frac{\rho g \alpha \Delta T d^3}{\eta \kappa} \tag{4.5}$$

The pressure field can also be calculated using:

$$\nabla^2 P = Ra \frac{\partial}{\partial z}[T] \tag{4.6}$$

and the dimensionless energy equation (equation 4.3) becomes:

$$\frac{\partial T}{\partial t} = \nabla^2 T - \boldsymbol{V} \cdot \nabla T + H \tag{4.7}$$

where:

$$H = \frac{H_v d^2}{\rho C_p \kappa \Delta T} \tag{4.8}$$

At a given time level, the velocity field (represented by the components of $\boldsymbol{A}$) is obtained from the temperature field by inverting equation 4.4. The temperature field is then updated using the discretised version of equation 4.7.

The structural similarity between the thermal convection problem and the melt migration problem thus led to the strategy to adapt the TDCON program in order to develop TD2PF.

### 4.1.3 Program map

The basic organisation of the TDCON program is summarised in the program map shown in Figure 34.

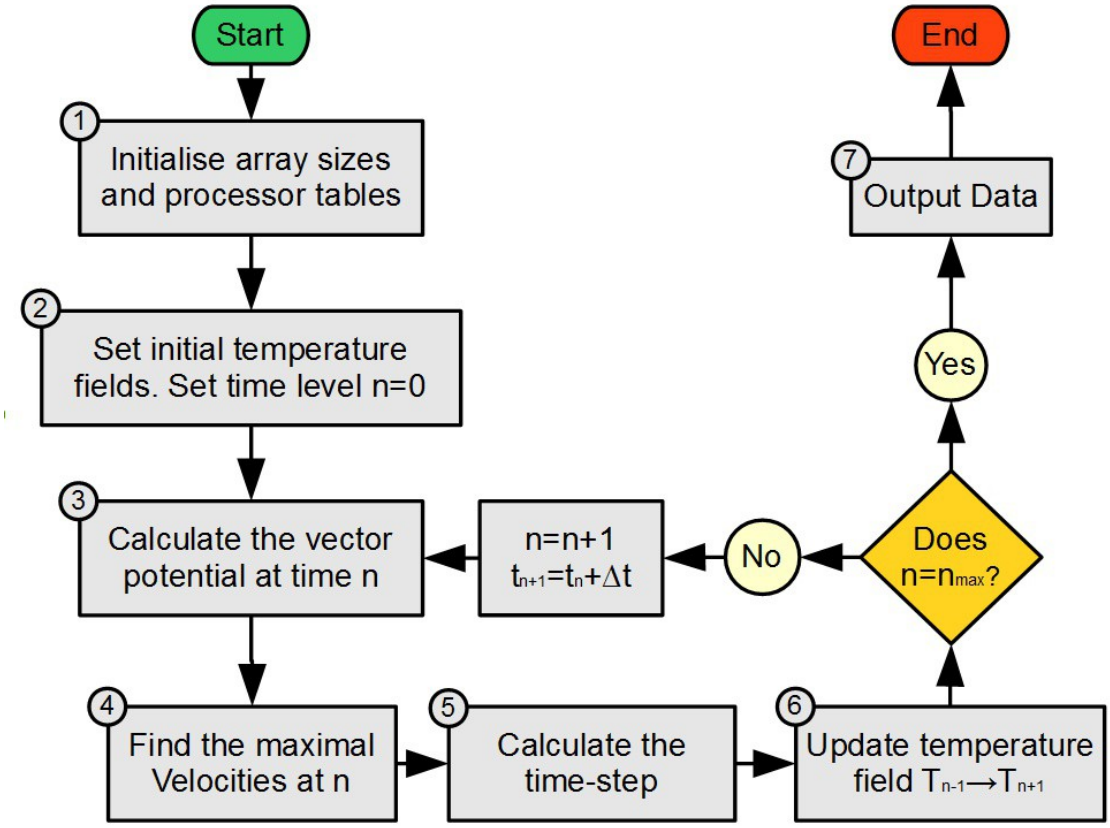


*Figure 34: Flow chart of the three-dimensional thermal convection program, TDCON. Time and temperature fields are incremented in steps until the solution reaches a prescribed end time $t_{max}$ or number of steps $n_{max}$.*

Each operation in Figure 34 depends on multiple subroutines and processes, especially in the parallel version of TDCON. In the following sections I will describe the most important of these processes in more detail.

### 4.1.1 The finite difference mesh and parallelisation

The solution method for the biharmonic equation 4.4 depends on the efficient use of the Fast Fourier Transform in the two horizontal directions. To optimise that procedure, the mesh dimensions in *x*, *y* and *z* directions are restricted to values:

$$NX1 = 2^{IQX} + 1 \quad , \quad NY1 = 2^{IQY} + 1 \quad \& \quad NZ1 = 2^{IQZ} + 1 \tag{4.9}$$

where *IQX*, *IQY* and *IQZ* are integers defined in the program at compilation. The dimensionless layer thickness is 1, so the interval between mesh points in the vertical direction is:

$$\Delta z = \frac{1}{(NZ1 - 1)} \tag{4.10}$$

By default, the same mesh interval is used in the horizontal directions unless a separate scale factor of *DXP*, or *DYP* is defined to differ from 1.

The strategy for parallelising TDCON is to cut the rectangular prism using two sets of parallel planes, as shown in Figure 35. Each of the blocks thus produced is operated on by an independent processor. The nature of the different operations that are carried out in each time-step requires however that this parallelisation must be done in three different ways, parallel to the *x* direction, *y* direction or *z* direction. At different times in the calculation the data are re-organized across processors to enable parallel operations to occur in the *x*, *y* or *z* direction respectively.

This parallelisation, originally implemented by S. Borthwick, is complex but the sharing of the workload allows for a much faster solution than would be possible with any serial code and allows larger and denser arrays of points to be used.

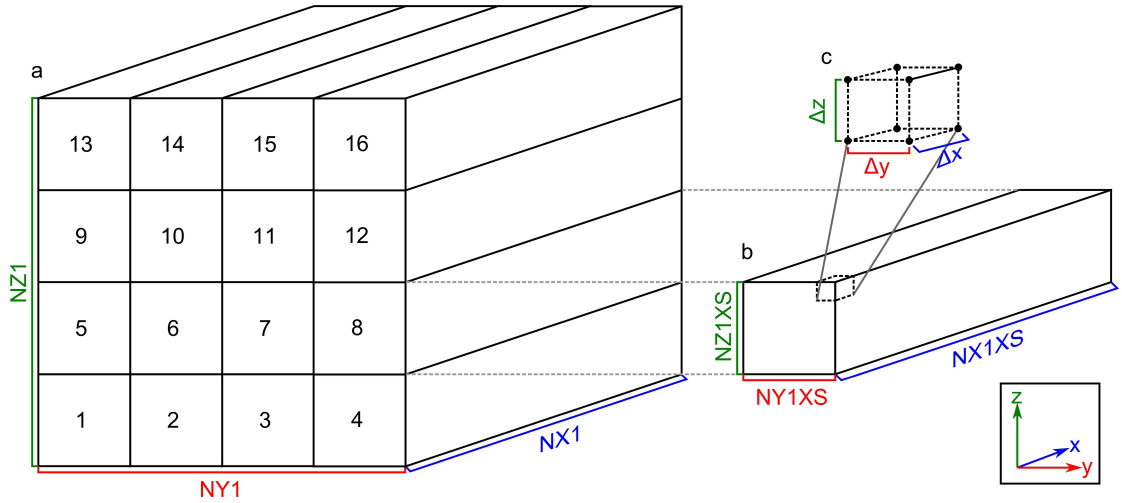


*Figure 35: How the three-dimensional rectangular array is split up for parallelisation in the programs TDCON and TD2PF. The data is split over multiple equivalent blocks, each assigned to a separate processor (a), (b) shows the relation between the unit computational element (c) of dimensions $\Delta x \times \Delta y \times \Delta z$.*

### 4.1.2 Initial temperature fields at time *n*=0 and *n*=-1

An initial temperature field must be defined at time zero. The specification of this field depends on the physical problem, but in general it is based on a small number of parameters read from an input file and has a simple functional dependence on *x*, *y* or *z* if necessary perturbed by a signal comprised of multiple harmonics with regular or random phase and amplitude, which can be used to initiate convection systems with a random flow element.

Because the time-stepping algorithm is centred on the current time level $t_n$, it uses $T_{n-1}$ and $T_n$ to compute the updated temperature field $T_{n+1}$. Therefore, the temperature field initialisation requires that $T_{-1}$ and $T_0$ are defined. During the course of the calculation temperatures are successively updated at odd and then even time levels.

### 4.1.3 Calculate the vector potential at time *n*

For homogeneous boundary conditions, Equation 4.4 reduces to a partial differential equation with only *x* and *y* components:

$$\nabla^4 A_x \hat{\boldsymbol{i}} + \nabla^4 A_y \hat{\boldsymbol{j}} = Ra\left[\frac{\partial T}{\partial y}\hat{\boldsymbol{i}} - \frac{\partial T}{\partial x}\hat{\boldsymbol{j}}\right] \tag{4.11}$$

The discretised (4.4) may be written using the temperature field at time level *n*:

$$\nabla^4 A_x = Ra \frac{T_{i,j+1,k} - T_{i,j-1,k}}{2\Delta y} \tag{4.12}$$

$$\nabla^4 A_y = -Ra \frac{T_{i+1,j,k} - T_{i-1,j,k}}{2\Delta x} \tag{4.13}$$

Equations 4.12 and 4.13 are successively solved using the boundary conditions for $A$ stated in section 4.2.3. The biharmonic operator is inverted using the subroutine TDPOIS (Houseman, 1990) to find the values of $A_x$ and $A_y$. TDPOIS is an integral part of TDCON and is discussed in section 4.3.

### 4.1.4 Stability criteria for time-step size

TDCON uses the maximum value of $\boldsymbol{V}$ (using equation 2.1) to ascertain how quickly the system is evolving. It uses this value to determine the time-step size needed to prevent discretisation errors from producing numerical instability.

The main constraint on the time-step comes from the velocity field, requiring that the time-step is never large enough to advect further than Δx, Δy or $\Delta z$ in one time-step. This produces the following relation as stated by Youngs (2007, p92):

$$\Delta t^n + \Delta t^{n+1} \leq \frac{11}{4}\left[ max\left( \frac{|u|}{\Delta x} + \frac{|v|}{\Delta y} + \frac{|w|}{\Delta z} \right) \right]^{-1} \tag{4.14}$$

where $u$, $v$ and $w$ are the $x$, $y$ and $z$ components of the velocity field. Typically equation 4.14 provides the effective upper limit on the time-step size in TDCON. TDCON uses a second condition based on a diffusion stability criteria (from Roache, 1972, p.53), however there are no diffusion terms in the TD2PF algorithm so this term is not relevant to TD2PF.

There is also need for a time step smoothing operation to prevent oscillation in the size of the time-step (Youngs, 2007, p93), simply:

$$\Delta t^{n+1} = \frac{\Delta t^n + \Delta t^{n+1}}{2} \quad \text{if} \quad \Delta t^{n+1} \geq \Delta t^n \tag{4.15}$$

### 4.1.5 Time-stepping the temperature field

The temperature field is advanced from time level $n$ to $n$+1 using the discretised form of equation 4.7. For second-order accuracy, TDCON uses the time-centred approximation to the time derivative:

$$\frac{\partial T}{\partial t}=\frac{T_{i,j,k}^{n+1}-T_{i,j,k}^{n-1}}{2\Delta t} \tag{4.16}$$

$\nabla^2 T$ is represented using the average of centred time and forward time difference operators (4.14, 4.15) is as follows:

$$\nabla^2 T=\frac{1}{2}\left[(\nabla^2 T)^{n-1}+(\nabla^2 T)^{n}\right] \tag{4.17}$$

where $n$ is the current time-step. The spatial operator $\nabla^2 T$ uses the centred finite difference approximation at $n$-1:

$$(\nabla^2 T)^{n-1}=\frac{T_{i+1}^{n-1}-2T^{n-1}+T_{i+1}^{n-1}}{\Delta x^2}+\frac{T_{j+1}^{n-1}-2T^{n-1}+T_{j+1}^{n-1}}{\Delta y^2}+\frac{T_{k+1}^{n-1}-2T^{n-1}+T_{k+1}^{n-1}}{\Delta z^2} \tag{4.18}$$

The space-centred advection terms of equation 4.7 are evaluated at time level $n$:

$$\begin{aligned}(-\boldsymbol{V}.\nabla[T])^{n}=&\frac{(V_x T)_{i+1,j,k}^{n}-(V_x T)_{i-1,j,k}^{n}}{2\Delta x}\\ &+\frac{(V_y T)_{i,j+1,k}^{n}-(V_y T)_{i,j-1,k}^{n}}{2\Delta y}+\frac{(V_z T)_{i,j,k+1}^{n}-(V_z T)_{i,j,k-1}^{n}}{2\Delta z}\end{aligned} \tag{4.19}$$

The final term in equation 4.7 is simply a constant. Using equations (4.17) and (4.19) the temperature at time $n$+1 can be calculated using:

$$T^{n+1}=T^{n-1}+(\Delta t^{n}+\Delta t^{n+1})\left[\frac{1}{2}((\nabla^2 T)^{n-1}+(\nabla^2 T)^{n})-(\boldsymbol{V}\cdot\nabla[T])^{n}+H^{n}\right] \tag{4.20}$$

Replacing the stored values of $T_{n-1}$ with those of $T_{n+1}$. At the next time-step $T_n$ is replaced by the $T$ field computed at time level $n$+2. The method requires temperature fields to be stored in the computer's memory for the previous two time steps, and therefore is quite memory-intensive.

Spatial boundary conditions are also required for the temperature field. On the side boundaries, the normal gradient is generally set to zero, as if the boundary were a reflecting surface. On the upper and lower boundaries, either a constant temperature or a constant normal gradient of temperature (constant heat flux) is set. For the purpose of

representing the advection (4.19) and diffusion terms, these conditions provide values for the temperature field just outside the bounding surface.

## *4.2 Three-dimensional numerical models*

### 4.2.1 Introduction

Three-dimensional numerical modelling has become more common in recent years with increases in computer power now allowing solution of relatively complex three-dimensional problems within a reasonable length of computing time.

An important development in recent years which has enabled these computationally intensive three-dimensional numerical models to be developed is the expansion of cluster computing using parallel processing. In this case, the computational process is split across multiple processors, all working simultaneously to solve parts of the same problem.

To date, relatively few three-dimensional models of the magma matrix two-phase system have been developed. However, Wiggins and Spiegelman (1995) demonstrated that a three-dimensional solution is possible and that solitary waves exist in such a numerical solution. The same authors also demonstrated that the solitary waves discussed in chapter 3 are unstable in a three-dimensional model, destabilising and forming into spherical solitary waves. However, the system of equations they used in that paper are heavily simplified and they provide little detail on their method. There is therefore much scope for obtaining new insight into the dynamic process of melt extraction by the development of a three-dimensional algorithm for solution of this problem.

### 4.2.2 Mathematics for three-dimensional model

The three-dimensional model involves significantly more complexity than the one-dimensional model. For a start, I use the potential function formulation 2.1 to represent the matrix velocity field $\boldsymbol{V}$. One advantage of the potential function formulation is that it provides a natural separation of the velocity field into compressible ($\nabla B$) and incompressible ($\nabla \times \boldsymbol{A}$) components. The divergence $D = \nabla^2 B$ (equation 2.9) is obtained

by solution of equation 2.65 and then simply inverted to obtain *B*. The vector potential components $\boldsymbol{A}$ are obtained from the inversion of equation 2.61. The velocity field is thus defined at a given time step by equation 2.1, and determined completely by the current distribution of melt fraction φ. The whole solution is advanced in time using a discretised version of equation 2.66 to construct a time-stepping algorithm which updates φ based on the current $\boldsymbol{A}$ and *B* fields.

### 4.2.3 Boundary conditions

The construction of boundary conditions to solve the potential function equations (2.65, 2.9, 2.61) in three dimensions is based on the same principles as those used for the one-dimensional program in section 3.2.2. Boundary conditions on $\boldsymbol{V}$ however must be replaced with equivalent conditions on *D*, *B* and $\boldsymbol{A}$ and additional conditions are needed in the x and y directions.

Consider first the boundary conditions that apply in the z (vertical) direction as stated in section 3.2.2. I assume that the divergence of the matrix is zero at the top of the layer (equation 3.9):

$$D_{z=h_z}=0 \tag{4.21}$$

Here *z* is positive upwards, with $z=0$ being the base of the modelled region and $h_z$ being the top (changed from *h*, as this is now a system of three dimensions). To obtain the boundary condition for *D* on $z=0$ equation 2.30 can be used, noting that $\boldsymbol{V}=\boldsymbol{u}=0$ on the lower boundary:

$$\nabla^2[\boldsymbol{V}]+\nabla\left[\left(\frac{1}{\varphi}-\frac{2}{3}\right)\nabla\cdot[\boldsymbol{V}]\right]+(1-\varphi)\Delta\rho\,\frac{g}{\eta_m}\hat{\boldsymbol{k}}=0 \tag{4.22}$$

Substituting for the potential functions, and using identity 2.12 and the chain rule:

$$-\nabla\times[\nabla\times[\nabla\times[\boldsymbol{A}]]]+D\nabla\left[\frac{1}{\varphi}\right]+\left(\frac{1}{\varphi}+\frac{1}{3}\right)\nabla D+(1-\varphi)\Delta\rho\,\frac{g}{\eta_m}\hat{\boldsymbol{k}}=0 \tag{4.23}$$

Thus, in dimensionless units (section 2.5):

$$\nabla D=\left(\frac{3\varphi}{3+\varphi}\right)\left(\nabla\times[\nabla\times[\nabla\times[\vec{\boldsymbol{A}}]]]-\nabla\left[\varphi^{-1}\right]D-(1-\varphi)\hat{\boldsymbol{k}}\right) \tag{4.24}$$

On the $z$=0 boundary only the z-component of 4.24 is needed:

$$\partial_z D = \left(\frac{3\varphi}{3+\varphi}\right)\left(\frac{\partial}{\partial y}[\nabla^2 A_x] - \frac{\partial}{\partial x}[\nabla^2 A_y] - D\frac{\partial}{\partial z}[\varphi^{-1}] - (1-\varphi)\right) \tag{4.25}$$

This boundary condition is applied iteratively alongside equation 2.65 due to the term that includes $D$ on the right hand side of equation 4.25.

The three-dimensional numerical program also requires conditions on both the x and y boundaries. I assume here that each of the side boundaries: $x$=0,$h_x$, $y$=0,$h_y$ use a reflecting boundary: there is no flow normal to the boundary and no gradient of the flow parallel to the boundary. Thus:

$$\frac{\partial D}{\partial x} = 0 \quad on \quad x = 0, h_x \tag{4.26}$$

$$\frac{\partial D}{\partial y} = 0 \quad on \quad y = 0, h_y \tag{4.27}$$

Similarly:

$$\frac{\partial B}{\partial x} = 0 \quad on \quad x = 0, h_x \tag{4.28}$$

$$\frac{\partial B}{\partial y} = 0 \quad on \quad y = 0, h_y \tag{4.29}$$

And for $\boldsymbol{A}$ (Houseman, 1990):

$$\frac{\partial A_x}{\partial x} = 0 \quad on \quad x = 0, h_x \tag{4.30}$$

$$A_x = 0 \quad on \quad y = 0, h_y \tag{4.31}$$

$$A_x = 0 \quad on \quad z = 0, h_z \tag{4.32}$$

$$A_y = 0 \quad on \quad x = 0, h_x \tag{4.33}$$

$$\frac{\partial A_y}{\partial y} = 0 \quad on \quad y = 0, h_y \tag{4.34}$$

$$A_y = 0 \quad on \quad z = 0, h_z \tag{4.35}$$

To solve equation 2.9, upper and lower boundary conditions for $B$ are needed.

The condition of zero vertical velocity on the lower boundary gives:

$$\frac{\partial B}{\partial z}=0 \quad on \quad z=0 \tag{4.36}$$

On the upper boundary zero horizontal velocity is assumed, and thus $B$ = constant on $z=h_z$. The value of the constant is arbitrary and without loss of generality, it can be set as:

$$B=0 \quad on \quad z=h_z \tag{4.37}$$

completing the set of boundary conditions on all six boundaries for $D$, $B$ and $\boldsymbol{A}$.

## *4.3 TDPOIS and TDPOTS*

### 4.3.1 Introduction

TDPOIS (Three-Dimensional POIsson Solver) is an optimised subroutine used to solve the three-dimensional Poisson or biharmonic equations on a rectangular mesh. Houseman (1987) described the basic version of the routine; Houseman (1990) described a modified version, useful also for rigid boundary conditions. The purpose of this subroutine is to solve equations of the form:

$$\nabla^m[g(x,y,z)]=f(x,y,z) \tag{4.38}$$

Where $m$ is either 2 for a Poisson equation or 4 for a biharmonic equation. To solve equation 4.38, TDPOIS requires as input the array $f$ of equation 4.38, and a small set of integer values that define the boundary conditions to be applied on $x$ and $y$ surfaces. The Poisson solver uses Fourier transforms in both $x$ and $y$ directions to convert equation 4.38 into a set of one-dimensional ordinary differential equations in the $z$ direction. These are solved numerically using a cyclic reduction algorithm. For TD2PF, significant extension of TDPOIS is required. For ease of reference and distinction between the two, the resulting program has been given a different name: TDPOTS (Three-Dimensional POisson and Tridiagonal Solver).

### 4.3.2 Fourier analysis

The description here applies to the method used to solve the biharmonic equation ($m$=4) but it can be adapted for the Poisson problem with ease.

If equation 4.38 is split into two parts, the *x* component can be examined:

$$\nabla^2 \omega_x = -f_x$$
$$\nabla^2 g_x = -\omega_x \tag{4.39}$$

Reflection conditions on the side boundaries result in a mixture of Neumann and Dirichlet conditions:

$$\frac{\partial g_x}{\partial x} = \frac{\partial \omega_x}{\partial x} = 0 \quad \text{on} \quad x = h_x$$
$$\omega_x = g_x = 0 \quad \text{on} \quad y = 0, h_y \tag{4.40}$$
$$\omega_x = g_x = 0 \quad \text{on} \quad z = 0, h_z$$

With these boundary conditions, the discretised two-dimensional Fourier representations of ω and *f* are:

$$\omega(x, y, z) = \sum_{i=0}^{NX} \sum_{j=1}^{NY} \Omega_{ij}(z) \cos\left(\frac{i\pi x}{h_x}\right) \sin\left(\frac{j\pi y}{h_y}\right) \tag{4.41}$$

$$f(x, y, z) = \sum_{i=0}^{NX} \sum_{j=1}^{NY} F_{ij}(z) \cos\left(\frac{i\pi x}{h_x}\right) \sin\left(\frac{j\pi y}{h_y}\right) \tag{4.42}$$

where:

$$\Delta x = \frac{h_x}{NX} \quad \Delta y = \frac{h_y}{NY} \quad \Delta z = \frac{h_z}{NZ} \tag{4.43}$$

The boundary conditions determine the use of cosine or sine in each direction; sine relates to a Dirichlet condition (zero value on the boundary) while cosine is for a Neumann condition (zero gradient on the boundary). If equation 4.41 and 4.42 are substituted into 4.39, each harmonic can be considered separately:

$$\frac{d^2 \Omega_{ij}(z)}{dz^2} - k^2 \Omega_{ij}(z) = -F_{ij}(z) \tag{4.44}$$

where $k^2 = \left(\frac{i\pi}{h_x}\right)^2 + \left(\frac{j\pi}{h_y}\right)^2$

Equation 4.44 can now be converted into finite difference form using the centred difference method for a second-order accurate approximation:

$$\Omega_{i,j,k-1} - \left[2 + k^2 \Delta z^2\right] \Omega_{i,j,k} + \Omega_{i,j,k+1} = -\Delta z^2 F_{i,j,k} \tag{4.45}$$

The resulting $NX \times NY$ one-dimensional equations can now be solved using a cyclic reduction algorithm, an alternative method to the tridiagonal algorithm discussed in section 3.2.4, and is more efficient and stable than the matrix equation defined by equation 4.45.

### 4.3.3 Cyclic reduction (Dirichlet)

Cyclic reduction applies to a tridiagonal matrix in which the values on the diagonals are constant along each diagonal (allowing for exceptions at top and bottom). The matrix for equation 4.45 is:

$$\begin{bmatrix} 1 & 0 & 0 & 0 & \cdots & 0 \\ 1 & -\alpha & 1 & 0 & \cdots & 0 \\ 0 & 1 & -\alpha & 1 & \cdots & 0 \\ \vdots & \ddots & \ddots & \ddots & \ddots & \vdots \\ 0 & \cdots & 1 & -\alpha & 1 & 0 \\ 0 & \cdots & 0 & 1 & -\alpha & 1 \\ 0 & \cdots & 0 & 0 & 0 & 1 \end{bmatrix} \begin{bmatrix} \Omega_0 \\ \Omega_1 \\ \Omega_2 \\ \vdots \\ \Omega_{NZ-2} \\ \Omega_{NZ-1} \\ \Omega_{NZ} \end{bmatrix} = \begin{bmatrix} 0 \\ F_1 \\ F_2 \\ \vdots \\ F_{NZ-2} \\ F_{NZ-1} \\ 0 \end{bmatrix} \tag{4.46}$$

where $\alpha = 2k^2 \Delta z^2$, and dropping the subscripts ($i$,$j$) used in the previous section for brevity. In this example, Dirichlet conditions have been applied to replace the first and last equations.

The cyclic reduction technique (Christiansen and Hockney, 1971) is a three-step process: reduction, three point solution and back-substitute. The reduction phase seeks to condense the $NZ$+1 equations in (4.46) down to three equations. At each step in the reduction every second equation is eliminated as follows; for example:

$$\Omega_{k-2} - \alpha \Omega_{k-1} + \Omega_k = -\Delta z^2 F_{k-1} \tag{4.47a}$$

$$\Omega_{k-1} - \alpha \Omega_k + \Omega_{k+1} = -\Delta z^2 F_k \tag{4.47b}$$

$$\Omega_k - \alpha \Omega_{k+1} + \Omega_{k+2} = -\Delta z^2 F_{k+1} \tag{4.47c}$$

Multiplying 4.47b by α and adding equations 4.47a and 4.47c produces:

$$\Omega_{k-2} - (\alpha^2 - 2)\Omega_k + \Omega_{k+2} = -\Delta z^2 [F_{k-1} + \alpha F_k + F_{k+1}] \tag{4.48}$$

Applying the reduction procedure to every second line of (4.46) reduces the set of equations in number to $NZ$/2+1.

The procedure is repeated at each of $r_n$ reduction cycles, re-evaluating α (equation 4.62) until only three equations remain:

$$\begin{bmatrix} 1 & 0 & 0 \\ 1 & -\alpha^{r=r_n} & 1 \\ 0 & 0 & 1 \end{bmatrix} \begin{bmatrix} \Omega_0 \\ \Omega_{NZ/2} \\ \Omega_{NZ} \end{bmatrix} = \begin{bmatrix} 0 \\ F_{NZ/2}^{r=r_n} \\ 0 \end{bmatrix} \tag{4.49}$$

The solution of (4.49) is trivial:

$$\begin{aligned} \Omega_0 &= 0 \\ \Omega_{NZ/2} &= -\frac{F_{NZ/2}^{r=r_n}}{\alpha^{r=r_n}} \\ \Omega_{NZ} &= 0 \end{aligned} \tag{4.50}$$

Back-substituting the (now known) value of $\Omega_{NZ/2}$ into the previous reduction cycles obtains the unknowns on the intermediate points $k=NZ/4$ and $3NZ/4$. Working back up the chain of reduction cycles, all other values of $\Omega_m$ are progressively found for this particular $i,j$ coordinate in the wavenumber domain. This algorithm is applied to all values of $i$ and $j$ before the inverse Fourier transform is applied to return the solved value for $\omega(x,y,z)$. To find $g(x,y,z)$ the cyclic reduction is simply applied a second time before the inverse Fourier transform is used.

### 4.3.4 Modifications to TDPOIS algorithm

As mentioned earlier, the capabilities of TDPOIS do not match the requirements for solution of equation 2.65, needed to obtain $D$, the divergence of the flow field. The simplest way to solve equation 2.65 for $D$ would be to arrange it in the manner:

$$\nabla^2 D = p - \mathbf{r} \cdot \nabla D + q^2 D \tag{4.51}$$

where primes have now been dropped for clarity. The boundary conditions for $D$ (4.21, 4.25, 4.26 and 4.27) call for the $z$=0 boundary to be a non-zero Neumann condition and $z$=1 a zero value Dirichlet condition. This set of boundary conditions is not compatible with the TDPOIS algorithm as written by (Houseman, 1987), since the subroutine that handles cyclic reduction in TDPOIS (named VCRED) can only use zero Dirichlet conditions on $z$=0,1.

VCRED is a vectorised and modified version of a subroutine named CRED originally written by Christiansen and Hockney (1971). They explained what adaptations of the methods described in section 4.3.3 are needed to implement a Neumann boundary condition on $z$=0,1, and I implemented a version of their algorithm in VCRED.

However, as discussed in section 4.4.3, this arrangement of equation 2.65 is unstable in the range of $q^2$ values I require when solved with TDPOIS using VCRED. To solve this issue, a second arrangement of equation 2.65 was proposed:

$$\nabla^2 D - q^2 D = p - \boldsymbol{r} \cdot \nabla D \tag{4.52}$$

Solution to an equation of this form is not possible with VCRED therefore such a new subroutine named VCTRI and new input structures were introduced into TDPOIS to allow it to solve using a tridiagonal matrix solver algorithm much like 1D2PF.
With these adaptations, TDPOIS was renamed to TDPOTS. In the next few sections I discuss in detail the implementation of these new algorithms and changes that reconfigured TDPOIS into TDPOTS in order to solve equations 4.51 and 4.52 with the necessary boundary conditions.

### 4.3.5 Cyclic reduction (Neumann)

The matrix equation 4.46 is modified by changing the first and last equations only, assuming (for zero gradient on the boundary) that the point just outside the boundary takes the same value as the point just inside the boundary:

$$\begin{bmatrix} -\alpha^{r=0} & 2 & 0 & 0 & \cdots & 0 \\ 1 & -\alpha^{r=0} & 1 & 0 & \cdots & 0 \\ 0 & 1 & -\alpha^{r=0} & 1 & \cdots & 0 \\ \vdots & \ddots & \ddots & \ddots & \ddots & \vdots \\ 0 & \cdots & 1 & -\alpha^{r=0} & 1 & 0 \\ 0 & \cdots & 0 & 1 & -\alpha^{r=0} & 1 \\ 0 & \cdots & 0 & 0 & 2 & -\alpha^{r=0} \end{bmatrix} \begin{bmatrix} \Omega_0 \\ \Omega_1 \\ \Omega_2 \\ \vdots \\ \Omega_{NZ-2} \\ \Omega_{NZ-1} \\ \Omega_{NZ} \end{bmatrix} = \begin{bmatrix} F_0^{r=0} \\ F^{r=0} \\ F^{r=0} \\ \vdots \\ F_{NZ-2}^{r=0} \\ F_{NZ-1}^{r=0} \\ F_{NZ}^{r=0} \end{bmatrix} \tag{4.53}$$

The algorithm is similar to that used for the Dirichlet condition, except that the reduction also involves the equations for $k$=0 and $NZ$.

The boundary equations are reduced using the adjacent equation as follows:

$$-\alpha\Omega_0+2\Omega_1=\Delta z^2 F_0 \tag{4.54a}$$

$$\Omega_0-\alpha\Omega_1+\Omega_2=\Delta z^2 F_1 \tag{4.54b}$$

Equation 4.54a is multiplied by α and 4.54b by 2 then adding together to produce the reduced form:

$$-(\alpha^2-2)\Omega_0+2\Omega_2=2\Delta z^2 F_1+\alpha\Delta z^2 F_0 \tag{4.55}$$

which can be refined into:

$$-\alpha^{r=1}\Omega_0+2\Omega_2=F_0^{r=1} \tag{4.56}$$

After $r_n$ reduction cycles equation 4.53 results in three equations analogous to equation 4.49:

$$\begin{bmatrix} -\alpha^{r=r_n} & 2 & 0 \\ 1 & -\alpha^{r=r_n} & 1 \\ 0 & 2 & -\alpha^{r=r_n} \end{bmatrix} \begin{bmatrix} \Omega_0 \\ \Omega_{NZ/2} \\ \Omega_{NZ} \end{bmatrix} = \begin{bmatrix} F_0^{r=r_n} \\ F_{NZ/2}^{r=r_n} \\ F_{NZ}^{r=r_n} \end{bmatrix} \tag{4.57}$$

If middle of equation (4.57) is multiplied by $\alpha^{r=r_n}$ and added to the other two equations, the central term is found:

$$\Omega_{NZ/2}=\frac{F_{NZ/2}^{r=r_n}+\left(F_{NZ}^{r=r_n}+F_0^{r=r_n}\right)/\alpha^{r=r_n}}{4/\alpha^{r=r_n}-\alpha^{r=r_n}} \tag{4.58}$$

and then by substituting (4.58) back into the boundary equations from (4.57) the values for boundaries are:

$$\Omega_0=\frac{2\Omega_{NZ/2}-F_0^{r=r_n}}{\alpha^{r=r_n}} \tag{4.59}$$

and:

$$\Omega_{NZ}=\frac{2\Omega_{NZ/2}-F_{NZ}^{r=r_n}}{\alpha^{r=r_n}} \tag{4.60}$$

The back-substitution required to recursively obtain the rest of the unknown values follows the same method as described in section 4.3.3.

If both boundary conditions are of Neumann type one integration constant remains undetermined. For wavenumber zero ($i$=$j$=0) equation 4.45 becomes:

$$\Omega_{k-1}-2\Omega_k+\Omega_{k+1}=-\Delta z^2 F_{k-1} \tag{4.61}$$

At each step in the cyclic reduction, the coefficient of every diagonal term is just:

$$\alpha^{r=n} = \alpha^{r=n-1}\,\alpha^{r=n-1} - 2 = 2 \tag{4.62}$$

For all *r*. The denominator of 4.58 is therefore zero and the value of $\Omega_{NZ}/2$ is undefined. To rectify this, the Dirichlet condition is used on $k=0$ and a Neumann condition on $k=NZ$ for this wavenumber only (equivalent to setting the average value of the function on the boundary to zero) so that equation 4.58 becomes:

$$\Omega_{NZ/2} = \frac{F_{NZ}^{r=r_n}/\alpha^{r=r_n} + F_{NZ/2}^{r=r_n}}{2/\alpha^{r=r_n} - \alpha^{r=r_n}} = -F_{NZ/2}^{r=r_n} - 0.5\,F_{NZ}^{r=r_n} \tag{4.63}$$

With the Neumann condition implemented in VCRED, further modifications to handle a combination of both Dirichlet and Neumann conditions over all wavenumbers is a trivial matter.

### 4.3.6 Non-zero boundary conditions

As previously discussed, the equation for *D* requires a non-zero boundary condition which depends on the solution and must be determined iteratively. For the Dirichlet condition with a non-zero boundary value, equation 4.46 is modified so that *f(x,y,z)* at $z=0$ or *NZ* contains the required boundary values in the first and last elements of the right hand side. This has to be done in such a manner as to provide the boundary values in the Fourier domain as *F(i,j,k)* at $k=0$ or *NZ*.

Equation 4.50 is then amended:

$$\begin{aligned} \Omega_0 &= F_0^{r=r_n} \\ \Omega_{NZ/2} &= \frac{F_0^{r=r_n} - F_{NZ/2}^{r=r_n} + F_{NZ}^{r=r_n}}{\alpha^{r=r_n}} \\ \Omega_{NZ} &= F_{NZ}^{r=r_n} \end{aligned} \tag{4.64}$$

Although the non-zero Dirichlet condition is not required in this formulation, the inclusion of this boundary condition is simple and may be useful for others at a later date.

For non-zero Neumann condition, the central difference form in the spatial domain is:

$$\frac{f_{x,y,1}-f_{x,y,-1}}{2\Delta z}=C_{0:x,y} \quad \text{for } z\text{=0 boundary} \tag{4.65a}$$

$$\frac{f_{x,y,NZ+1}-f_{x,y,NZ-1}}{2\Delta z}=C_{NZ:x,y} \quad \text{for } z\text{=1 boundary} \tag{4.65b}$$

Using equations (4.65a-b) to replace the references to external points in the first and last equations (*z=0,NZ*), which become in the centred difference form:

$$2f_{x,y,1}-2f_{x,y,0}=\Delta z^2\omega_{x,y,NZ}+2\Delta z C_{0:x,y} \quad \text{for } z\text{=0 boundary} \tag{4.66a}$$

$$2f_{x,y,NZ-1}-2f_{x,y,NZ}=\Delta z^2\omega_{x,y,NZ}-2\Delta z C_{NZ:x,y} \quad \text{for } z\text{=1 boundary} \tag{4.66b}$$

The boundary condition is simply implemented by addition of the terms containing *C(x,y,0)* or *C(x,y,NZ)* to the first or last entries in the *f(x,y,z)* vector before performing the Fourier transform. Because the right hand side of the input vector ***F*** is pre-multiplied by $\Delta z^2$ after the Fourier transform, the right hand side of equation 4.66 needs to be divided by $\Delta z^2$*:*

$$2\Delta z C_{0:x,y} \rightarrow \frac{2C_{0:x,y}}{\Delta z} \quad \text{for } z\text{=0 boundary} \tag{4.67a}$$

$$2\Delta z C_{NZ:x,y} \rightarrow \frac{2C_{NZ:x,y}}{\Delta z} \quad \text{for } z\text{=1 boundary} \tag{4.67b}$$

With this formulation for non-zero boundary conditions, the case of a Dirichlet boundary on one surface and a Neumann boundary on the opposite surface can equally be dealt with by appropriate combination of the numerical manipulations already described in the preceding sections. Thus, (4.46) can be expressed for the *z* boundary conditions on *D* in 4.80 as:

$$\begin{bmatrix} -\alpha & 2 & 0 & 0 & \cdots & 0 \\ 1 & -\alpha & 1 & 0 & \cdots & 0 \\ 0 & 1 & -\alpha & 1 & \cdots & 0 \\ \vdots & \ddots & \ddots & \ddots & \ddots & \vdots \\ 0 & \cdots & 1 & -\alpha & 1 & 0 \\ 0 & \cdots & 0 & 1 & -\alpha & 1 \\ 0 & \cdots & 0 & 0 & 0 & 1 \end{bmatrix} \begin{bmatrix} \Omega_0 \\ \Omega_1 \\ \Omega_2 \\ \vdots \\ \Omega_{NZ-2} \\ \Omega_{NZ-1} \\ \Omega_{NZ} \end{bmatrix} = \begin{bmatrix} F_0+2C_0\Delta z \\ F_1 \\ F_2 \\ \vdots \\ F_{NZ-2} \\ F_{NZ-1} \\ 0 \end{bmatrix} \tag{4.68}$$

With this new functionality, the modified VCRED and TDPOTS can be used to solve all combinations of the boundary conditions expressed in section 4.2.3.

### 4.3.7 Implementation of a tridiagonal algorithm in TDPOTS

I also introduced a new subroutine designated VCTRI to TDPOTS that applies the tridiagonal matrix solving algorithm (section 3.2.4) in such a way that the boundary conditions in section 4.2.3 can be handled. This provides an alternate algorithm that allows TDPOTS to solve equations of the form:

$$\nabla^2 \omega - q^2 \omega = -f \tag{4.69}$$

given that $q^2$ is a function of $z$ only.

Cyclic reduction can not solve (4.69) for ω so the tridiagonal matrix solver written by Press et al., (1986, p43) was included into TDPOTS to fill this role. The modifications required in TDPOTS for this additional subroutine and allowing it to handle non-zero boundary conditions were trivial.

### 4.3.8 Testing of TDPOTS (VCRED)

To test the validity of TDPOTS, I use a program called TESTDP that starts with an *ad hoc* harmonic function consistent with the boundary condition, applies the Poisson or biharmonic operators analytically, and uses the function thus obtained as input to TDPOTS. The original function then can be compared to the numerical solution obtained from TDPOTS in order to determine its accuracy. I modified TESTDP so as to allow testing of the new boundary conditions implemented in TDPOTS.

To test the inversion of the Poisson operator, TESTDP uses a function of the form:

$$\nabla^2 f(x, y, z) = \sum_{k=1}^{m} \sin(k\pi x + \psi_x \pi) \sin(k\pi y + \psi_y \pi) \sin(k\pi z + \psi_z \pi) \tag{4.70}$$

For $0 \le x \le 1$, $0 \le y \le 1$, $0 \le z \le 1$ and harmonics $k$ such that $0 \le k \le m$. For Dirichlet conditions $\psi_n = 0$ as to make $f = 0$ on the $n$ boundaries while for Neumann conditions the value $\psi_n = 0.5$ is used to set $\partial_n f = 0$ on the $n$ boundaries.

The analytical solution to equation 4.70 is:

$$f(x,y,z) = -\sum_{k=1}^{m} \frac{\sin(k\pi x + \psi_x \pi)\sin(k\pi y + \psi_y \pi)\sin(k\pi z + \psi_z \pi)}{3(k\pi)^2} \tag{4.71}$$

A simple zero boundary value is obtained if ψ=0 and a zero normal gradient is obtained if ψ=0.5, satisfying the boundary conditions required.

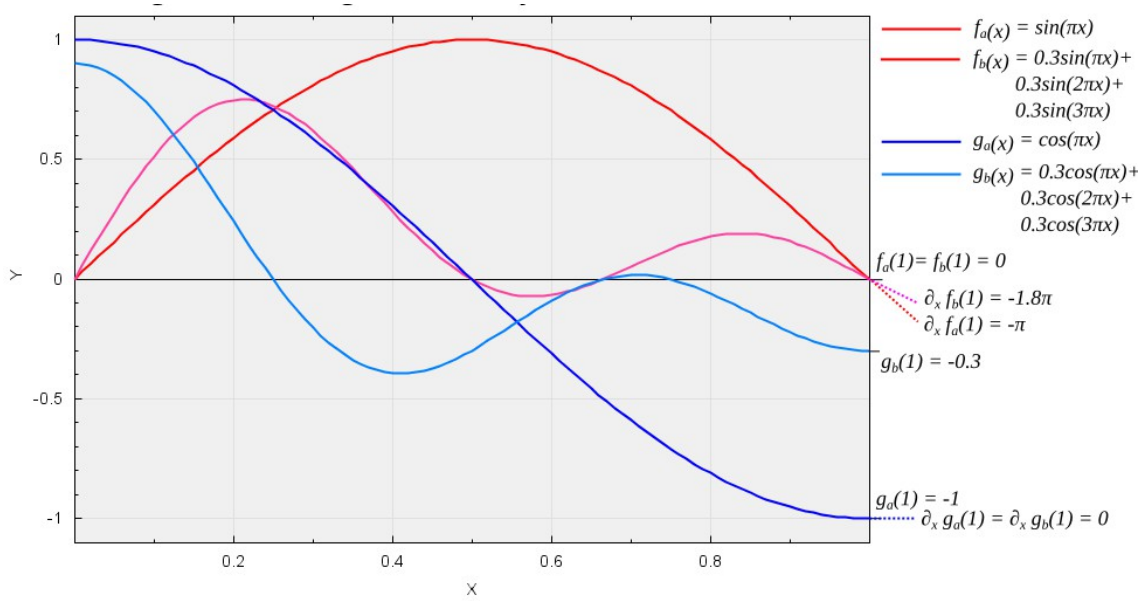


*Figure 36: Plot of four harmonics and their boundary conditions. The functions are a single harmonic sine (red) and cosine (blue) as well as a three harmonic sine (pink) and cosine (light blue). To the right the tangents at z=1 are projected from the graph and given analytically derived values, showing that a sum of sine waves has both zero Dirichlet and non-zero Neumann boundary conditions while a sum of cosine waves has both non-zero Dirichlet and zero Neumann boundary conditions.*

Swapping cosine for sine changes the boundary value from a non-zero value to a zero value (or *vice versa*). For example, the single harmonic sine wave in Figure 36 can be considered a zero Dirichlet condition as $f_a(x)=sin(\pi x)=0$ at $x=0,1$ or a non-zero Neumann condition as $\partial_x f_a(x)=\partial_x sin(\pi x)=\pi cos(\pi x)=\pi,-\pi$ at $x=0,1$. To test a non-zero boundary condition, values must be provided from the analytic solution (4.71).

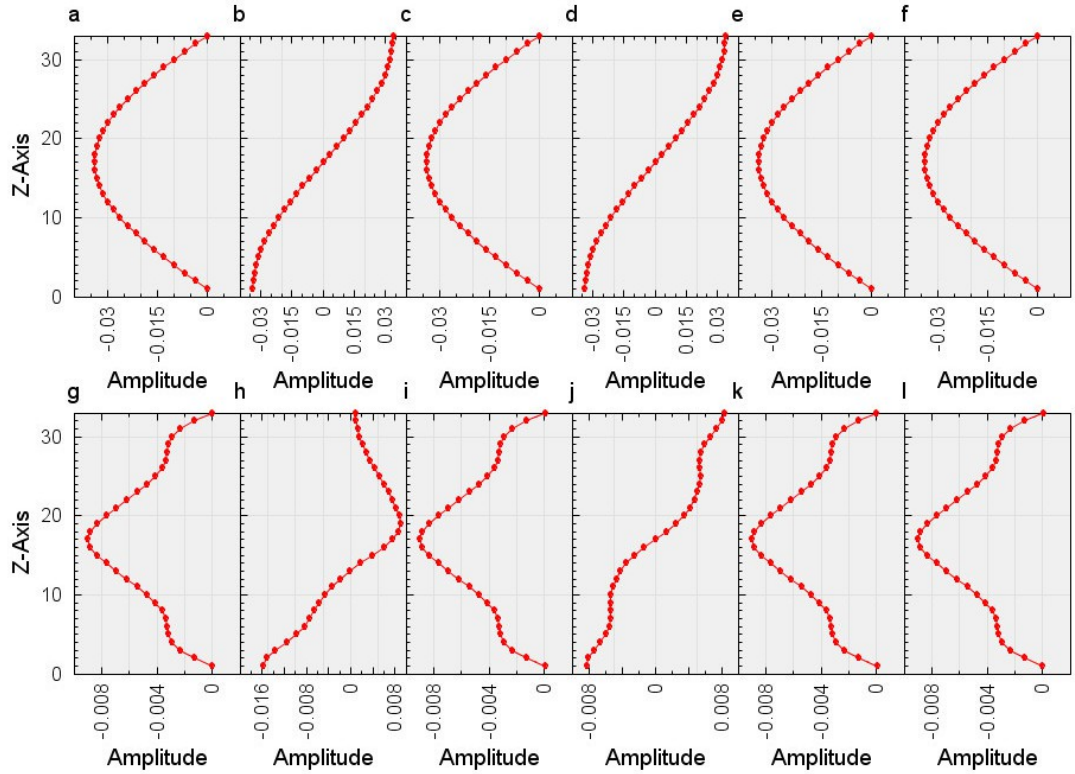


*Figure 37: One-dimensional sections of three-dimensional analytical and numerical tests of the cyclic reduction algorithm in TDPOTS. Numerical solutions to a defined problem, equation 4.70 (dots) and the corresponding analytical solutions (line, equation 4.71) are overlaid in 37a-l. 37a-f are single harmonic tests (m=1) and 37g-l use multiple harmonics (m=10). Boundary conditions for 37a and 37g are 0 Dirichlet; 37b and 37h are 0 Neumann; 37c and 37i are non-zero Neumann; 37d and 37j are non-zero Dirichlet; 37e and 37k are 0 Dirichlet at z=1 and non-zero Neumann at z=0 while 37f and 37l are non-zero Neumann at z=1 and 0 Dirichlet at z=0. For all tests* $\psi_x = \psi_y = 0$ *and the section is taken at* $x = y = 0.5$.

The following resulting tests of TDPOTS produce the data in Table 5:

| Boundary condition | $m_{diff}$ ($m$=1) | $m_{diff}$ ($m$=10) $IQ$=5 | $m_{diff}$ ($m$=10) $IQ$=6 | $\psi_z$ |
|---|---|---|---|---|
| $f(x,y,z)=0$, $z$=0,1 | 0.0267% | 0.2412% | 0.0605% | 0 |
| $f(x,y,z)=0$, $z$=0,1 | 0.0267% | 0.2183% | 0.0559% | 0.5 |
| $f(x,y,z)=C(x,y)$, $z$=0,1 | 0.0967% | 0.9477% | 0.2589% | 0.5 |
| $\partial_z f(x,y,z)=C(x,y)$, $z$=0,1 | 0.0250% | 0.1928% | 0.0514% | 0 |
| $\partial_z f(x,y,z)=C(x,y)$, $z$=0<br>$f(x,y,z)=0$, $z$=1 | 0.0944% | 0.9468% | 0.2587% | 0 |
| $f(x,y,z)=0$, $z$=0<br>$\partial_z f(x,y,z)=C(x,y)$, $z$=1 | 0.0190% | 0.2412% | 0.0605% | 0 |

*Table 5: Values of maximum absolute difference between analytical and numerical solution as a percentage of the largest absolute value of the analytical solution (Figure 37). The first column is for tests with a single harmonic (m=1) and a three-dimensional mesh of $(2^5+1)^3$ points (IQ=IQX=IQY=IQZ=5). In the second column the harmonic content is increased to (m=10). In the third column IQ is increased to 6 so that the numerical grid is spanned by 65 points in each direction. For all tests $\psi_x = \psi_y = 0$ and the section is taken at $x = y = 0.5$.*

For each test, I use the function described by equation 4.70 with the value of $\psi_z$ shown in Table 5 and $\psi_x = \psi_y = 0$ with the one-dimensional section taken at $x = y = 0.5$. For the first series of tests, Table 5, column 2 shows $m_{diff}$, the maximum absolute difference between analytical and numerical solution as a percentage of the maximum absolute value of the analytical solution. For a single harmonic (a single sine or cosine wave of wavelength 2), $m_{diff} < 0.1\%$ for all these tests.

In the second experiment, I increase the complexity of the problem by including more harmonics (specifically $m$=10, includes superposed sine or cosine waves of wavelength 2 to 0.2 in each direction). The shorter wavelength components contribute relatively larger error, so the accuracy of the solution is significantly reduced (column 3 of Table 5). In effect, the short wavelength components of the test function are represented using a coarser discretisation.

The solution to this resolution problem is to increase the number of mesh points used in numerical solution. When the numerical mesh is based on $65^3$ (274,625) points (column 4, Table 5) instead of $33^3$ (35,937) as used in the previous tests, there is an approximate 4-fold decrease in the value of $m_{diff}$ (compare columns 4 and 3 of Table 5). This decrease is fully consistent with the second-order accuracy of the discretisation used in the numerical solution, and confirms the relative accuracy of the method.

### 4.3.9 Testing of TDPOTS (VCTRI)

To check the validity and accuracy of the solutions produced by the VCTRI subroutine for equation (4.69), TESTDP is modified to include the $q^2\omega$ term:

$$q^2(z)=\frac{A_m}{m}\sum_{k=1}^{m}\left[\cos^2(k\pi z+\psi_z\pi)\right] \tag{4.72}$$

where $A_m$ is an arbitrary constant used to ensure $q^2\omega$ is comparable in magnitude to $\nabla^2\omega$. Using (4.72), equation (4.70) can be modified to define a test problem that is similar in form to equation (4.70):

$$\nabla^2 f(x,y,z)-q^2(z)f(x,y,z)=$$
$$\sum_{k=1}^{m}\left[\left(1-\frac{q^2(z)}{3(k\pi)^2}\right)\sin(k\pi x+\psi_x\pi)\sin(k\pi y+\psi_y\pi)\sin(k\pi z+\psi_z\pi)\right] \tag{4.73}$$

where *f(x,y,z)* is the same as that described by (4.71) as the equations describing the analytical solution and boundary conditions (4.72) do not need alteration.

The tridiagonal matrix solver algorithm was tested for several types of boundary condition: Dirichlet problem on $z$=0 and $z$=1, Dirichlet on $z$=0 and non-zero Neumann on $z$=1, and non-zero Neumann on $z$=0 and Dirichlet on $z$=1. In fact, only the latter conditions are needed in TD2PF, as stated in section 4.2.3.

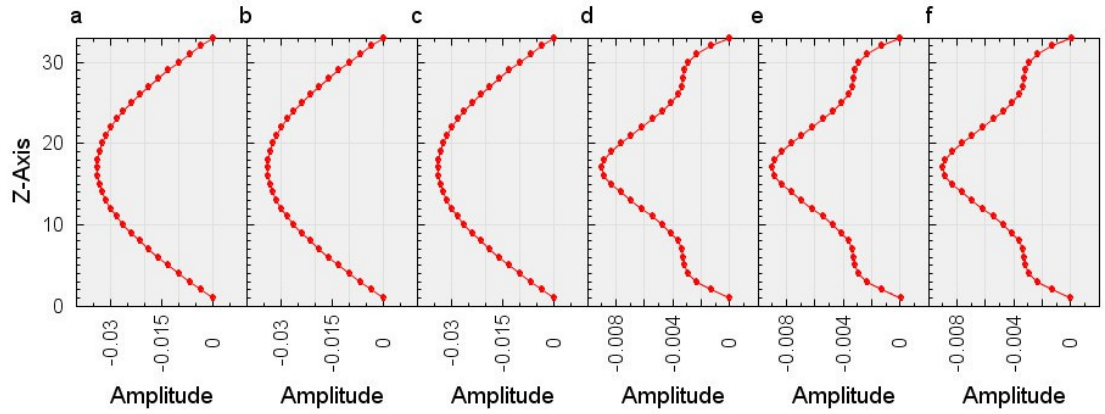


*Figure 38: One-dimensional sections of three-dimensional analytical and numerical tests of the tridiagonal algorithm in TDPOTS. 38a-f show overlain numerical solutions to a defined problem, equation 4.73 (dots) and the corresponding analytical solutions (line, equation 4.71). 38a-c are single harmonic tests (m=1), 38d-f multiple harmonics (m=10). Boundary conditions for 38a and 38d are 0 Dirichlet; 38b and 38e are 0 Dirichlet at z=1 and non-zero Neumann at z=0 while 38c and 38f are non-zero Neumann at z=1 and 0 Dirichlet at z=0.*

| Boundary condition | $m_{diff}$ ($m$=1) | $m_{diff}$ ($m$=10) | ψ |
|---|---|---|---|
| f(x,y,z)=0, z=0,1 | 0.0079% | 0.0551% | 0 |
| f'(x,y,z)=C(x,y), z=0<br>f(x,y,z)=0, z=1 | 0.0124% | 0.2143% | 0 |
| f(x,y,z)=0, z=0<br>f'(x,y,z)=C(x,y), z=1 | 0.0074% | 0.0551% | 0 |

*Table 6: The values of maximum absolute difference between analytical and numerical solution as a percentage of the largest absolute value of the analytical solution. For the first column of values in this test, a single harmonic (m=1) is used for a cube of $(2^6+1)^3$ data points, as IQ=IQX=IQY=IQZ=6 in these tests. In the second column, the harmonic count is increased to (m=10) to explore a more complex problem.*

The main test of note in Table 6 is the second one for Neumann at $z$=0 and Dirichlet at z=1. The value for the maximal error between numerical and analytical solution about four times greater than that of the other boundary condition solutions. However, this error is significantly affected by the number of points, decreasing to 0.005% for $m$=10 when $IQ$ is increased from $IQ$=6 to $IQ$=7. This decrease in accuracy is consistent with discretisation errors.

## *4.4 TD2PF*

### 4.4.1 Outline of modifications needed for TD2PF algorithm

I now summarise how the thermal convection program TDCON is adapted to become the melt migration program TD2PF.

Analogous to TDCON, the divergence-free part of the flow field is computed by solving the discretised form of equation (2.61):

$$\nabla^4 A_x = -\frac{\partial \varphi}{\partial y} \quad \text{and} \quad \nabla^4 A_y = \frac{\partial \varphi}{\partial x} \tag{4.74}$$

with the boundary conditions stated in section 4.2.3 which are identical to those used in TDCON and the non-dimensionalisation described in section 2.5.1. The buoyancy source terms for computation of the vector potential ***A*** in TD2PF require a simple change to 4.12 and 4.13:

$$\nabla^4 A_x = -\frac{\varphi_{i,\,j+1,\,k} - \varphi_{i,\,j-1,k}}{2\Delta y} \tag{4.75}$$

$$\nabla^4 A_y = \frac{\varphi_{i+1,\,j\,,k} - \varphi_{i-1,\,j\,,\,k}}{2\Delta x} \tag{4.76}$$

The boundary conditions on $A_x$ and $A_y$ are as stated in section 4.2.3. Compared to (4.12 and 4.13) does not appear in (4.75) and (4.76) because of the non-dimensionalisation described in section 2.5.1 and the temperature (*T)* has been replaced with melt fraction (φ).

The major new development in TD2PF is the addition of the solution procedure for the curl-free part of the flow field:

$$\nabla^2 D - q^2 D = p - \boldsymbol{r} \cdot \nabla D \tag{4.77}$$

where:

$$\nabla^2 B = D \tag{4.78}$$

and with the boundary conditions as discussed in section 4.2.3:

$$\frac{\partial D}{\partial x}=\frac{\partial B}{\partial x}=0 \quad \text{on} \quad x=0,h_x$$

$$\frac{\partial D}{\partial y}=\frac{\partial B}{\partial y}=0 \quad \text{on} \quad y=0,h_y$$

$$D=B=0 \quad \text{on} \quad z=1 \tag{4.79}$$

$$\partial_z D=\left(\frac{3\varphi}{3+\varphi}\right)\left(\frac{\partial}{\partial y}[\nabla^2 A_x]-\frac{\partial}{\partial x}[\nabla^2 A_y]-D\frac{\partial}{\partial z}[\varphi^{-1}]-(1-\varphi)\right) \; on \quad z=0$$

$$\frac{\partial B}{\partial z}=0 \quad \text{on} \quad z=0$$

The horizontal boundary conditions are readily implemented in TDPOIS by simply choosing cosine dependence in both the *x* and *y* directions for the Fourier expansion of 4.41 and 4.42. In the *z* direction, the upper boundary condition in TDPOIS is Dirichlet and readily implemented, while the non-zero Neumann condition on the lower ($z$=0) boundary requires amendment to the algorithm used in TDPOIS.

### 4.4.2 Initialisation of TD2PF

The time-stepping algorithms in TD2PF require an initial distribution of the melt fraction to be defined. Since I am studying the evolution of a spatially extensive melt distribution, the following three-dimensional Gaussian distribution superposed on a constant background melt fraction is used to create an initial condition with gradients in *x*, *y* and *z* directions:

$$\varphi(x,y,z)=\varphi_0+A\exp\left[-\frac{(x_0-x)^2}{2\sigma_x^2}-\frac{(y_0-y)^2}{2\sigma_y^2}-\frac{(z_0-z)^2}{2\sigma_z^2}\right] \tag{4.80}$$

with adjustable parameters $\varphi_0$, $A$, $x_0$, $y_0$, $z_0$, $\sigma_x$, $\sigma_y$ and $\sigma_z$, a broad class of initial conditions can be defined, including the one-dimensional model described in Chapter 3 if $\sigma_x$ and $\sigma_y$ are set to very large values. The option of adding a small amplitude perturbation function with fixed- or randomly-varying phase and amplitude is also retained from TDCON for the purpose of investigating unstable modes.

### 4.4.3 Solution algorithm for *D*

The first algorithm considered for the solution of the divergence equation was an iterative method which may be expressed as:

$$\nabla^2 D^{I+1} = p - \boldsymbol{r} \cdot \nabla D^I + q^2 D^I \tag{4.81}$$

where superscript *I* is an iteration count. In this form the Poisson solver TDPOTS can be used in principle to iteratively solve equation (4.81). On each iteration the right hand side is re-evaluated using the current estimate for *D*, then TDPOTS is applied again (using a modified version of the algorithm VCRED) to get the improved estimate for the next iteration. Iterations are repeated until the solution *D* converges as assessed by evaluating the difference in *D* between iterations:

$$\frac{max|D^{I+1} - D^I|}{max|D^I|} < 0.001 \tag{4.82}$$

This method, though simple in concept, was not successful as an algorithm for *D*, because this method is inherently unstable. Numerical tests of the algorithm for finding *D* confirm this instability, shown in Figure 39.

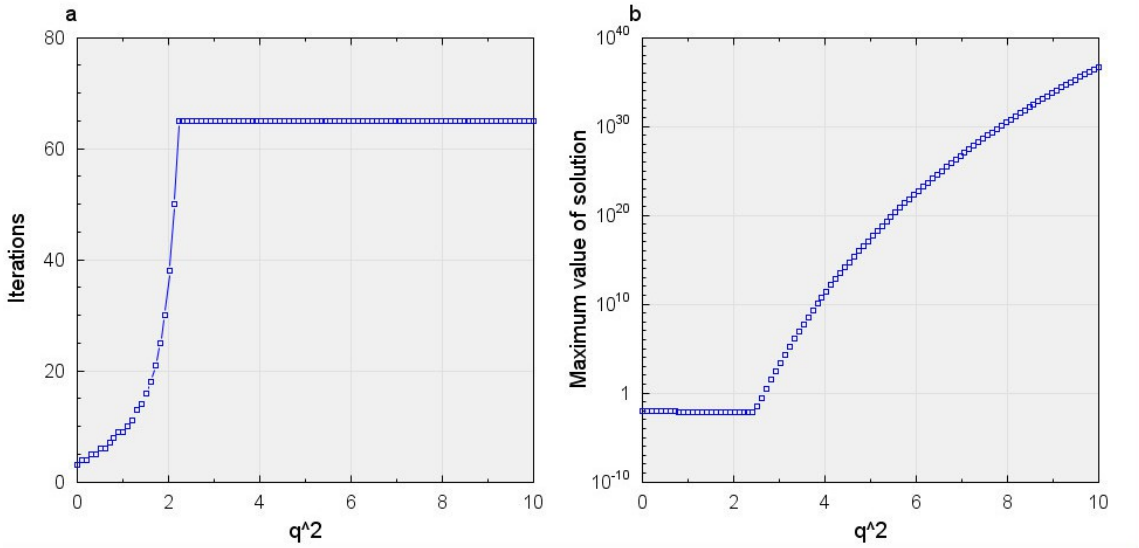


*Figure 39: Convergence of the iterative method of solving equation 4.81 for the constant melt fraction case with a variable $q^2$. 39a shows the number of iterations needed for the difference between solutions to satisfy equation 4.82 for different values of $q^2$. 39b shows the value of the iterative solution to D (equation 4.81) for each experiment. The method is only stable and convergent for $q^2 \leq 2.5$.*

Initial tests based on the compaction of a uniform layer ($\varphi(x,y,z)=\varphi_0$) were used to test the above method (the analytical solution for this problem was described in section

3.2.9). For $q^2 > 2.5$ (Figure 39) the solution for $D$ produced by the iterative algorithm oscillated from positive to negative and rapidly increased in magnitude with each iteration. This behaviour is indicative of an unstable numerical method, so the algorithm was refined to attempt to remove the problem, re-writing equation 4.81 in the form:

$$(\nabla^2 - q^2) D^{I+1} = p - \boldsymbol{r} \cdot \nabla D^I \tag{4.83}$$

By moving the $q^2D$ term from the right hand side to the left, a large part of the feedback loop that causes the numerical instability in the iterative method is stabilised.

Unfortunately, the revised equation 4.81 is incompatible with the $x$ and $y$ direction Fourier transform used in TDPOTS if $q^2$ has a functional dependence on $x$ and $y$, which it may if the melt fraction has gradients in those directions.

To resolve this problem, $q^2$ is separated into a $z$-dependent component, and an $x$- and $y$-dependent component:

$$q^2(x, y, z) = \bar{q}^2(z) + \hat{q}^2(x, y) \tag{4.84}$$

where:

$$\bar{q}^2_{(z)} = \frac{1}{ab} \iint [q^2_{(x,y,z)}] . dxdy \simeq \sum_{i=0}^{NX} \sum_{j=0}^{NY} [w_i w_j q^2_{(i,j,k)}] \tag{4.85}$$

Here, $w$ is the weight factor for boundary points needed to get an accurate estimate of the area integral defined on $0 \le x \le a$, $0 \le y \le b$:

$w_i$ = ½ when $i$=0 or $NX$

$w_j$ = ½ when $j$=0 or $NY$

Equation 4.81 can now be written:

$$(\nabla^2 - \bar{q}^2) D^{I+1} = p - \boldsymbol{r} \cdot \nabla D^I + \hat{q}^2 D^I \tag{4.86}$$

and a Fourier-based inversion can still be applied to the operator on the left hand side as $\bar{q}^2$ is independent of $x$ and $y$.

To facilitate comparison with the method described in section 4.3, consider the analogous problem:

$$(\nabla^2 - \bar{q}^2) \omega = -f \tag{4.87}$$

Applying the horizontal Fourier transform produces:

$$\left( \frac{\partial^2}{\partial z^2} - k^2 \right) \Omega - \bar{q}^2 \Omega = -F \tag{4.88}$$

and the discretised approximation is:

$$\Omega_{i,j,k-1}-\left(2+\left(k^2+\bar{q}^2\right)\Delta z^2\right)\Omega_{i,j,k}+\Omega_{i,j,k+1}=-F_{i,j,k}\Delta z^2 \tag{4.89}$$

The $z$-dependence of $\bar{q}^2$ prevents the straightforward use of a cyclic reduction algorithm to solve (4.89). Therefore a simple tridiagonal solver by Press et al., (1986, p43) is used to solve (4.89) before re-applying the horizontal Fourier transforms. As previously, inversion of the operator on the left hand side of (4.86) is repeated iteratively, with the right hand side updated at every iteration.

### 4.4.4 Validity tests of the iterative solution algorithm for *D*

I first retested the new algorithm implemented in VCTRI for solution of *D* with the constant melt fraction compaction problem in one dimension using the algorithm based on (4.86) to solve:

$$\left(\frac{\partial^2}{\partial z^2}-q^2\right)D^{I+1}=p-r\frac{\partial}{\partial z}D^I \tag{4.90}$$

To validate VCTRI, the one-dimensional compaction problem was used, the solution to which is defined by equation (3.42):

$$D=\frac{p}{q}\left[\frac{\sinh\left(q\left(h-z\right)\right)}{\cosh\left(qh\right)}\right] \tag{4.91}$$

where, from (3.32) non-dimensionalised:

$$\begin{aligned} q^2&=\left(\frac{3\varphi_0}{3+\varphi_0}\right)\frac{h_0^2}{\varphi_0^2}\\ p&=-\left(\frac{3\varphi_0}{3+\varphi_0}\right)\left(1-\varphi_0\right)\end{aligned} \tag{4.92}$$

This analytic solution applies only at time zero to the case of initially constant melt fraction ($\varphi=\varphi_0$).

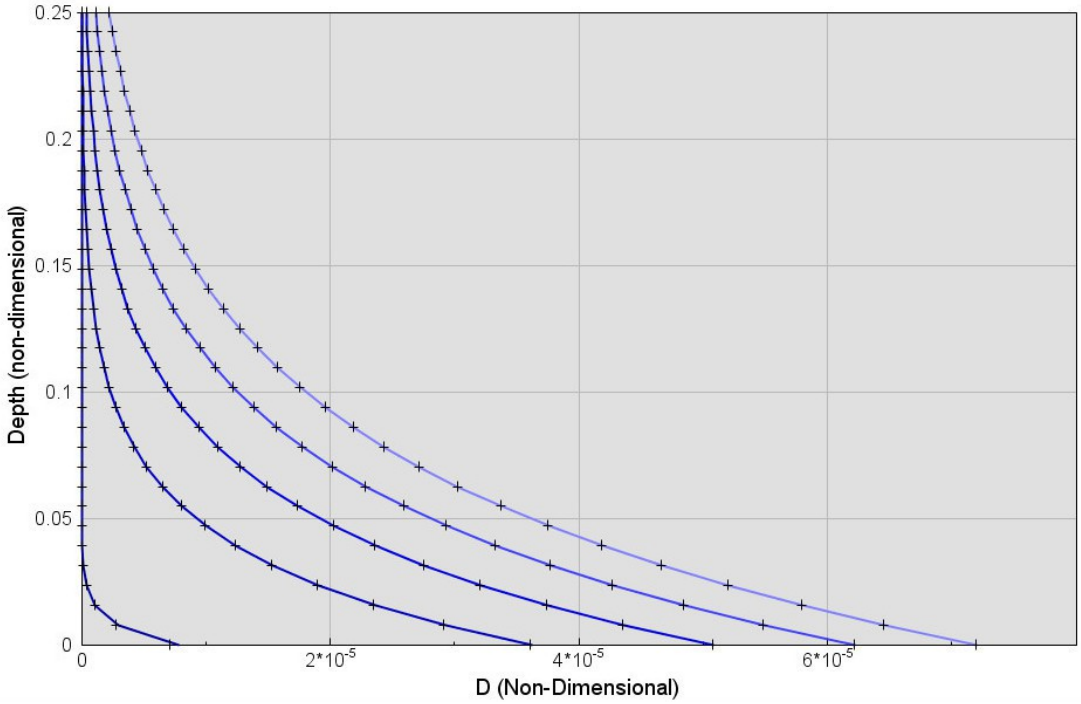


*Figure 40: Comparison of numerical solutions (crosses) using an algorithm based on equation (4.86), VCTRI, to analytical solutions defined by equation (4.91). The dark blue line is the solution for $\varphi_0$ =0.001, the light blue line $\varphi_0$ =0.101, with $\varphi_0$ =0.021, 0.041, 0.061 in progressively lighter shades of blue. All solutions use the length scale $\delta$ = h/4 as defined by (2.54).*

For these tests, the compaction length ($\delta = h/4$) was used with $\delta$ defined by (2.54) and the melt fraction was in the range of $\varphi_0$ =0.001 to $\varphi_0$ =0.101 (Figure 40). The maximum absolute difference ($m_{diff}$) between (4.91) and the numerical solution to (4.86) using VCTRI, expressed as a percentage of maximum value ($D_{max}$), is between 10% and 0.11% for $\varphi_0$=0.001 and 0.101 respectively using 129 points. The 10% error for $\varphi_0$=0.001 stems from the fact that the smaller melt fraction initial condition has a comparatively smaller compacting region and, as such, is more susceptible to discretisation errors. Increasing the discretisation to 257 points reduces $m_{diff}$ from 10% to 2.9% and 0.11% to 0.027% for $\varphi_0$=0.001 and $\varphi_0$=0.101 respectively.

I now describe tests which include a more complex *z*-dependence of melt fraction (still independent of *x* and *y)* which could be validated against an independent one-dimensional calculation using the one-dimensional program (1D2PF) discussed in chapter 3.

To do so the one-dimensional form of (4.80) for the initial melt fraction field was used in order to be consistent with initial condition in 1D2PF (3.10):

$$\varphi_{(x,y,z)}=\varphi_0+A\exp\left[-\frac{(z_0-z)^2}{2\sigma_z^2}\right] \tag{4.93}$$

Iterative solutions of (4.90) were completed when condition (4.82) was reached; typically 3 iterations were required for convergence of the examples shown in Figure 41.

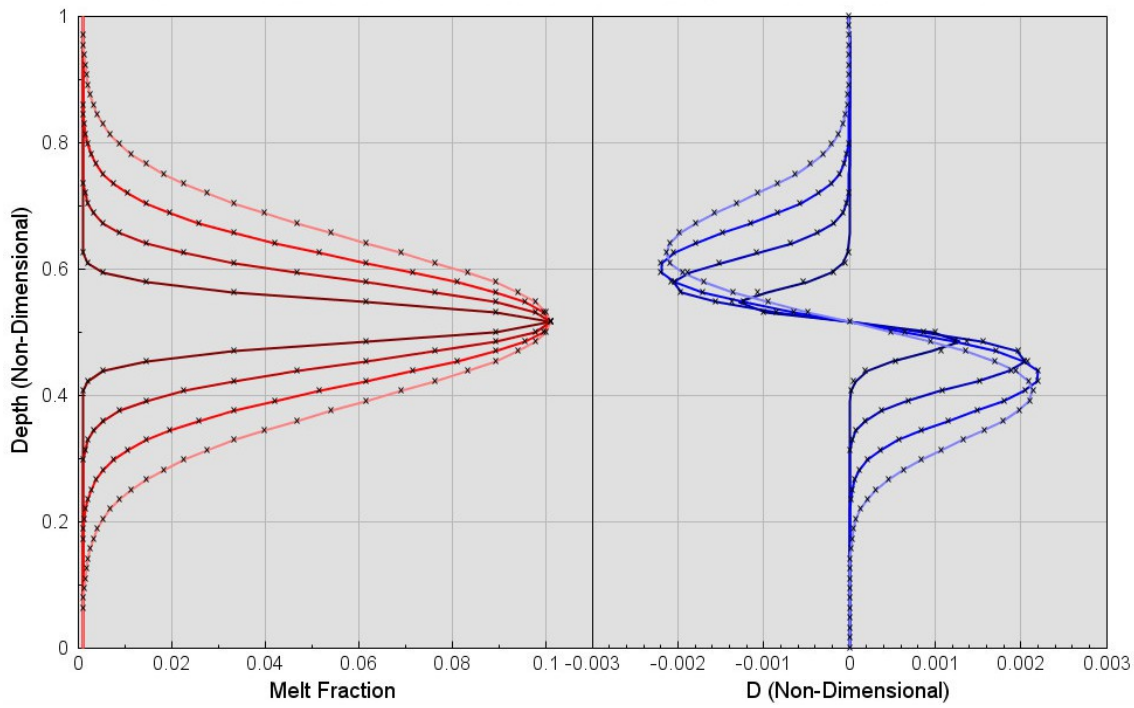


*Figure 41: Comparison of numerical solutions from VCTRI and 1D2PF (chapter 3). Left, melt fraction distributions (equation 4.80) used to calculate D for $\sigma_z=3.125\text{x}10^{-2}$ to $1.25\text{x}10^{-1}$ as listed in Table 7. Right, the corresponding D fields for t=0. The coloured lines are data from VCTRI while the black crosses are data from 1D2PF.*

For this test problem (4.93) the localised melt concentration introduces terms that depend on the gradient of the melt fraction. Figure 41 shows solutions obtained using 129 points, $\delta=h/4$, $A=0.1$, $\varphi_0=0.001$ with $\sigma_z$ values shown in Table 7 producing progressively wider Gaussian distributions of melt fraction for both VCTRI and 1D2PF.

| $\sigma_z$ (non-dimensional) | $m_{diff}$ for 64 points | $m_{diff}$ for 128 points |
|---|---|---|
| $3.125 \times 10^{-2}$ | 8.2% | 2.3% |
| $6.25 \times 10^{-2}$ | 1.5% | 0.39% |
| $9.375 \times 10^{-2}$ | 0.43% | 0.10% |
| $1.25 \times 10^{-1}$ | 0.15% | 0.043% |

*Table 7 Maximum absolute difference as a percentage of maximum value ($m_{diff}$) between VCRED algorithm and 1D2PF (chapter 3) solutions. Melt distributions were generated using the $\sigma_z$ values from the first column with equation (4.93).*

I also made a further series of tests to investigate the stability of the iterative method defined by equation (4.86) when the wavenumbers $k>0$. In these tests, $k$ follows the function:

$$k = N\,2\pi^2 \quad \text{for} \quad 0 \leqslant N \leqslant 150 \tag{4.94}$$

I solved (4.88) iteratively using the same $p$ and $r$ for all values of $k$ for each $\sigma_z$ in Table 7. There is no independent verification of the answer to this problem, but the object of the test was to find if the method would converge for all $k$ in a computation that is comparable to the full three-dimensional computation required to solve (4.77). To examine its effect on stability of the algorithm, $k$ is included in the numerical solution of (4.90) while the one-dimensional forms of the source term $p$ and feedback term $\boldsymbol{r}$ are retained:

$$\left(\frac{\partial^2}{\partial z^2} - \left(k^2 + q^2\right)\right) D^{I+1} = p - r\frac{\partial}{\partial z} D^I \tag{4.95}$$

The introduction of the wavenumber parameter $k$ increasingly weights the effect of the $D$ operator on the left hand side of equation 4.95 over the $\nabla^2 D$ with increasing $N$ and, as such, constitutes a possible source of instability.

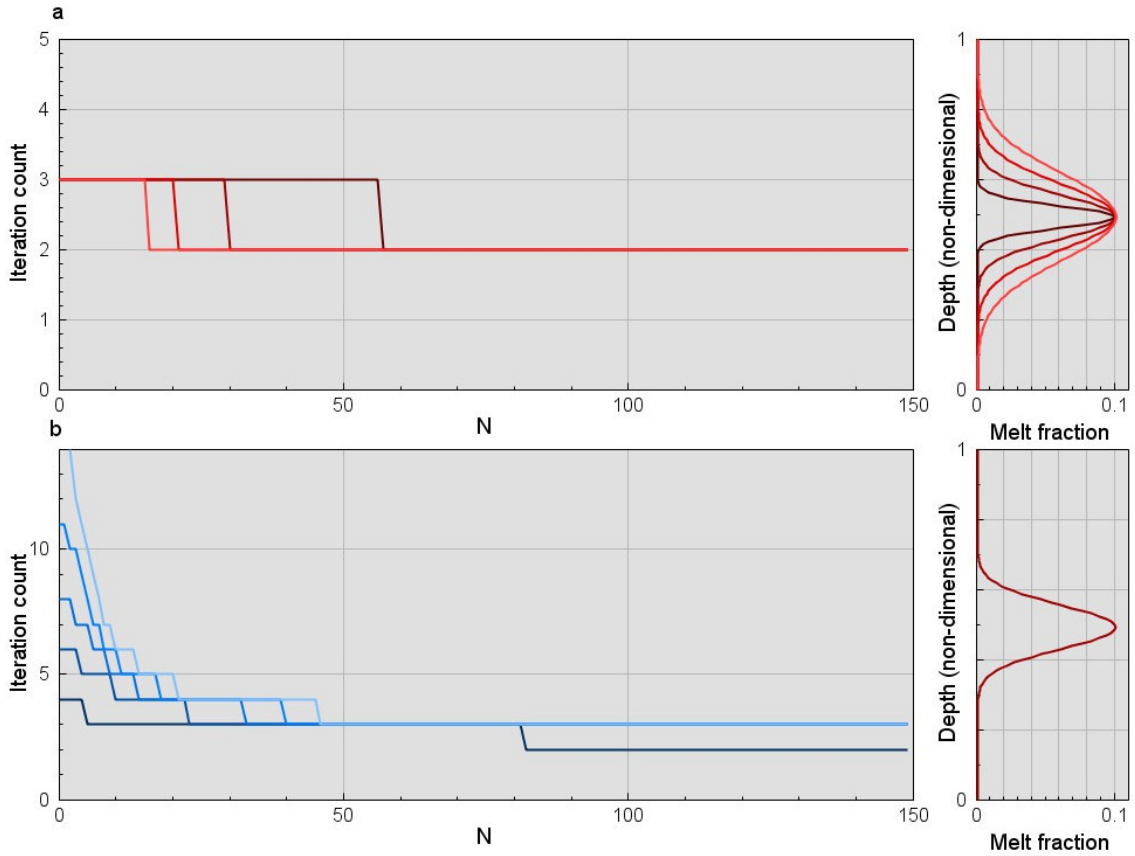


*Figure 42: Number of iterations needed to reach convergence for equation (4.95). a) Tests on increasing gradients of melt fraction (42a, right), using wavenumbers defined by N in equation (4.94) and melt-zone widths defined by $\sigma_z$ values listed in table Table 7 (column 1), from small $\sigma_z$ (dark red) to large $\sigma_z$ (light red). b) Numbers of iterations needed for convergence of equation (4.96) for $D_0$=10 (dark blue) to $D_0$=500 (light blue) and $\sigma_z$=6.25x10$^{-2}$. The convergence criteria used was (4.82).*

These tests of *k* showed that the solutions are typically solved in 4 to 3 iterations for low wavenumbers, but larger gradients of melt fraction may require extra iterations to converge as shown in Figure 42a.

One further test of algorithm stability was made by introducing a term representing an *x*- and *y*-dependant function comparable to the last term on the right hand side of equation (4.95):

$$\left(\frac{\partial^2}{\partial z^2}-\left(k^2+q^2\right)\right)D^{I+1}=p-r\frac{\partial}{\partial z}D^I+D_0 D^I \qquad (4.96)$$

As expected, the number of iterations needed to solve equation (4.96) rises with increasing amplitude of the constant factor $D_0$ (Figure 42b), but the compaction is stabilised by increasing wavenumber variable *N*. Figure 42b shows that the algorithm converges readily for larger wavenumbers, but failure of convergence can occur at the

longest wavelengths for large values of $D_0$. With this in mind, I proceeded to implement this algorithm in TDPOTS.

## *4.5 Other modifications required for TD2PF*

### 4.5.1 Algorithm for calculating *B*

The potential function *B* is obtained directly from *D* using TDPOTS to invert:

$$\nabla^2 B = D \tag{4.97}$$

The required boundary conditions are:

$$\frac{\partial B}{\partial z}\Big|_{z=0} = 0 \tag{4.98}$$

Based on zero flow across the base of the layer, while the upper boundary condition is:

$$B = 0 \quad on \quad z = h_z \tag{4.37}$$

This set of differing boundary conditions uses the modifications to VCRED mentioned earlier in section 4.3.5.

### 4.5.2 Modifications to time-step calculation

Although the advection equation (4.86) is similar to the thermal evolution equation (4.7), so that the general framework used in TDCON can be reapplied here, significant differences arise: Firstly, the terms representing diffusion are simply removed. Secondly, the advection terms now include spatial gradients of *B* in addition to those terms which include gradients of ***A*.**

The advection term may be written:

$$\boldsymbol{V}\cdot\nabla\varphi = \left(\frac{\partial B}{\partial x} - \frac{\partial A_y}{\partial z}\right)\frac{\partial \varphi}{\partial x} + \left(\frac{\partial B}{\partial y} + \frac{\partial A_x}{\partial z}\right)\frac{\partial \varphi}{\partial y} + \left(\frac{\partial B}{\partial z} + \frac{\partial A_y}{\partial x} - \frac{\partial A_x}{\partial y}\right)\frac{\partial \varphi}{\partial z} \tag{4.99}$$

which, when approximated using space-centred finite differences, yields the following discretised approximation to (4.86):

$$\begin{aligned}\frac{\partial \varphi}{\partial t} &= (1-\varphi) D_{i,j,k} \\ &+ \left(\frac{A_{y:i,j,k+1}-A_{y:i,j,k-1}}{2\Delta z} - \frac{B_{i+1,j,k}-B_{i-1,j,k}}{2\Delta x}\right)\left(\frac{\varphi_{i+1,j,k}-\varphi_{i-1,j,k}}{2\Delta x}\right) \\ &- \left(\frac{A_{x:i,j,k+1}-A_{x:i,j,k-1}}{2\Delta z} + \frac{B_{i,j+1,k}-B_{i,j-1,k}}{2\Delta y}\right)\left(\frac{\varphi_{i,j+1,k}-\varphi_{i,j-1,k}}{2\Delta y}\right) \\ &- \left(\frac{A_{y:i+1,j,k+1}-A_{y:i-1,j,k}}{2\Delta x} - \frac{A_{x:i,j+1,k}-A_{x:i,j-1,k}}{2\Delta y}\right)\left(\frac{\varphi_{i,j,k+1}-\varphi_{i,j,k-1}}{2\Delta z}\right) \\ &- \left(\frac{B_{i,j,k+1}-B_{i,j,k-1}}{2\Delta z}\right)\left(\frac{\varphi_{i,j,k+1}-\varphi_{i,j,k-1}}{2\Delta z}\right)\end{aligned} \tag{4.100}$$

In the absence of the diffusion term, the simple forward time-step representation of the time derivative can be used:

$$\varphi_{i,j,k}^{n+1} = \varphi_{i,j,k}^{n} + \left(\frac{\partial \varphi}{\partial t}\right)^{n} \Delta t^{n} \tag{4.101}$$

Where $\Delta t^n$ is a non-dimensional time-step calculated using the current condition as implemented in TDCON, basically ensuring a time-step that is small enough that no point in the solution domain can be advected further than one mesh interval during that time-step. Using equation 4.101 there is no need to store the *n*-1 melt fraction; the melt fraction array can be simply updated in place.

## *4.6 Time-stepping tests for TD2PF*

### 4.6.1 Solving the one-dimensional compaction problem

The first comprehensive test of the three-dimensional program TD2PF was to reproduce the solution of the one-dimensional compaction problem from an initially constant melt fraction. These solutions were validated by comparison with results from the one-dimensional program described in section 3.2.9. For my initial tests, I used a melt fraction of $\varphi(x,y,z)=\varphi_0=0.01$ and $\delta = h/2$ as defined by (2.54).

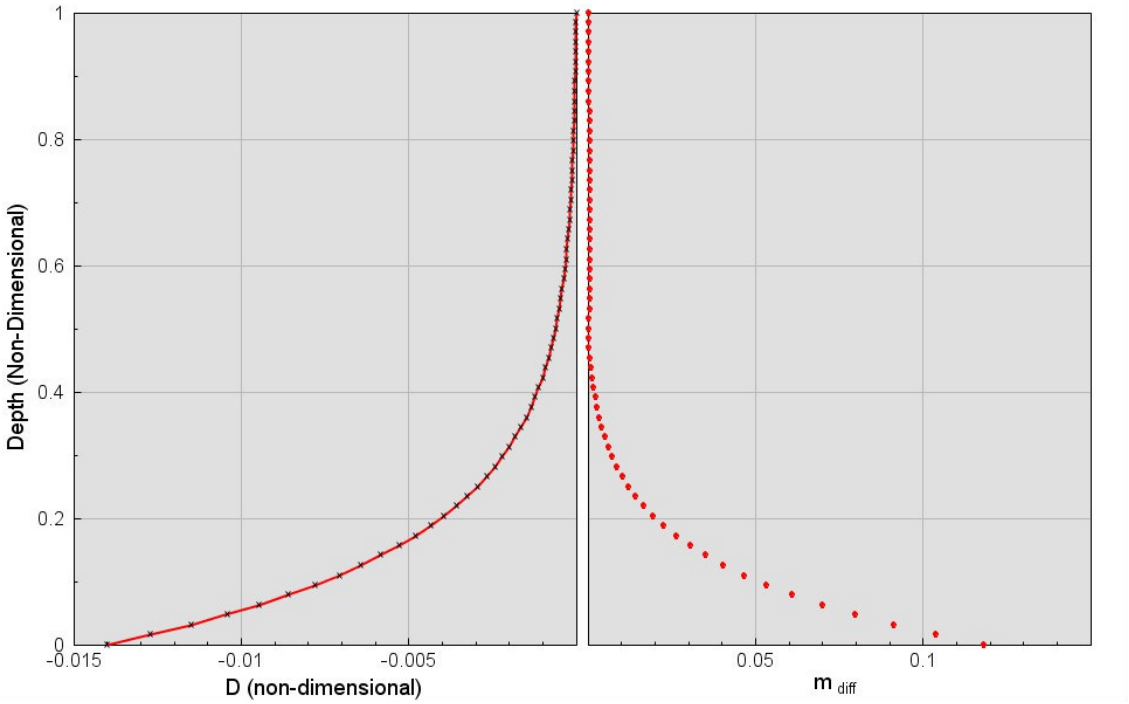


*Figure 43: Comparison of analytical solution to the numerical solution from TD2PF to a one-dimensional constant melt fraction problem. (a) Comparison at t=0 of the analytical solution to the one-dimensional compaction problem (red line) with the numerical solution from TD2PF (black crosses). (b) The difference between analytical and numerical solution as a percentage of the maximum value of the analytical ($m_{diff}$) of D. The initial melt fraction problem is $\varphi_0$=0.1, $\delta$ = h/2 as defined by (2.54) and NZ1=65 points.*

For *NZ1*=65 points, the maximum $m_{diff}$ is 0.12% which then decreases to $m_{diff}$=0.032% for *NZ1*=129. In this test case, the iterative procedure needed to calculate *D* only comes into effect as the melt fraction distribution evolves away from the initial homogeneous state for which $\boldsymbol{r}=\mathbf{0}$ and $q^2$=constant in (4.83).

The evolution of the melt fraction $\varphi_{(z)}$ and the divergence function $D_{(z)}$ for $t>0$ are shown in Figure 44. For this test, I used the same initial melt distribution ($\varphi_0$=0.01) length scale $\delta = h/2$ as defined by (2.54).

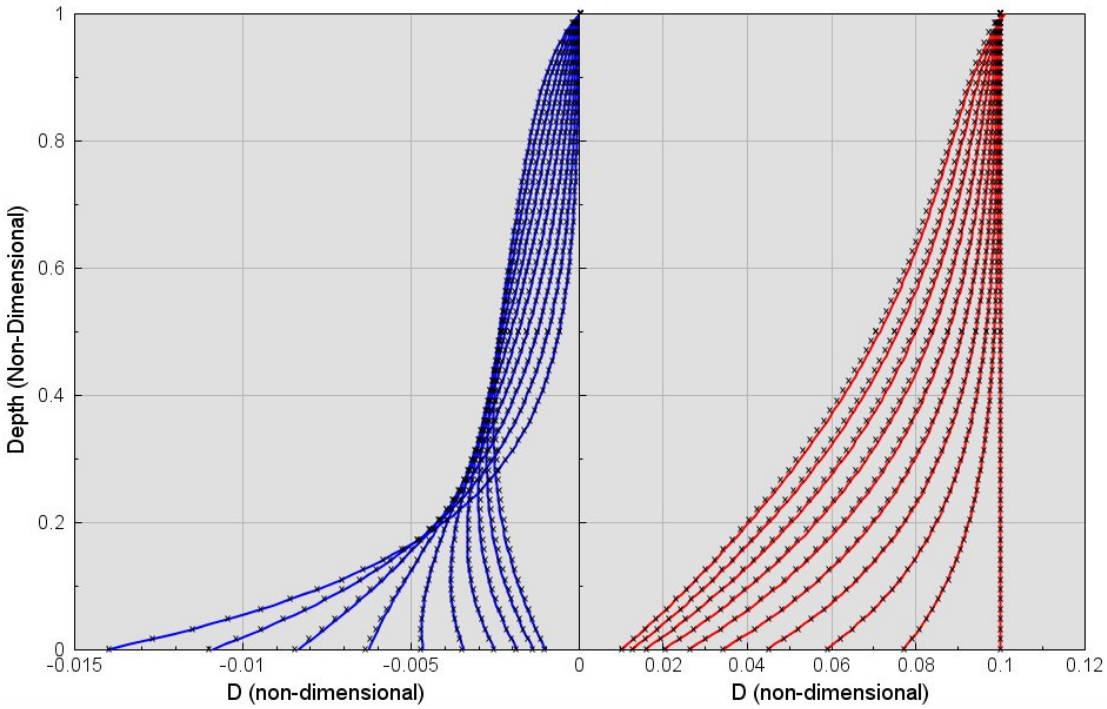


*Figure 44: Comparison of solutions for an initially constant melt fraction problem from TD2PF and 1D2PF. The lines are solutions obtained from 1D2PF, the crosses from TD2PF showing the melt fraction field $\varphi_{(z)}$ (left) and divergence field $D_{(z)}$ (right). Non-dimensional time-steps were $\Delta t=0.1$ up to a time $t=18$ and the mesh used NZ1=65 points.*

For $t$=18 (180 time-steps), an RMS error of 1.1% for the melt fraction and 2.0% for $D$ develops between the solutions obtained from the one-dimensional program (1D2PF) and that from the three-dimensional program (TD2PF).

### 4.6.2 Solving the one-dimensional Gaussian perturbation problem

The next stage of testing was to replicate a train of one-dimensional solitary waves in both 1D2PF and TD2PF. The initial condition used was a Gaussian perturbation upon a background constant melt fraction as defined by equation (4.80), using the parameters defined in Table 8.

| Parameter | $x_0$ | $y_0$ | $z_0$ | $\sigma_x$ | $\sigma_y$ | $\sigma_z$ | $A$ | $\varphi_0$ |
|---|---|---|---|---|---|---|---|---|
| Value | 0.5 | 0.5 | 0.1430 | 0.05058 | 1000 | 1000 | 0.1 | 0.001 |

*Table 8: Initial parameter values used in generating the solutions shown in Figure 45. These parameters relate to equation (4.80) which describes a three-dimensional Gaussian perturbation atop a background melt fraction. The values of $\sigma_y$ and $\sigma_x$ are large to render the distribution nearly one-dimensional in the z-direction.*

For this experiment, I used a mesh defined by *NX1*=*NY1*=129 and *NZ1*=257 to allow better vertical resolution of the solitary wave. The compaction length was again half of the non-dimensional layer thickness ($h_0$=2, Equation 2.55) and the time step size ($\Delta t$) was 0.1

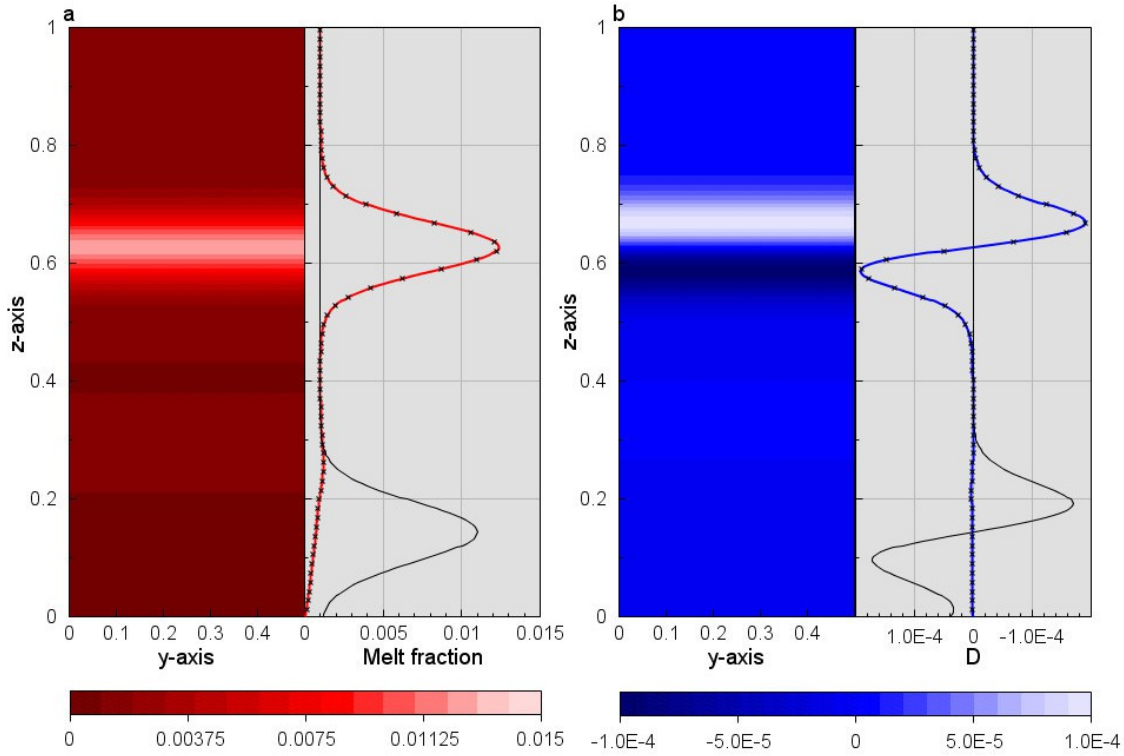


*Figure 45: Comparison of solutions from TD2PF and 1D2PF for an initial distribution of melt fraction that produces a solitary wave. The initial melt fraction (black line in 45a) is a function of z using equation 4.80 for the parameters in Table 8. The solution is at non-dimensional time t=200, depicting (a) melt fraction (φ) and (b) compaction rate (D). Contour plots are two-dimensional slices through the three-dimensional solution for melt fraction (red) and D (blue). Line plots show 1D sections for solutions generated by TD2PF (lines) and 1D2PF (crosses).*

Comparing solutions to the solitary wave propagation problem of Figure 45 obtained using TD2PF and 1D2PF (with *NZ1*=257), the maximum value of $m_{diff}$ at time $t$=200 (2000 time steps), are $m_{diff}$=0.84% for φ and $m_{diff}$=0.83% for $D$.

The comparison between these two independently-developed programs, 1D2PF based on the solution of the equation for $V$ (3.4), and TD2PF based on solution of the equations for $\boldsymbol{A}$ (4.75, 4.76) and $D$ (4.83), validates and provides confidence in the formulation and implementation of both methods.

### 4.6.3 Instability analysis

TD2PF in its current incarnation cannot solve *D* for a three-dimensional distribution of melt fraction using the iterative system described in section (4.4.3). The instability in the solution of *D* develops from gradients of melt fraction in the *x* and *y* direction which when multiplied by $\hat{q}^2$ in equation 4.86, promotes instability of the iterative algorithm.

In an email on 18 September 2012, G. Houseman set out the nature of this instability by first examining a simplified form of equation 4.81:

$$\nabla^2 D^{I+1} = p - \boldsymbol{r}\cdot\nabla D^I + q^2 D^I \tag{4.102}$$

which is repeated until:

$$max\left|D^{I+1} - D^I\right| \;\leq\; \varepsilon \tag{4.103}$$

Suppose the exact solution is $D_e$ and that after the *I*th iteration, $D^I$ differs from $D_e$ by:

$$D^I = D_e + \sum \varepsilon_{mn} \exp i\left(k_x x + k_y y + k_z z\right) \tag{4.104}$$

This expression is just the normal Fourier expansion of an arbitrary noise signal. The summation is over a complete set of the coefficients for which the wavenumbers are consistent with the boundary conditions. If equation (4.104) is substituted into (4.102):

$$\begin{aligned}\nabla^2 D^{I+1} &= p - \boldsymbol{r}\cdot\nabla D_e + q^2 D_e \\ -\sum i\left(\boldsymbol{r}\cdot\boldsymbol{k}\right)\varepsilon_{mn} \exp i\left(k_x x + k_y y + k_z z\right) &+ \sum q^2 \varepsilon_{mn} \exp i\left(k_x x + k_y y + k_z z\right)\end{aligned} \tag{4.105}$$

Then, because $D_e$ satisfies the governing equation exactly:

$$\nabla^2\left(D^{I+1} - D_e\right) = \sum \left(q^2 - i\,\boldsymbol{r}\cdot\boldsymbol{k}\right)\varepsilon_{mn} \exp i\left(k_x x + k_y y + k_z z\right) \tag{4.106}$$

Inverting the operator in (4.106) produces:

$$D^{I+1} - D_e = \sum \left(\frac{i\,\boldsymbol{r}\cdot\boldsymbol{k} - q^2}{\boldsymbol{k}\cdot\boldsymbol{k}}\right)\varepsilon_{mn} \exp i\left(k_x x + k_y y + k_z z\right) \tag{4.107}$$

where $k^2 = k_x^2 + k_y^2 + k_z^2$.

From (4.107) we see that the error signal is increased in amplitude by the factor $(i\boldsymbol{r}\cdot\boldsymbol{k} - q^2)/(\boldsymbol{k}\cdot\boldsymbol{k})$ at every iteration. The smallest, $k^2$ value sees the biggest increase in the error component at each iteration.

If the longest wavelength possible in a domain of width 1 is 2 (the zero horizontal wavenumber does not contribute because of the separation of components in equation 4.84), then the smallest horizontal wavenumber is:

$$k_{min}^2 = \pi^2 \tag{4.108}$$

And this longest wavenumber component has increased in amplitude after $N$ iterations by the factor:

$$f = \left( \frac{i\,\boldsymbol{r}\cdot\boldsymbol{k} - q^2}{\pi^2} \right)^N \tag{4.109}$$

The solution thus increases in amplitude without limit if the factor in parentheses has an absolute value greater than 1. The impact of this factor thus depends on the form of the vector function $\boldsymbol{r}$. In the simple case that $\boldsymbol{r} = \boldsymbol{0}$, the criterion for stability is that $-\pi < q < \pi$. For values of $q$ of greater magnitude, the analysis predicts systematic growth of a noise signal of the longest horizontal wavelength permitted by the boundary conditions.

## *4.7 Chapter Summary*

In this section, I provide a summary of chapter 4, discussing the construction and problems encountered while designing the three-dimensional numerical model. For efficiency, I chose to adapt a program written by Houseman (1987) named TDCON that utilises a Poisson solver named TDPOIS which was originally designed to produce solutions for a thermally convecting fluid. The mathematical model used by TDCON is similar in form to the two-phase fluid model (chapter 2), and as such conversion of TDCON to solve the two-phase problem was a more efficient solution than starting from scratch.

Another option would have been to implement the three-dimensional two-phase fluid model derived by Wiggins and Spiegelman (1995). Their method however uses significantly more simplifying assumptions than my formulation, ignoring matrix shear along with wider use of the small melt fraction approximation (Section 2.4.1). TDCON was converted to TD2PF by replacing the temperature field with melt fraction in the appropriate algorithms (section 4.4.1) and addition of a new algorithm to solve for divergence $D$ (section 4.4.3) using a heavily modified version of TDPOIS (renamed

TDPOTS, discussed section 4.3) along with a rewriting of the time step algorithm (section 4.5.2) for advection of melt fraction.

I thoroughly tested TD2PF and showed that it is second-order accurate in comparison to analytical solutions (section 4.6.1) and can produce accurate numerical solutions for one-dimensional problems that directly correspond to those produced by 1D2PF. Attempts to solve three-dimensional problems, where gradients of melt fraction exist in both *x* and *y* directions, produce a numerical instability in the iterative algorithm for solving *D*.

Two different approaches to solving for *D* have been discussed and analysed in this chapter. The first algorithm attempts to iteratively solve the equation:

$$\nabla^2 D^{I+1} = p - \boldsymbol{r} \cdot \nabla D^I + q^2 D^I \tag{4.110}$$

The algorithm worked by first producing an initial solution using $D^0 = 0$ for the right hand side which can then be solved by TDPOTS (modified version of TDPOIS) with defined boundary conditions to give $D^1$. Repeating this step with the new estimation of *D* until $\Delta D^I$ is below a threshold value (equation 4.82) a good approximation of *D* should be attained. However this approach proved to be unstable, with the solution inflating out of control with each iteration when *q* is sufficiently large, for all initial conditions tried.

I discovered that the $q^2$ term was the source of the instability (Figure 39) and to counter this TD2PF and TDPOTS were adapted again to handle a reformulation of equation 4.110:

$$(\nabla^2 - \bar{q}^2) D^{I+1} = p - \boldsymbol{r} \cdot \nabla D^I + \hat{q}^2 D^I \tag{4.111}$$

Equation 4.111 separated the $q^2$ term into two components, the *z*-dependent component, $\bar{q}^2$, and the *x*- and *y*-dependent components, $\hat{q}^2$ . This separation significantly reduced the potential for instability, as the driving force for the system is in the *z* direction. I investigated the potential for instability in the new formulation (Equation 4.111, section 4.4.4) and showed that the solution was stable in most circumstances, but would become unstable if the $\hat{q}^2$ became too large (Figure 42), with instability most likely at low horizontal wavenumbers.

I was able obtain one-dimensional solutions using the three-dimensional program

TD2PF which evolved correctly and without instability with second-order accuracy confirmed by the independently developed one-dimensional program 1D2PF predicted (Figure 44). However when relatively small *x* and *y* gradients of melt fraction emerged, *D* would again become unstable and explode in value.

In conclusion, I have outlined unsuccessful attempts in this search for a solution to the three-dimensional two-phase flow problem and have developed and detailed the source of the instability clearly. I have also significantly expanded TDPOIS in the form of TDPOTS, so that it can now handle a variety of mixed and non-zero boundary conditions and solve a new type of equation:

$$(\nabla^2 - q(z)^2) f(x, y, z) = g(x, y, z) \tag{4.112}$$

The instability of the particular algorithms for *D* explored here does not preclude the existence of another algorithm that is stable, or that further simplifying approximations may allow for a solvable system within the same broad framework that I have developed.

# 5 Discussion, conclusion and future work

During the course of this project, I have developed both one-dimensional and three-dimensional formulations of the two-phase flow problem in which magma moves through a deformable viscous matrix. Experiments with the one-dimensional compaction problem confirm that the base of the medium compacts via expulsion of the pore fluid, on a compaction length scale first identified by McKenzie (1984). Building on the results of Barcilon and Richter (1986), I confirmed with one-dimensional numerical solutions the stable propagation of the melt fraction pulses with a Gaussian depth profile. Initial perturbations evolve into either a single solitary wave (Figure 19) followed by a minor disturbance in the background melt fraction (Figure 20); or, above a critical perturbation width, a train of solitary waves, whose number increases with the initial perturbation width ($\lambda_I$), is formed. The secondary solitary waves have a systematically decreasing amplitude and width depending on certain parameters of the medium, which include permeability, matrix viscosity, and melt viscosity. The propagation velocity of the solitary waves depends primarily on the peak melt fraction amplitude (Figures 23 and 24), but also on the melt fraction independent compaction length scale $\delta$ (Equation 2.54) determined by matrix and fluid viscosity and permeability coefficient (Figure 29), confirming results by Barcilon and Richter (1986). A series of waves with varying amplitude is therefore naturally dispersed, resulting in melt concentration pulses arriving at the surface at intervals related to the difference in phase velocity between successive waves. The description of how these trains of solitary waves develop and propagate from the initial Gaussian melt fraction distribution has provided new insights into a potential mechanism for intermittent surface volcanism, first proposed by Scott and Stevenson (1984). I have also laid the groundwork for development of a parallelised computation algorithm for the three-dimensional two-phase flow problem, building on code previously developed for simulation of the three-dimensional thermal convection problem.

I have described some of the pitfalls and instabilities that arise with the potential function formulation, but successful completion of a working three-dimensional two-phase flow simulation was not possible in the time available.

### 5.1.1 One-dimensional solitary wave formation

Solitary waves in magmatic systems have previously been explored by numerous investigators using both numerical and analytical models as discussed in chapter 1. Their existence in the earth's mantle is still debatable as direct evidence of magmatic solitary waves is not yet accessible. However, the equations that govern the melt-rock system with low melt fraction show that solitary waves initiate from any spacial variability in the melt content. Spiegelman (1993a, 1993b, 1993c) has investigated this phenomenon in considerable detail in one and two dimensions.

Once initiated, solitary waves take relatively little time to stabilise into an approximately Gaussian shaped wave of stable form and velocity. Assuming the Gaussian form, I measured the width, amplitude and velocity of the solitary waves generated by numerical solution of the governing equations, so as to analyse their evolution. Greater amplitude causes an increased phase speed, as shown previously by Barcilon and Richter (1986). The width of the solitary waves follows the relationship:

$$\lambda_S \simeq 4.6\,\delta \tag{5.1}$$

and the amplitude varies approximately as:

$$A_S \simeq 89/\delta \tag{5.2}$$

where $\delta$ is the melt fraction independent compaction length, $\delta_c$ without $\varphi$ dependence (Equation 2.54) defined as:

$$\delta = \sqrt{\frac{k_0 \eta_m}{\eta_f}} \tag{5.3}$$

The phase velocity of the solitary wave is shown to be a more complicated function of the melt fraction independent compaction length and the matrix viscosity, obeying the equation:

$$\omega_s \approx C_2 (\delta)^{16/9} (\eta_m)^{-1} \tag{5.4}$$

Experiments with varying initial amplitudes and width revealed an intriguing relationship between the initial width of the perturbation and the volume of the stably propagating pulse (Figure 25). Below a critical value of the initial width, the input pulse propagates as a stable solitary wave, but above this threshold, fluid from the initial melt fraction that is not accommodated in the primary wave ends up in one or more secondary solitary waves. Partitioning of melt into secondary solitary waves only occurs for initial perturbation widths above this threshold (Figure 32).

In conclusion, my numerical solutions have provided further evidence of the permanence of form associated with solitary waves that have an approximately Gaussian profile in the distribution of melt fraction, and confirmed the dependence of phase velocity on amplitude demonstrated by Barcilon and Richter (1986). I showed also that there is a preferred solitary wave width that is directly proportional to the compaction length scale defined by McKenzie (1984) (basically the square root of the ratio of matrix viscosity to fluid viscosity, multiplied by the permeability coefficient).

### 5.1.2 One-dimensional solitary wave trains

For a sufficiently thick Gaussian melt fraction profile or small melt fraction independent compaction length, a series of size-ordered solitary waves will result, which disperse because the larger pulses have a greater phase velocity. A broad zone of diffuse partial melt is therefore likely to produce a sequence of magmatic pulses arriving at the surface at discrete times, each pulse smaller than the last. This however would require that melt built up in a small region before being expelled, which is contradicted by geochemical evidence from Kelemen et al. (1997) that the melt fraction builds up to ~7-13% at maximum before extraction. Furthermore, numerical solutions by Scott and Stevenson (1984) indicate that a band of melting produces a train of similarly spaced and shaped waves.

Where secondary waves were not produced, a small-amplitude disturbance (~0.3% of the amplitude of the primary wave, for the example of Figure 20) was observed in some calculations. This disturbance is found close to the site of initial perturbation of the melt fraction when there are no secondary solitary waves. As the solution becomes closer to one that developing a secondary solitary wave, the magnitude of the disturbance reduces

to nothing. I suggest that this disturbance is a result of the input perturbation not exactly matching the stable solitary wave in amplitude and width required for stable propagation in a medium with the defined physical properties.

The further investigation of solitary wave train formation from a lens-like structure, with horizontal offsets related to transform faults, may provide insights into the melt transport under a ridge system. Here I have only touched on the small-scale disturbance to the melt fraction that forms from incomparability between the initial condition and solitary wave that evolves from it. As such, one component of future studies would be to take a more in-depth look at the reasons for this incompatibility and examine the small-scale disruptions closer, examining the phenomena for different initial distributions of melt fraction and $\delta$.

### 5.1.3 Development of a three-dimensional two-phase flow algorithm

As part of this project, considerable effort was invested in development of a new non-dimensional algorithm for solution of the two-phase flow problem. This algorithm is based on a potential function representation of the matrix velocity field, which has the advantage of separating naturally those parts of the flow that describe compaction or expansion of the matrix (using a scalar function $B$) and those that describe advection without change of melt fraction (using a vector function $\boldsymbol{A}$). The scalar potential function $B$ was found to be simply related to the divergence of the flow field $D$ and a governing equation for $D$ was derived. Efforts to find an efficient algorithm for the solution of this equation have not yet been successful. A simple iterative approach to solution of the equation for $D$:

$$\nabla^2 D = \vec{\boldsymbol{r}} \cdot \nabla D + q^2 D + p \tag{5.5}$$

is found to be numerically unstable. A solution to this problem was not possible in the available time, however major progress was made in the development of the program TD2PF, which was proven to accurately solve the one-dimensional compaction test case. At this time the remaining major requirement for a working non-dimensional program is to design and implement an efficient and stable algorithm for the solution of the above equation.

The clearest avenue for future work on this topic revolves around continuing the

development of the three-dimensional two-phase flow simulation program TD2PF. Although various studies by other authors have investigated aspects of the one- and two-dimensional problems, little has been done using three-dimensional numerical solutions to this two-phase system representing partially molten mantle. Adaptation of the mathematical model by Wiggins and Spiegelman (1995) into TD2PF would be one such possible way of solving the instability in the *D* solving algorithm.

### 5.1.4 Application of model results to Earth processes and observations

The existence of solitary wave trains (Figure 22) would imply a possible deep control on the periodicity of surface volcanism. The trains of solitary waves I have studied consist of a series of waves at intervals governed by the relative phase velocity of each solitary wave, expressed as:

$$\Delta t = \frac{b}{\omega_{n+1}} - \frac{b}{\omega_n} \tag{3.50}$$

where $\Delta t$ is the time between arrivals of wave $n$ and $n$+1, $b$ is the depth of solitary wave formation and $\omega$ is the solitary wave phase velocity of pulse $n$ in the train.

This mechanism indicates that the majority of melt would arrive at the base of a volcanic system in pulses rather than by percolation of melt at a constant rate.

Based on my calculations of solitary wave velocities, amplitudes and widths (Figures 23 and 24) and equation 3.50, I calculate the time period between eruptions at 3160 years between the 1st and 2nd, and 3200 years between the 2nd and 3rd arrivals for an initial perturbation width of ~9km at a depth of ~80km with the parameters from Table 1. The difference between sequential arrivals remains small compared to the value of $\Delta t$ for both larger and smaller $\lambda_I$, as shown in Table 4. Solitary wave velocity however is sensitive to the parameters governing the region and for the ranges of matrix viscosity, fluid viscosity and permeability I have studied in section 3.3.2, $\Delta t$ is on the order $10^3$ to $10^5$ years.

Plots of volcanic eruptions going back ~10000 years for the more well-documented volcanoes in Iceland (Siebert and Simkin, 2002) showed no discernible increase in eruptivity on the time-scales in question (~$10^3$ years). The absence of a clear signal however may depend to some extent on the patchy nature of eruptive history data;

recorded history, is far too short to accurately document the relevant time scales of volcanic activity mediated by solitary wave arrivals.

Comparison of solitary wave melt volume to erupted volume shows that solitary waves can provide the volume of melt seen over multiple eruptions. Krafla in Iceland for example produced $4.9x10^8m^3$ of erupted material over historical records (Siebert and Simkin, 2002). Assuming that the one-dimensional volumes in Figure 3.45 are representative of a cross section through a spherical three-dimensional solitary wave, the largest solitary wave I have studied in Chapter 3 has a melt volume of $5.7x10^7m^3$ (Figure 23). Experiments with initial perturbation widths of 9km and peak melt fraction ($A_l$) of 7 to 11% produce primary solitary wave volumes between $3.8x10^8m^3$ and $2.1x10^9m^3$ respectively. These volumes fall within the bounds required to feed the recorded erupted volume of Krafla for the past ~1000 years, supporting the argument that the solitary waves do not correspond to individual eruptions, but to periodic increases in volcanic activity on the time scales of thousands of years.

In conclusion, I have demonstrated that the solitary wave trains forming in a region of Earth-like parameters produce successive arrivals every $\sim10^3$ years and would expect a periodical increase and decrease in volcanic activity to match these periodic increases in melt flux from the mantle. I have also demonstrated that these solitary waves can contain enough melt volume to supply multiple volcanic eruptions, comparing the volume to the eruptive history of Krafla compiled by Siebert and Simkin, (2002).

Future geochemical dating and measurement of past eruptions over the time scales in question may uncover the proposed periodicity in volcanic activity.

# 6 References

Anderson, O. L., The temperature profile of the upper mantle, *Journal of Geophysical Research*, 85(B12), 7003-7010, 1980

Barcilon, V. & Richter, M., Nonlinear waves in compacting media, *Journal of Fluid Mechanics*, (164), 429-448, 1986

Barcilon, V. & Lovera, O. M., Solitary Waves in Magma Dynamics, *Journal of Fluid Mechanics*, (204), 10.1017/S0022112089001680, 1989

Bercovici, D., Ricard, Y. & Schubert, G., A two-phase model for compaction and damage: 1. general theory, *Journal of Geophysical Research*, 106(B5), doi:10.1029/2000JB900430, 2001a

Bercovici, D., Ricard, Y. & Schubert, G., A two-phase model for compaction and damage: 3. Applications to shear localization and plate boundary formation, *Journal of Geophysical Research*, 106(B5), doi:10.1029/2000JB900432, 2001b

Beutel, E., Wijk, J. V., Ebinger, C., Keir, D. & Agostini, A., Formation and stability of magmatic segments in the main Ethiopian and Afar rifts, *Earth and Planetary Science Letters*, (293), 225-235, 2010

Christiansen, J. P. & Hockney, R. W., DELSQPHI, A two dimensional Poisson-solver program, *Computer Physics Communications*, 2(3), 10.1016/0010-4655(71)90046-4, 1971

Coltice, N. & Schmalzl, J., Mixing times in the mantle of the early Earth derived from 2-D and 3-D numerical simulations of convection, *Geophysical Research Letters*, (33), doi:10.1029/2006GL027707, 2006

Connolly, J. A. D. & Podladchikov, Y. Y., Decompaction weakening and channelling instability in ductile porous media: Implications for asthenospheric melt segregation, *Journal of Geophysical Research*, (112), doi:10.1029/2005JB004213, 2007

Dziewonski, A. M. & Anderson, D. L., Preliminary reference earth model, *Physics of the Earth and Planetary Interiors*, 25(4), 10.1016/0031-9201(81)90046-7, 1981

Ebinger, C. J., Tectonic development of the western branch of the east African rift system, *Geological Society of America Bulletin*, 101(7), doi:10.1130/0016-7606(1989)101<0885:TDOTWB>2.3.CO;2, 1989

Hamling, I. J., Atele, A., Bennari, L., Calais, E., Ebinger, C. J., Keir, D., Lewi, E., Wright, T. J. & Yirgu, G., Geodetic observations of the ongoing dabbahu rifting episode: New dyke intrusions in 2006 and 2007, *Geophysical Journal International*, 178(2), doi:10.1111/j.1365-246X.2009.04163.x, 2009

Hewitt, I. J. & Fowler, A. C., Partial melting in an upwelling mantle column, *Proceedings of the Royal Society*, 464(2097), doi:10.1098/rspa.2008.0045, 2008

Hayward, N. J. & Ebinger, C. J., Variations in the along-axis segmentation of the Afar rift system, *Tectonics*, 15(2), doi:10.1029/95TC02292, 1996

Holtzman, B. K., Groebner, N. J., Zimmerman, M. E., Ginsberg, S. B. & Kohlstedt, D. L., Stress-driven melt segregation in partially molten rocks, *Geochemistry Geophysics Geosystems*, 4(5), doi:10.1029/2001GC000258, 2003

Holtzman, B. K. & Kohlstedt, D. L., Stress-driven melt segregation and strain partitioning in partially molten rocks: effects of stress and strain, *Journal of Petrology*, 48(12), doi:10.1093/petrology/egm065, 2007

Houseman, G. A., TDPOIS, a vector-processor routine for the solution of the three-dimensional Poisson and biharmonic equations in a rectangular prism, *Computer Physics Communications*, (43), 257-267, 1987

Houseman, G. A., Boundary conditions and efficient solution algorithms for the potential function formulation of the 3-D viscous flow equations, *Geophysical Journal International*, 100(1), doi:10.1111/j.1365-246X.1990.tb04565.x, 1990

Katz, R. F., Spiegelman, M. & Holtzman, B., The dynamics of melt and shear localization in partially molten aggregates, *Nature*, (442), doi:10.1038/nature05039, 2006

Katz, R. F., Magma dynamics with the enthalpy method: Benchmark solutions and magmatic focusing at mid-ocean ridges, *Journal of Petrology*, 49(12), 2099-2121, doi: 10.1093/petrology/egn058, 2008

Katz, R. F., Porosity-driven convection and asymmetry beneath mid-ocean ridges, *Geochemistry Geophysics Geosystems*, 11, Q0AC07, doi:10.1029/2010GC003282, 2010

Kelemen, P.B., Shimizu, N. & Salters, V.M.J., Extraction of mid-ocean-ridge basalt from the upwelling mantle by focused flow of melt in dunite channels, *Nature*, (375), doi:10.1038/375747a0, 1995

Kelemen, P. B., Hirth, G., Shimizu, N., Spiegelman, M. & Dick, H. J., A review of melt migration processes in the adiabatically upwelling mantle beneath oceanic spreading ridges, *Philosophical Transactions of the Royal Society London A*, (355), 283-318, 1997

Kohlstedt, D. L. & Zimmerman, M. E., Rheology of partially molten mantle rocks, *Annual Review of Earth and Planetary Sciences*, (24), doi:10.1146/annurev.earth.24.1.41, 1996

Kohlstedt, D. L. & Holtzman, B.K., Shearing melt out of the earth: an experimentalist's perspective on the influence of deformation on melt extraction, *Annual Review of Earth and Planetary Sciences*, (37), doi:10.1146/annurev.earth.031208.100104, 2009

Marchant, T.R. & Smyth, N. F., Approximate solutions for magmon propagation from a reservoir, *IMA Journal of Applied Mathematics*, 70(6), doi:10.1093/imamat/hxh069, 2005

McConnell, R. B., Geological Development of the Rift System of Eastern Africa, *Geological Society of America Bulletin*, 83(9), doi:10.1130/0016-7606(1972)83[2549:GDOTRS]2.0.CO;2, 1972

Mckenzie, D and O'Nions, R. K., Partial Melt Distributions from Inversion of Rare Earth Element Concentrations, *Journal of Petrology*, 32(5), doi:10.1093/petrology/32.5.1021, 1991
McKenzie, D, The generation and compaction of partially molten rock, *Journal of Petrology*, 25(3), doi:10.1093/petrology/25.3.713, 1984

Mohr, P. A. & Wood, C. A., Volcano spacings and lithospheric attenuation in the eastern rift of Africa, *Earth and Planetary Science Letters*, 33(1), doi:10.1016/0012-821X(76)90166-7, 1976

Morgan, J. P. & Holtzman, B. K., Vug waves: A mechanism for coupled rock deformation and fluid migration, *Geochemistry Geophysics Geosystems*, 6(Q08002), doi:10.1029/2004GC000818, 2005

Nakayama, M. & Mason, D. P., Rarefactive solitary waves in two-phase fluid flow of compacting media, *Wave Motion*, 15(4), doi:10.1016/0165-2125(92)90054-6, 1992

Nakayama, M. & Mason, D. P., On the Effect of Background Voidage on Compressive Solitary Waves in Compacting Media, *Journal of Physics A: Mathematical and General*, 28(7243), doi:10.1088/0305-4470/28/24/021, 1995

Nakayama, M. & Mason, D. P., Perturbation Solution for Small Amplitude Solitary Waves in Two-Phase Fluid Flow of Compacting Media, *Journal of Physics A: Mathematical and General*, 32(6309), doi:10.1088/0305-4470/32/35/309, 1999

Nooner, S. L., Bennati, L., Calais, E., Buck, W. R., Hamling, I. J., Wright, T. J. & Leqi, E., Post-rifting relaxation in the Afar region, Ethiopia, *Geophysical Research Letters*, (36), doi:10.1029/2009GL040502, 2009

Ohtani, E. & Maeda, M., Density of basaltic melt at high pressure and stability of the melt at the base of the lower mantle, *Earth and Planetary Science Letters*, 193(1-2), 10.1016/S0012-821X(01)00505-2, 2001

Parsons, R. A., Nimmo, F., Hustoft, J. W., Holtzman, B. K. & Kohlstedt, D. L., An experimental and numerical study of surface tension-driven melt flow, *Earth and Planetary Science Letters*, 267, 548-557, 2008

Press, W. H., Teukolsky, S. A., Vetterling, W. T. & Flannery, B. P., Numerical Recipes in Fortran 77: The Art of Scientific Computing 2ed, *Cambridge University Press*, p43, 1986

Rabinowicz, M. & Toplis M. J., Melt segregation in the lower part of the partially molten mantle zone beneath an oceanic spreading centre: Numerical modelling of the combined effects of shear segregation and compaction, *Journal of Petrology*, 50(6), doi:10.1093/petrology/egp033, 2009

Ribe, N. M., The deformation and compaction of partial molten zones, *Geophysical Journal Royal Astronomical Society*, 83, 487-501, 1985

Ricard, Y., Bercovici, D. & Schubert, G., A two-phase model for compaction and damage: 2. Applications to compaction, deformation, and the role of interfacial surface tension, *Journal of Geophysical Research*, 106(B5), doi:10.1029/2000JB900431, 2001

Richter, F. M. and McKenzie, D., Dynamical models for melt segregation from a deformable matrix, *Journal of Geology*, 92, 729-740, 1984

Richardson, C. N., Melt flow in a variable viscosity matrix, *Geophysical Research Letters*, 25(7), doi:10.1029/98GL50565, 1998

Richardson, C. N., Lister J. R. & McKenzie, D., Melt conduits in a viscous porous matrix, *Journal of Geophysical Research*, 101(B9), 20423-23432, 1996.

Roache, P.J., Computational Fluid Dynamics, *Hermosa Publishers*, 1972

Roony, T. O., Furman, T., Yirgu, G. & Ayalew, D., Structure of the Ethiopian lithosphere: Xenolith evidence in the main Ethiopian rift, *Geochemica et Cosmochimica Acta*, 69(15), 10.1016/j.gca.2005.03.043, 2005

Schiemenz, A., Liang, Y. & Parmentier, E. M, A high-order numerical study of reactive dissolution in an upwelling heterogeneous mantle—I. Channelization, channel lithology and channel geometry, *Geophysics Journal International*, 186(2), 641-664, 2011

Schmalzl, J., Houseman, G. A. & Hansen, U., Mixing in vigorous, time-dependent three-dimensional convection and application to Earth's mantle, *Journal of Geophysical Research*, 101(B10), 21847-21858, 1996

Scott, D. R. & Stevenson, D. J., Magma solitons, *Geophysical Research Letters*, 11(11), doi:10.1029/GL011i011p01161, 1984

Scott, D.R., & Stevenson D.J., Magma ascent by porous flow, *Journal of Geophysical Research*, 91(B9), doi:10.1029/JB091iB09p09283, 1986

Sempéré, J. C., Lin, J., Brown, H. S., Schouten, H. & Purdy, G. M., Segmentation and morphotectonic variations along a slow-spreading centre: The Mid-Atlantic Ridge, *Marine Geophysical Researches*, 15(3), 153-200, 1993

Siebert L, Simkin T (2002-). Volcanoes of the World: an Illustrated Catalog of Holocene Volcanoes and their Eruptions. Smithsonian Institution, Global Volcanism Program Digital Information Series, GVP-3, (http://www.volcano.si.edu/world/).

Simpson, G., Spiegelman, M. & Weinstein, M. I., A multiscale model of partial melts: 1. Effective equations, *Journal of Geophysical Research*, 115(B04410), doi:10.1029/2009JB006375, 2010a

Simpson, G., Spiegelman, M. & Weinstein, M. I., A multiscale model of partial melts: 2. Numerical results, *Journal of Geophysical Research*, 115(B04411), doi:10.1029/2009JB006376 , 2010b

Shaw, H. R., Rheology of basalt in the melting range, *Journal of Petrology*, 10(3), doi:10.1093/petrology/10.3.510, 1969

Spiegelman, M., Flow in a deformable porous media. Part 1: Simple analysis, *Journal of Fluid Mechanics*, (247), doi:10.1017/S0022112093000369, 1993a

Spiegelman, M., Flow in a deformable porous media. Part 2: Numerical analysis - the relationship between shock waves and solitary waves, *Journal of Fluid Mechanics*, (247), doi:10.1017/S0022112093000370, 1993b

Spiegelman, M., Physics of Melt Extraction: Theory, Implications and Applications, *Philosophical Transactions of the Royal Society London A*, 342(1663), doi:10.1098/rsta.1993.0002, 1993c

Spiegelman, M., Kelemen, P. B., & Aharonov, E., Causes and consequences of flow organization during melt transport: The reaction infiltration instability in compatible media, *Journal of Geophysical Research*, 106(B2):2061 2077, 2001

Ŝrámek, O., Ricard, Y. & Bercovici, D., Simultaneous melting and compaction in deformable two-phase media, *Geophysical Journal International*, 168(3), doi:10.1111/j.1365-246X.2006.03269.x, 2007

Stevenson, D. J., Spontaneous small scale melt segregation in partial melts undergoing deformation, *Geophysical Research Letters*, 16, 1067–1070, 1989

Takashi, D. & Satsuma, J., Explicit solutions of magma equations, *Journal of the Physical Society of Japan*, 57, 417-421, 1988

Thordarson, T and Larsen, G, Volcanism in Iceland in historical time: Volcano types, eruption styles and eruptive history, Journal of Geodynamics, 43(1), 10.1016/j.bbr.2011.03.031, 2007

Toramaru, A. & Fujii, N., Connectivity of melt phase in a partially molten peridotite, *Journal of Geophysical Research*, 91(B9), doi: 10.1029/0JGREA0000910000B9009239000001, 1986
Vaughn, P. J. & Kohlstedt, D. L., Distribution of the glass phase in hot-pressed olivine-basalt aggregates: an electron microscopy study, *Contributions to Mineralogy and Petrology*, 81(4), doi:10.1007/BF00371679, 1982

Wark, D.A. & Watson, E.B., Grain-scale permeabilities of texturally equilibrated, monomineralic rocks, *Earth and Planetary Science Letters*, 164(3-4), doi:10.1016/S0012-821X(98)00252-0, 1998

Whitehead, J. A., Dick, J. B. & Schouten, H., A mechanism for magmatic accretion under spreading centres, *Nature*, (312), doi:10.1038/312146a0, 1984

Wiggins, C. & Spiegelman, M., Magma migration and magmatic solitary waves in 3-D, *Geophysical Research Letters*, 22(10), doi:10.1029/95GL00269, 1995

Wolfenden, E., Ebinger, C., Yirgu, G., Deubi, A. & Ayalew, D., Evolution of the northern main Ethiopian rift: Birth of a triple junction, *Earth and Planetary Science Letters*, 244, 213-228, 2004

Wright, T. J., Ebinger, C., Biggs, B., Ayele, A., Yirgu, G., Kir, D. & Stork, A., Magma-maintained rift segmentation at continental rupture in the 2005 Afar dyking episode, *Nature*, (442), doi:10.1038/nature04978, 2006

Youngs, B. A. R., Calculations on the dynamical state of the lowermost mantle, PhD Thesis, *The University of Leeds*, 2007

Youngs, B. A. R. & Houseman, G. A., Formation of steep-sided topography from compositionally distinct dense material at the base of the mantle, *Journal of Geophysical Research*, (114), doi:10.1029/2007JB005487, 2009

Zhu, W. & Hirth, G., A network model for permeability in partially molten rocks, *Earth and Planetary Science Letters*, 212(3-4), 407-416, 2003

Zhu, W., Gaetani, G. A., Fusseis, F., Montési, L. G. J. & De Carlo, F., Microtomography of partially molten rocks: three-dimensional melt distribution in mantle peridotite, *Science*, 332(6025), doi:10.1126/science.1202221, 2011

# 7 Appendices

## 7.1 Appendix A: Derivation of $O(\Delta z^3)$ difference equations.

In section 2.6 I discuss the discretisation of the mathematical system to allow for numerical solution of the equations that describe a two-phase medium. To convert the analytical system of equations into numerical algorithms tools are required such as the finite difference method for approximation of a differential equation. In general, finite difference approximations are based on space-centred approximations, (e.g. 2.67, 2.68). On boundaries, however, it is sometimes necessary to use a one-sided approximation. I describe here the derivation of a one-sided approximation to the first derivative that is 2nd order accurate.

The first stage is to generate a series of Taylor expansions of function *f* for *h* to 2*h*:

$$f_{(x+h)} = f_{(x)} + h f'(x) + h^2 \frac{f''(x)}{2!} + O(h^2) \tag{7.1}$$

$$f_{(x+2h)} = f_{(x)} + 2h f'(x) + 4h^2 \frac{f''(x)}{2!} + O(h^2) \tag{7.2}$$

Backward Taylor expansions for -*h* to -2*h*:

$$f_{(x-h)} = f_{(x)} - h f'(x) + h^2 \frac{f''(x)}{2!} + O(h^2) \tag{7.3}$$

$$f_{(x-2h)} = f_{(x)} - 2h f'(x) + 4h^2 \frac{f''(x)}{2!} + O(h^2) \tag{7.4}$$

To find the first order forward difference approximation, equation 7.1 is multiplied by 4 and subtracted by equation (7.2). This removes the second order term to produce:

$$-4 f_{(x+h)} + f_{(x+2h)} = -3 f_{(x)} - 2h f'(x) + O(h^2) \tag{7.5}$$

Which can be rearranged to leave the second order accurate approximation for the first order forward difference:

$$f'(x) = -\frac{(3 f_{(x)} - 4 f_{(x+h)} + f_{(x+2h)})}{2h} + O(h^2) \tag{7.6}$$

The backwards difference equivalent of (7.6) is:

$$f'(x) = \frac{(3 f_{(x)} - 4 f_{(x-h)} + f_{(x-2h)})}{2h} + O(h^2) \tag{7.7}$$

using the same method.

## 7.2 Appendix B: Derivation of vector calculus identities.

I use many vector calculus identities in the derivation of the system of equations in chapter 2. In this section I go through two of these identities and prove them to be valid. The first identity is equation 2.10, restated here:

$$\nabla\cdot[\nabla\cdot[\boldsymbol{a}]\mathbf{I}] = \nabla[\nabla\cdot[\boldsymbol{a}]] \tag{2.10}$$

The divergence of the vector $\boldsymbol{a}$ is:

$$\nabla\cdot[\boldsymbol{a}]=\partial_x a_x+\partial_y a_y+\partial_z a_z \tag{7.8}$$

Multiplying (7.8) by the identity matrix:

$$\nabla\cdot[\boldsymbol{a}]\boldsymbol{I}=\begin{bmatrix}\partial_x a_x+\partial_y a_y+\partial_z a_z & 0 & 0\\ 0 & \partial_x a_x+\partial_y a_y+\partial_z a_z & 0\\ 0 & 0 & \partial_x a_x+\partial_y a_y+\partial_z a_z\end{bmatrix} \tag{7.9}$$

And then taking the divergence:

$$\nabla\cdot[\nabla\cdot[\boldsymbol{a}]\boldsymbol{I}]= (\partial_{xx} a_x+\partial_{xy} a_y+\partial_{xz} a_z)\hat{\mathbf{x}}+(\partial_{xy} a_x+\partial_{yy} a_y+\partial_{yz} a_z)\hat{\boldsymbol{y}}+(\partial_{xz} a_x+\partial_{yz} a_y+\partial_{zz} a_z)\hat{\boldsymbol{z}} \tag{7.10}$$

Then taking the gradient of (7.8):

$$\nabla[\nabla\cdot[\boldsymbol{a}]]= (\partial_{xx} a_x+\partial_{xy} a_y+\partial_{xz} a_z)\hat{\mathbf{x}}+(\partial_{xy} a_x+\partial_{yy} a_y+\partial_{yz} a_z)\hat{\boldsymbol{y}}+(\partial_{xz} a_x+\partial_{yz} a_y+\partial_{zz} a_z)\hat{\boldsymbol{z}} \tag{7.11}$$

So identity 2.10 is valid.
The second identity in question is:

$$\nabla\cdot[\nabla[\boldsymbol{a}]+(\nabla[\boldsymbol{a}])^T] = \nabla^2[\boldsymbol{a}]+\nabla[\nabla\cdot[\boldsymbol{a}]] \tag{2.11}$$

The gradient of **a** is:

$$\nabla[\boldsymbol{a}]=\begin{bmatrix}\partial_x a_x & \partial_x a_y & \partial_x a_z\\ \partial_y a_x & \partial_y a_y & \partial_y a_z\\ \partial_z a_x & \partial_z a_y & \partial_z a_z\end{bmatrix} \tag{7.12}$$

And the Transpose of this is:

$$\nabla[\boldsymbol{a}]^T=\begin{bmatrix}\partial_x a_x & \partial_y a_x & \partial_z a_x\\ \partial_x a_y & \partial_y a_y & \partial_z a_y\\ \partial_x a_z & \partial_y a_z & \partial_z a_z\end{bmatrix} \tag{7.13}$$

So the left hand side of 2.11 is:

$$\nabla\cdot[\nabla[\boldsymbol{a}]+(\nabla[\boldsymbol{a}])^T]=(2\partial_{xx}a_x+\partial_{xx}a_y+\partial_{xy}a_x+\partial_{xx}a_z+\partial_{xz}a_x)\hat{\boldsymbol{x}}$$
$$+(\partial_{yy}a_x+\partial_{xy}a_y+2\partial_{yy}a_y+\partial_{yy}a_z+\partial_{zy}a_y)\hat{\boldsymbol{y}}+(\partial_{zz}a_x+\partial_{xz}a_z+\partial_{zz}a_y+\partial_{yz}a_z+2\partial_{zz}a_z)\hat{\boldsymbol{z}} \quad (7.14)$$

Turning attention to the right hand side buy first calculating the vector Laplacian:

$$\nabla^2[\boldsymbol{a}]=\partial_{xx}a_x\hat{\boldsymbol{x}}+\partial_{yy}a_y\hat{\boldsymbol{y}}+\partial_{zz}a_z\hat{\boldsymbol{z}} \quad (7.15)$$

And then the right hand side using equation 7.11:

$$\nabla^2[\boldsymbol{a}]+\nabla[\nabla\cdot[\boldsymbol{a}]]=(2\partial_{xx}a_x+\partial_{xy}a_y+\partial_{xz}a_z)\hat{\boldsymbol{x}}$$
$$+(\partial_{xy}a_x+2\partial_{yy}a_y+\partial_{yz}a_z)\hat{\boldsymbol{y}}+(\partial_{xz}a_x+\partial_{yz}a_y+2\partial_{zz}a_z)\hat{\boldsymbol{z}} \quad (7.16)$$

Thus the identity is correct as (7.14) equals (7.16).